

# **Multi-scale Dynamics of Organic Light-Emitting Devices**

A dissertation submitted to the faculty of the graduate school of the University of  
Minnesota

Kyle William Hershey

In partial fulfillment of the requirements for the degree of Doctor of Philosophy

Russell J. Holmes, Advisor

February 20, 2018

## **Acknowledgements**

I would like to thank my research advisor Russell J. Holmes for all of his guidance and advice.

Parents

Mary Beth

Dow Chemical for funding and collaboration. Dow scientists for research guidance, samples, etc.

## **Dedication**

To some people that I value

## Abstract

Over the last decade, organic light-emitting devices (OLEDs) have grown to receive tremendous attention for application in commercial displays and in lighting. While mostly successful for small format displays, challenges still exist that limit their performance for broader applications. Many of these limitations stem from a lack of understanding of charge and exciton dynamics and their impact on efficiency and stability. In this presentation, we describe novel device characterization and modelling efforts aimed at elucidating key dynamic processes in multiple regimes, including the microsecond transient behavior, steady-state, and long term degradation.

A model is presented which unifies both the transient and steady-state electroluminescence behavior of an OLED as a function of current density. The excellent agreement between the model and experiment enables a deeper understanding of efficiency reduction at high brightness. Additionally, the relatively ambiguous device efficiency parameter of charge balance is recast as an exciton formation efficiency. This framework permits a novel characterization paradigm for decoupling degradation pathways during OLED life-testing. In addition to the luminance loss, the degradation in emitter photoluminescence and exciton formation efficiency are also extracted. This technique is applied to an archetypical phosphorescent OLEDs, enabling more comprehensive design rules for device engineering to realize enhanced lifetime. Data science is a rising topic in industrial research. A system for enabling data science techniques within laboratory research is presented. Select useful applications are demonstrated.

# Contents

<b>1 Overview of Organic Semiconductors</b>	<b>7</b>
1.1 Organic Semiconductors . . . . .	7
1.2 Excitons . . . . .	7
1.2.1 Singlets and Triplets . . . . .	7
1.2.2 Electronic Transitions . . . . .	7
1.2.3 Quenching Processes . . . . .	7
1.2.4 PL efficiency . . . . .	7
1.3 Charge Transport . . . . .	7
<b>2 Organic Light-Emitting Devices</b>	<b>8</b>
2.1 Architecture and Basic Operation . . . . .	8
2.1.1 Efficiency . . . . .	9
2.2 Fabrication Processes . . . . .	10
2.3 Characterization . . . . .	13
2.3.1 Current Voltage and Luminance . . . . .	13
2.3.2 Efficiency . . . . .	14
2.3.3 Chromaticity . . . . .	15
2.3.3.1 RGB . . . . .	16
2.4 Historical Development . . . . .	17
2.4.1 The First OLEDs . . . . .	17
2.4.2 Phosphorescence . . . . .	17
2.4.3 Thermally Activated Delayed Fluorescence . . . . .	18
2.5 Efficiency Roll-Off . . . . .	18
2.6 Recombination Zone Characterization . . . . .	19
2.7 Single Carrier Devices . . . . .	21
2.8 Operational Lifetime . . . . .	22
2.8.1 Degradation Mechanisms . . . . .	22
2.8.1.1 External: Dark Spots and Delamination . . . . .	23
2.8.1.2 Exciton and Polaron . . . . .	24
2.8.1.3 Interfaces . . . . .	24
2.8.2 Luminance Scaling . . . . .	25
2.8.3 Analysis Techniques . . . . .	26
2.8.3.1 Chemical Analysis . . . . .	26
2.8.3.2 Modeling . . . . .	27
2.8.3.3 Spectral Characterization . . . . .	28
<b>3 Transient and Steady-State Dynamics</b>	<b>30</b>
3.1 Motivation . . . . .	30
3.2 Theory . . . . .	32
3.2.1 Exciton Dynamics . . . . .	32
3.3 Polaron Dynamics . . . . .	33
3.3.1 Transient Electroluminescence . . . . .	34

3.3.2	Efficiency Analysis . . . . .	35
3.4	Experimental Details . . . . .	36
3.5	Exciton Quenching in Photoluminescence . . . . .	37
3.6	Application to Devices . . . . .	39
3.6.1	Quenching Only Steady-State Fit . . . . .	40
3.6.2	Transient Modeling . . . . .	40
3.6.3	Transient Term Efficiency . . . . .	41
3.6.4	Extracting Exciton Formation Efficiency . . . . .	42
3.6.5	Drift Model . . . . .	43
3.7	Understanding Assumptions of Polaron Model . . . . .	44
3.7.1	Carrier Injection . . . . .	44
3.7.2	Charge Imbalance . . . . .	46
3.8	Conclusion . . . . .	46
<b>4</b>	<b>Integrated Photoluminescence Lifetimes</b>	<b>48</b>
4.1	Luminance as Efficiency Loss . . . . .	49
4.2	Photoluminescence Characterization . . . . .	50
4.2.1	Light Selection . . . . .	52
4.2.2	Absorption - Recombination Overlap . . . . .	53
4.2.3	Contact Degradation . . . . .	53
4.2.4	Quenching Changes During Degradation . . . . .	54
4.2.5	Verification with Exciton Lifetime . . . . .	55
4.3	Experimental Implementation . . . . .	56
4.3.1	Motivation . . . . .	56
4.3.2	Development . . . . .	57
4.3.3	Hardware Setup . . . . .	59
4.3.4	Software Development . . . . .	60
4.4	Conclusion . . . . .	61
<b>5</b>	<b>Applied Integrated Lifetimes</b>	<b>62</b>
5.1	CBP Host Thickness . . . . .	62
5.1.1	Motivation and Experimental . . . . .	62
5.1.2	Results . . . . .	63
5.1.3	Conclusion . . . . .	65
5.2	MEML Luminance Scaling . . . . .	66
5.2.1	Motivation . . . . .	66
5.2.2	Experimental . . . . .	67
5.2.3	Results . . . . .	68
5.2.4	Conclusion . . . . .	71
5.3	Dow Cohost . . . . .	72
5.4	NPD Study . . . . .	72
<b>6</b>	<b>Novel Blue Emitter Development</b>	<b>74</b>
6.1	Molecular Systems . . . . .	74
6.2	Performance Optimization . . . . .	74
6.3	Solution Molecular Aggregation . . . . .	74
<b>7</b>	<b>Data Management for Devices</b>	<b>75</b>
<b>8</b>	<b>Modeling Out-Coupling</b>	<b>76</b>
8.1	Theory . . . . .	76
8.2	Recombination Zone Overlap During Lifetime . . . . .	76
<b>9</b>	<b>Future Research</b>	<b>77</b>

<b>Bibliography</b>	<b>77</b>
<b>Appendices</b>	<b>89</b>
<b>A List of Publications</b>	<b>89</b>
<b>B Measuring Triplet Energies</b>	<b>90</b>
<b>C Single Carrier Device Modeling</b>	<b>92</b>
C.1 Future Work . . . . .	94
<b>D Out-Coupling Code</b>	<b>95</b>
D.1 Transfer Matrix Model . . . . .	95
D.2 Out-Coupling (Power Dissipation) . . . . .	100
<b>E Lifetime Box Code</b>	<b>109</b>
<b>F Chemical Structures</b>	<b>110</b>
<b>G Material Properties</b>	<b>112</b>
<b>List of Figures</b>	<b>124</b>
<b>List of Tables</b>	<b>128</b>

# Chapter 1

## Overview of Organic Semiconductors

### 1.1 Organic Semiconductors

### 1.2 Excitons

#### 1.2.1 Singlets and Triplets

#### 1.2.2 Electronic Transitions

#### 1.2.3 Quenching Processes

#### 1.2.4 PL efficiency

### 1.3 Charge Transport

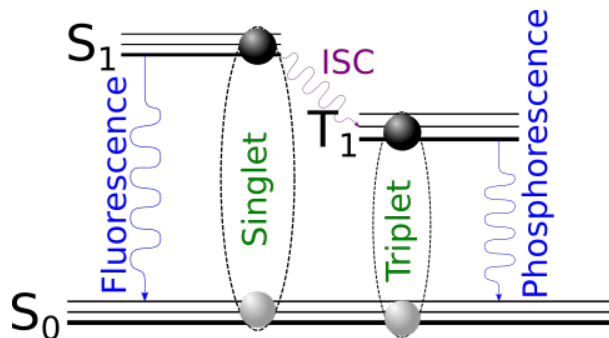


Figure 1.1: Simplified Jablonski diagram.

# Chapter 2

# Organic Light-Emitting Devices

## 2.1 Architecture and Basic Operation

Organic Light Emitting Devices (OLEDs) consist of an organic layer stack sandwiched between two electrodes. For light to escape, one of the electrodes is transparent, and in most lab scale devices, this is the bottom contact. This is often accomplished by using glass coated with Indium Tin Oxide (ITO) as a transparent conducting material. The opposing contact is typically a metal, and in most cases Aluminum. An example of this type of structure is shown in Figure 2.1.

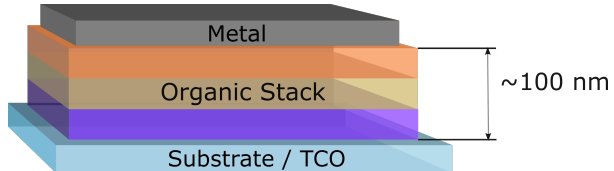


**Figure 2.1:** Basic layer diagram for OLED devices.

The organic stack of devices is typically 80 nm or more and consists of multiple layers. For most materials, deposition from the vapor phase at rates of 1 Å/s does not provide the time or energy needed to rearrange into a crystal, and thus yields amorphous films, showing minimal short and medium range order.<sup>1–4</sup> However, most materials will crystallize rapidly with annealing,<sup>5</sup> or slowly over time.<sup>6</sup>

Detailed device operation will be expanded upon in Chapter 3, but the goal of the layer stack is to efficiently form and recombine excitons. When voltage is applied, electrons are injected from the metal contact into the electron transport layer (ETL) and holes are injected from the ITO into the hole transport layer (HTL). Carriers transport through these layers to a region where exciton formation is designed to occur. This can be done in a variety of ways and is discussed in detail in Section 2.4, but most modern devices use a structure with a dedicated emissive layer (EML), as shown in Figure 2.2. In this type of device, the emitter molecule or guest, is doped at low concentration within a host matrix.<sup>7</sup> This composite film structure

is used because most emissive molecules show a reduction in  $\eta_{PL}$  with increasing concentration.<sup>8</sup> The host molecule is used to help transport charge to the emissive molecule and separate the guest molecules. The host molecule is designed to have a wider energy gap, making it energetically favorable for excitons to form on the guest molecule.

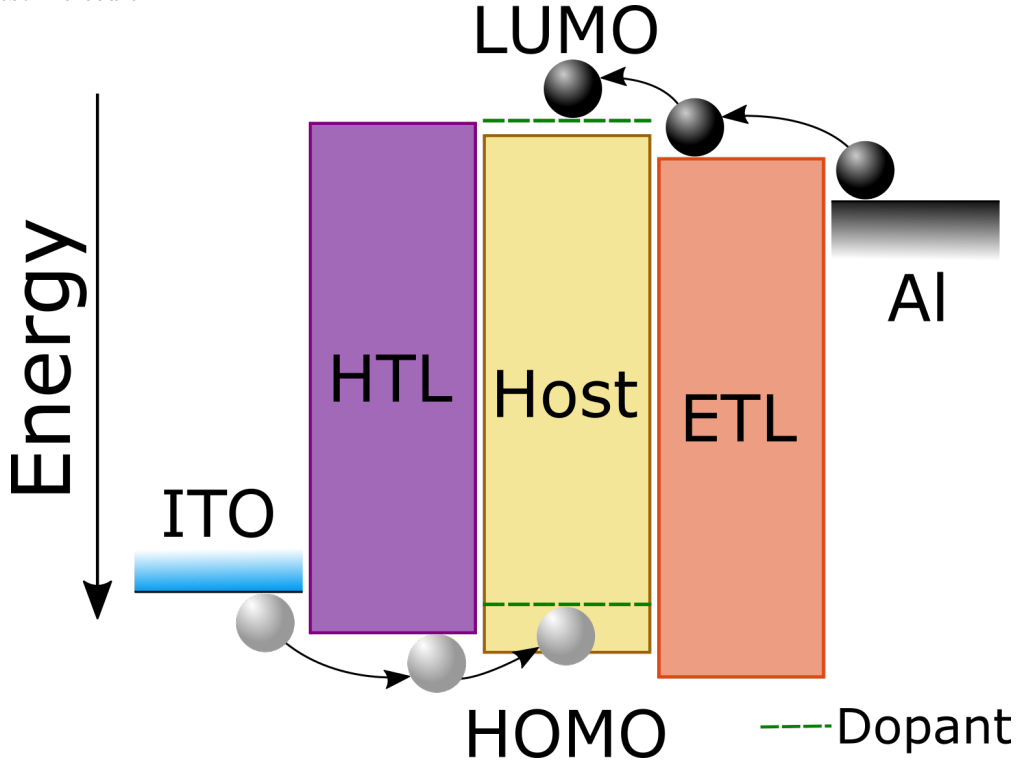


**Figure 2.2:** Energy level diagram of an OLED. Energy is shown in reference to the vacuum level. Electrons are shown in black spheres, holes shown in white.

The structure shown in Figure 2.2 is greatly simplified from most devices. Injection layers (HIL/EIL) are often used to aid in charge injection into the device between the electrode and transport materials. These materials will sit energetically between the electrode and the transport layer. To confine charges within the EML, blocking layers (HBL/EBL) are often used between the EML and the opposing transport layer. For example, a hole blocking layer would sit between the EML and the ETL and would have an energy level similar to the ETL, so electron transport would not be disrupted, but would have a high HOMO energy or a low hole mobility. These types of layers are often added as needed based on the energetic levels of the other materials in use.

### 2.1.1 Efficiency

Device efficiency is often thought of as a four component process as:<sup>9</sup>

$$\eta_{EQE} = \chi \eta_{PL} \eta_{EF} \eta_{OC} \quad (2.1)$$

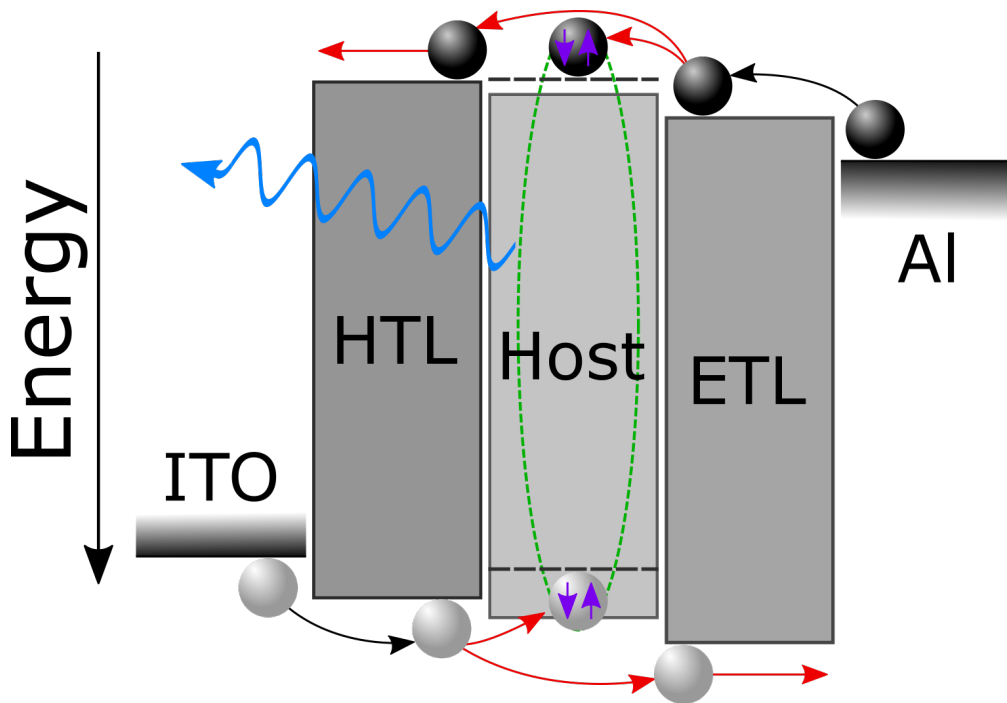


**Figure 2.3:** External Quantum Efficiency on energy level diagram.  $\eta_{OC}$  represented in blue,  $\eta_{PL}$  in green,  $\chi$  in purple, and  $\eta_{EF}$  in red.

The efficiency with which injected charges form excitons is the exciton formation efficiency,  $\eta_{EF}$  (traditionally called charge balance,  $\gamma$ ). This is competitive with charge loss through the device and is shown in red in Figure 2.3. In modern devices,  $\eta_{EF}$  can approach 100% at the maximum efficiency point. Electrically, excitons are formed in a 3:1 Triplet:Singlet ratio, as discussed in Chapter 1.2. The radiative spin fraction,  $\chi$ , captures the fraction of these formed excitons that are able to emit. For fluorescent materials,  $\chi = 1/4$  and for phosphorescent materials,  $\chi = 1$ . The photoluminescence efficiency,  $\eta_{PL}$  is the efficiency of photon generation from the radiatively allowed excitons and can reach 100%. The out-coupling efficiency,  $\eta_{OC}$ , is the fraction of photons that escape the device in the forward viewing direction, and is competitive with wave-guided modes and surface plasmons.<sup>10,11</sup> For most devices  $\eta_{OC}$  is the limiting process for efficiency, and typically is limited to 20-30%, but can be aided by enhancing films or layers.

## 2.2 Fabrication Processes

Substrates consist of glass precoated with indium-tin oxide (ITO). Prior to deposition, substrates are cleaned using 5 minutes each of sonicated Tergitol, water, and two cycles of acetone, followed by two cycles of boiling isopropanol. This is followed by a UV-ozone treatment for 10 minutes. Large area devices on patterned ITO are spin coated with a solution processed hole conducting planarizing layer. In my time in the group, this

started with Pedot-PSS and has transitioned to the more commercially used Plexcore AQ-1200. Pedot-PSS is water based and seemed more susceptible to treatment conditions prior to deposition, such as freezing. AQ-1200 has been a more reliable material. AQ-1200 has been replaced with AQ-1250, which appears to be the same formula, but with tighter control over consistency. For all solution processed layers, spin coating is done for 30 seconds at 3000 rpm, followed by a 30 minute bake at 150 °C.

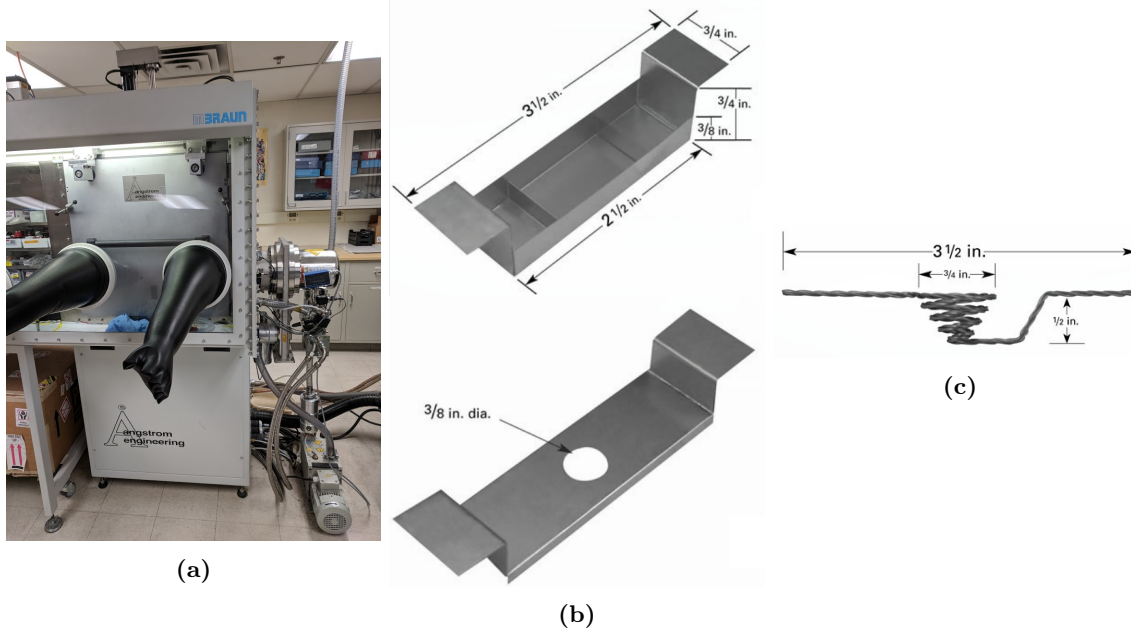


**Figure 2.4:** a. Angstrom vacuum chamber b. Organic deposition boat c. Aluminum deposition boat

Within our lab, the standard fabrication process for OLEDs is thermal evaporation at base pressures  $<10^{-7}$  Torr. This is done in an Angstrom Engineering vacuum deposition chamber from tungsten boat sources for organic materials, shown in Figures 2.4a and 2.4b, respectively. Material deposition rates can be measured using quartz crystal monitors (QCMs) during deposition. The absolute rate of material deposition can be calibrated by conducting ellipsometry on grown films to determine thickness. This chamber allows simultaneous deposition of up to 4 materials at a time. Co-deposition of materials allows for the creation of doped layers, which can even be varied with time to create graded composition profiles. For most devices, cathodes consist of 1 nm of lithium fluoride, from a dimple boat, followed by 100 nm of Aluminum, from the boat shown in Figure 2.4c.

For unpatterned devices, the whole substrate is coated in ITO, and device pixels are formed using a metal mask that defines the device area. In this case, to contact devices, contact must be made with the ITO for the anode and the Al cathode. A hard metal probe is used to contact the ITO by poking through the organic stack. However, the metal must be contacted without damaging the metal or underlying organic stack, as any damage would disrupt the device behavior, and at worst, short the contact to the ITO anode.

In order to contact the metal, a  $100\mu$  gold wire is used to gently contact the metal surface.

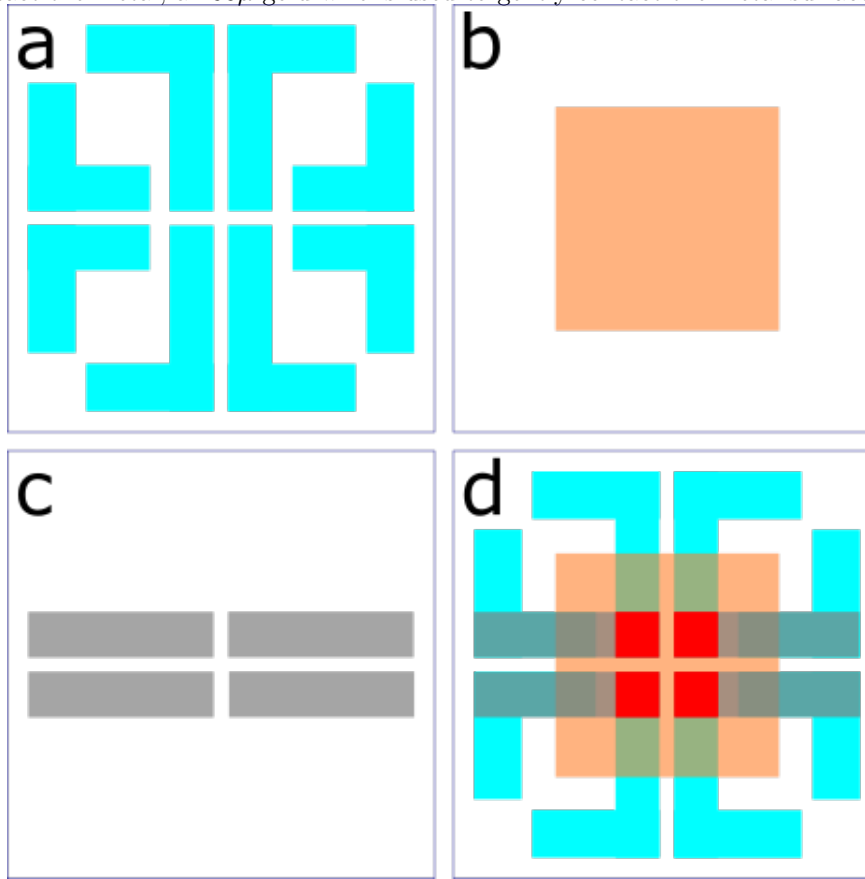


**Figure 2.5:** a. ITO Pattern b. Organic Mask c. Metal Mask d. Mask Overlays. Device area shown in red.

Patterned devices consist of a patterned ITO substrate with a corresponding patterned metal mask, where the intersection forms the device area. To ease contacting, an ITO pad is typically placed below the metal at the contact point outside of the organic deposition region as demonstrated in Figure 2.5. This method allows for contacting the device off of the device active area, and does not suffer from the difficulty of contacting and is essential for devices to be encapsulated. In this case, it is important to consider lateral transport within the HIL. A sharp edge on the ITO pattern can result in a discontinuity of the organic stack at the device edges and can frequently short the device with metal directly in contact with the ITO. To prevent this, a planarizing layer is used which minimizes the effects of ITO roughness and the discontinuity of the step edge. While this is effective, planarizing layers are designed to have high mobility and lateral conduction could become important as it may lead to shorting between the anode and cathode ITO pads. To prevent this in our devices, the planarizing layer is disturbed between the two pads in order to disrupt lateral transport.

For device lifetimes, to minimize oxygen exposure, devices are packaged. This is done before devices are exposed to oxygen levels outside of a glovebox. A UV cured epoxy seal is formed around the device active

area and is capped with a glass microscope slide cover slip. The epoxy is then cured with 3 minutes of exposure to a UV lamp. For extreme long lived devices or higher shelf life, a desiccant can be used, but this is not common in our lab due to the relatively short lifetimes that we are studying.

## 2.3 Characterization

Though numerous characterizations exist to analyze devices, the standard metrics of performance consist of current-voltage, luminance, and efficiency. Luminance is typically calculated in candelas per meter squared ( $cd/m^2$ ). There are three common efficiency metrics for devices, including the external quantum efficiency (%), the power efficiency ( $W/W$ ) and the luminance efficiency ( $lm/W$ ). Though dependent on field of study, for academic OLED interests, the most commonly explored metric is the external quantum efficiency ( $\eta_{EQE}$ ).

### 2.3.1 Current Voltage and Luminance

The current-voltage behavior of most OLEDs follows a diode-like current-voltage dependence. This is characterized by a weak dependence of current on voltage below some threshold, followed by a strong dependence at high voltage, as shown in Figure 2.6. In terms of device operation, at low voltage below turn-on (Region I), carriers do not have enough energy to make the transitions between molecular orbital energy levels and cannot be injected into the device. Soon after turn on, carriers are overcoming the injection barriers of the material stack and in an ideal device, forming a strong recombination current for light emission (Region II). In this region, the current is limited by carrier injection and follows an exponential dependence as carriers overcome the injection barrier potential.<sup>12</sup> At high voltage, injection barriers have been overcome and there is a charge buildup in the device which limits the current. This region is known as the space-charge limit and the current-voltage characteristic shows a power law dependence.<sup>12-14</sup> In a well formed device, luminance should closely follow current, as most current should be going to recombination and exciton formation.

For device brightness characterization, either optical power or luminance can be used. Optical power is simply a characterization of the total photon power exiting a device. This is typically calculated by measuring the total device light output using a large area photodiode. For optical power or optical power

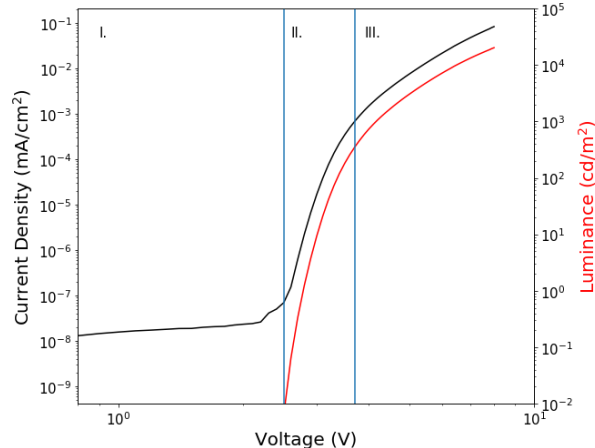


**Figure 2.6:** a. Device current voltage and luminance voltage behavior

density measurements, it is important to know the measured light producing region being measured. This can either be done by ensuring the total device area and all light output is measured, in which case the area of interest is the device area, or by measuring a known subsection of the device. The current output by the detector can be related to the incident optical power by the responsivity function of the detector, reported as a function of wavelength as  $W/A$ . A typical responsivity for a silicon detector is shown in Figure 2.7a.

Luminance is reported in candelas per meter squared ( $cd/m^2$ ), sometimes called a 'nit'. The candela is a measure of perceived light intensity per solid angle and is equivalent to 1 candle power. To measure luminance, the light output must be normalized to the wavelength dependent response of the human eye, known as the photopic response, shown in Figure 2.7b. This is typically done in one of two ways. The first method (employed by our group) is to use a spectrometer to measure the output light spectrum in Watts per nanometer. Then the spectrally averaged photopic response can be found for the light source of interest. Then, the output optical power can be measured by a simple photodiode and calibrated using the average photopic response. Alternatively, a photodiode can be filtered and modified so that the responsivity function matches the photopic response. In this case, the photodiode would directly output the luminance. Both methods are standardly used in research groups.<sup>15-17</sup>

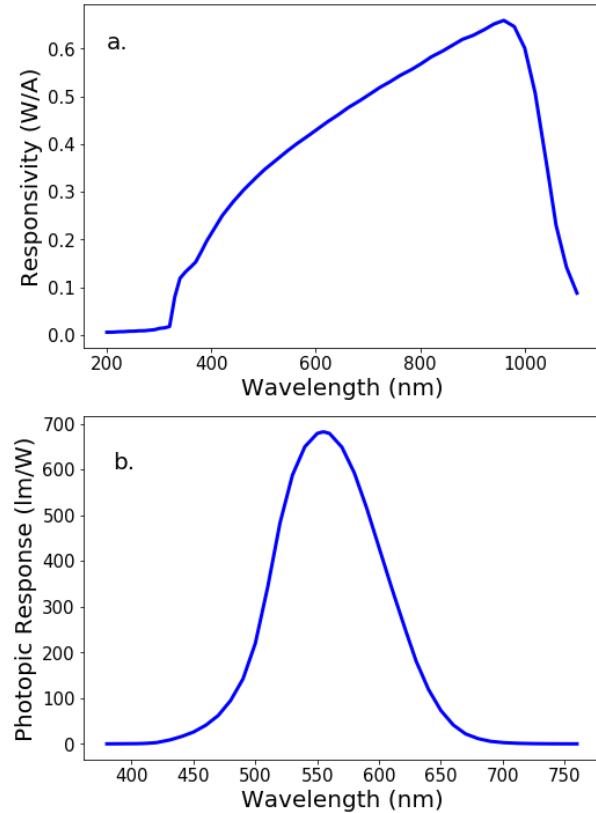


**Figure 2.7:** a. Silicon detector responsivity b. Photopic response

### 2.3.2 Efficiency

As mentioned previously, there are three common measures of device efficiency. The first is power efficiency, measured in  $W/W$ . This is straight forward to calculate given the previous discussion of measuring optical power. The luminance efficiency  $lm/w$  is related to the luminance output. The lumen is a measure of total light output and is related to the candela by  $1 \text{ lm} = 2\pi \text{ candelas}$ . A keen eye would note that the candela is normalized per solid angle and a factor of  $4\pi$  may be expected, but OLEDs are only able to emit in the forward direction.

The external quantum efficiency ( $\eta_{EQE}$ ) is a measure of photons exiting the device per electron injected. The photon flux out of the device can be calculated from the optical power by dividing by the average photon power,  $hf_{avg}$ , where  $f_{avg}$  can be calculated from the measured spectrum. The injected electron flux is simply  $I/q$  where  $I$  is the device current. The mathematical details of this model are discussed in detail by Forrest et al. [17].

### 2.3.3 Chromaticity

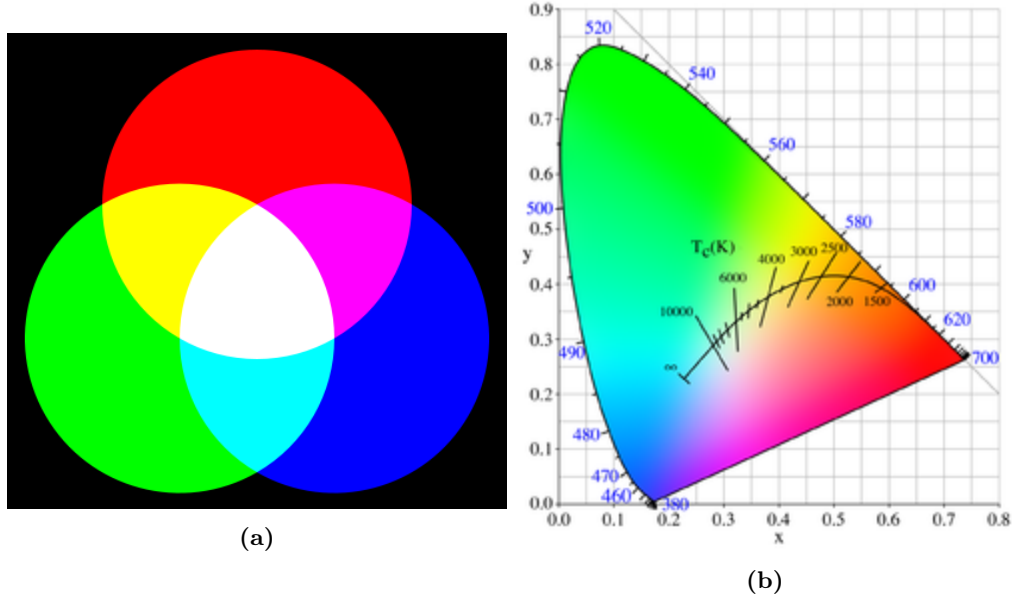


**Figure 2.8:** a. Simple color addition diagram. b. CIE  $xyY$  color space.

In addition to the efficiency and brightness characterization, the quality of light can also be assessed, known as chromaticity. This is very important for both displays and lighting applications. This characterization is standardly done using the CIE chromaticity diagram and  $xyY$  color space.<sup>18–20</sup>

The chromaticity of an emitter is defined to reflect the sensitivity of the human eye. In the eye, there are two color sensing cones, roughly corresponding to red, green, and blue. The wavelength sensitivity of these cones for red, green, and blue are defined as  $\bar{x}(\lambda), \bar{y}(\lambda)$ , and  $\bar{z}(\lambda)$ , respectively. A three dimensional color-space is then defined to define any color using

$$A = \int_{\lambda} L_{e,\Omega,\lambda}(\lambda) \bar{a}(\lambda) d\lambda \quad (2.2)$$

where  $A$  and  $\bar{a}$  are  $X, Y, Z$  and  $\bar{x}, \bar{y}, \bar{z}$ . These three dimensional coordinates are able to accurately describe the light, but are not very useful for visualizing the color-space. Therefore, the brightness is normalized out, leaving us with two color coordinates and a brightness value. Since our eye is most sensitive to green stimulus,

the  $Y$  coordinate is taken to represent the brightness. The color coordinates can be normalized by

$$a = \frac{A}{X + Y + Z} \quad (2.3)$$

where  $a$  and  $A$  are  $x, y, z$  and  $X, Y, Z$ . Note that  $x$  is a new color coordinate, not the standard observer sensitivity,  $\bar{x}$ . This remapping still has three coordinates, but here,  $z = 1 - x - y$ . Therefore, the color can be represented using just  $x, y$ . This can be seen in Figure 2.8b, where the perimeter is defined by mapping single wavelength light through these coordinate transformations. All possible visible colors are defined within the locus, and  $x, y$  coordinates are shown on the axes. For white light, the color temperature is calculated in reference to a black-body emission and is also shown in Figure 2.8b. While sophisticated in calculation, it is important to note that this concept of color-space is simply an extension of the color addition shown in Figure 2.8a.

### 2.3.3.1 RGB

For display applications, a single red, green and blue emitter are used, each of which will have  $x, y$  coordinates which can be expressed on the CIE diagram. Using this method, only colors within the enclosed triangle can be expressed, making it critical for a vibrant display to maximize the area of this triangle. Various phone displays are shown in Figure 2.9, with the pure color components being generated using a RGB color picker application. Interestingly, the iPhone SE, the only phone not using an OLED display, shows the worst response in the green, a clear advantage of OLED color representation. The scatter points in this figure represent individual pixels measured in the course of this thesis.

One limit of RGB color representation is that it is not consistent across displays. For example, the RGB coordinate  $(0,1,0)$  looks different on the Google Pixel versus the iPhone SE due to their different CIE coordinates. To account for this, display RGB values can be calibrated to accurately represent the CIE coordinates. However, in doing so, the color space available to the display is shrunk and the full color range of the display cannot be used. This is an important issue in commercial devices where consumer demands must be carefully considered with respect to the trade off between accurate and vibrant colors. This trade off

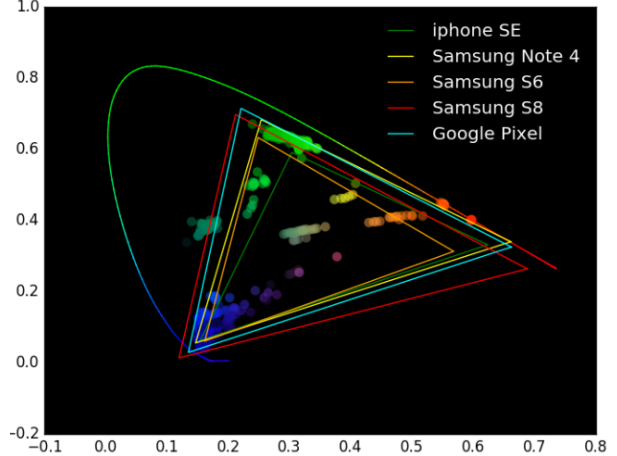


**Figure 2.9:** Various phone display limits shown on CIE coordinates

was clearly seen in the release of the Google Pixel 2, where consumers complained about dull colors because the manufacturers used a calibrated color space.<sup>21</sup>

## 2.4 Historical Development

### 2.4.1 The First OLEDs

Early interest in organic materials was generated based on use for organic laser dyes and the high fluorescence efficiency demonstrated.<sup>23-25</sup> Early attempts at producing electroluminescent devices tried contacting organic crystals, but required extremely high voltages to produce any light.<sup>26,27</sup> The first successful OLED was demonstrated by Tang and VanSlyke [22] in 1987, one of the first to utilize vacuum deposition for thin films. This was a bilayer device, with the structure shown in Figure 2.10, using TAPC at 75 nm thick and Alq<sub>3</sub> 60 nm, responsible for the emission of the device, centered around 550 nm. These devices achieved  $\eta_{EQE} \approx 1\%$  and showed rapid degradation.

In fluorescent cells,  $\chi = 0.25$  and without out-coupling enhancement  $\eta_{OC} \approx 0.20$ , leaving a maximum  $\eta_{EQE}$  of just 5%. Doped films were investigated soon after these initial findings in order to capitalize on the improved  $\eta_{PL}$  at low concentration.<sup>28</sup> This host with emissive guest system is utilized by almost all devices.

### 2.4.2 Phosphorescence

OLEDs saw a massive improvement in possible efficiency in 1998 with the introduction of phosphorescent dyes.<sup>9</sup> These dyes use a heavy metal atom to create a metal-ligand charge transfer state, which allows mixing of the singlet and triplet states, and thus emission from the triplet exciton. With all excitons able to emit, including the triplet state, the internal quantum efficiency ( $\eta_{IQE}$ ) raises to 100%. These devices utilized the red phosphor PtOEP in conjunction with the laser dye DCM2. This work comments on quenching at high current of the phosphor, a continuing problem which will be discussed further in Section 2.5.<sup>15,29</sup> Pure red and green emission devices utilizing only a phosphorescent dopant were developed soon after, along with the development of the ubiquitous green emitter, Tris[2-phenylpyridinato-C<sup>2</sup>,N]iridium(III) (Ir(ppy)<sub>3</sub>), shown in Figure 2.11.<sup>30,31</sup>

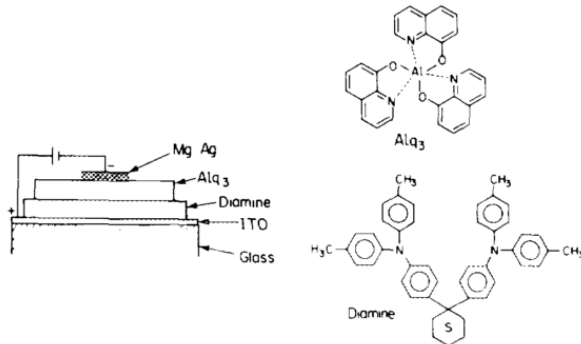


**Figure 2.10:** Structure of the first OLED cell from Tang and VanSlyke [22]. Diamine is commonly referred to now as TAPC.

Since the realization of the phosphorescent OLED, internal quantum efficiencies nearing 100% for green, red, blue, and white devices have been demonstrated.<sup>32,33</sup> With high efficiency achieved, attention has shifted to maximizing lifetimes.<sup>34</sup> Despite the high efficiency of blue phosphorescent devices, lifetimes still remain limiting and blue fluorescent materials are still used in commercial technologies.

### 2.4.3 Thermally Activated Delayed Fluorescence

While phosphorescent devices have been able to demonstrate high efficiency necessary for commercialization, this has come at a cost. Namely, in the use of expensive and rare heavy metal atoms, such as Ir(III), Pt(III), and Os(II).<sup>36</sup> In order to utilize the triplet excitons, reverse intersystem crossing is utilized. Chapter 1.2 and Figure 1.1 discuss intersystem crossing as an energetically favorable process as the triplet is lower energy than the singlet. However, if molecules are designed where the singlet and triplet energies difference ( $\Delta E_{ST}$ ) is small ( $< 1\text{eV}$ ), thermal energy can make the reverse intersystem crossing competitive with intersystem crossing ( $k_{RISC} \approx k_{ISC}$ ). This allows for Thermally Activated Delayed Fluorescence (TADF), shown in Figure 2.12.<sup>35,37,38</sup> TADF materials are a rapidly developing technology that has shown many benefits for efficiency, and rules are being established for molecular design.<sup>16,35,37–52</sup> These materials are also being investigated for benefits to device lifetime.<sup>53,54</sup>

## 2.5 Efficiency Roll-Off

In operational OLEDs, it is almost universally observed that efficiency reduces at high brightness and current density, an affect known as the efficiency roll-off, demonstrated in Figure 2.13.<sup>15,29,55–68</sup> This has been extensively studied and largely attributed to the bimolecular quenching processes discussed in Chapter 1.2,

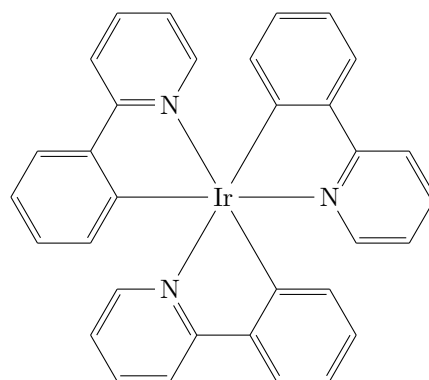


**Figure 2.11:** Molecular structure of the green phosphor,  $\text{Ir}(\text{ppy})_3$

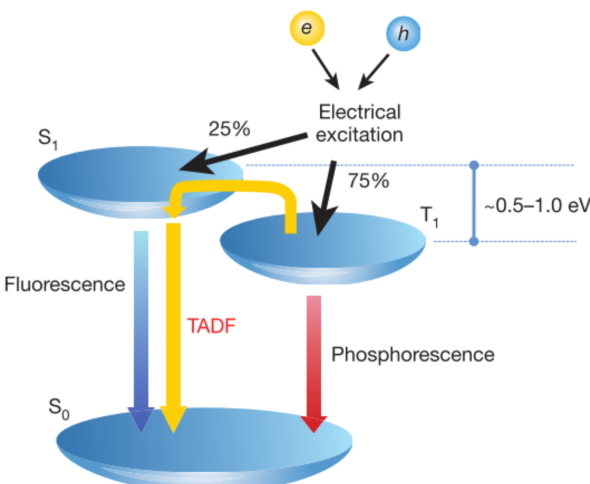


**Figure 2.12:** Reverse intersystem crossing for TADF materials. Figure taken from Uoyama et al. [35].

though exciton formation efficiency ( $\eta_{EF}$ ) is also known to contribute at a lesser degree. This is detrimental to commercialization as high brightness is a necessity for display and lighting applications. The bimolecular quenching at high brightness is also detrimental to device lifetime because quenching processes produce hot excited states that release excess energy into the device, which is thought to be a key factor in molecular degradation.<sup>69–71</sup> Development of electrically pumped organic lasers has proved unsuccessful because the exciton densities required to achieve population inversion lead to excessive quenching and the inability to create stimulated emission.<sup>9,72–76</sup>

Devices are often investigated to try to reduce the roll-off, often through the broadening of the exciton recombination zone.<sup>16,32,41,77–82</sup> These devices have not been successful in removing the roll-off, but rather in reducing it. Section 2.1 discussed the characterization of quantum efficiency using a four component efficiency model. This model fails to reproduce the roll-off behavior as it does not account for quenching. Modeling the efficiency roll-off has been the study of numerous works and is the motivation for Chapter 3.<sup>15,29,55,59</sup> These models center around a differential equations model for exciton dynamics, such as:

$$\frac{dn_{ex}}{dt} = -\frac{n_{ex}}{\tau} - \frac{1}{2}k_{TT}n_{ex}^2 - k_{TP}n_{pol}n_{ex} + G_{ex} \quad (2.4)$$

where  $n_{ex}$  is the exciton population density,  $\tau$  is the exciton lifetime,  $k_{TT}$  is the triplet-triplet annihilation rate,  $k_{TP}$  is the triplet-polaron quenching rate,  $n_{pol}$  is the charge density, and  $G_{ex}$  is the exciton generation rate. Here we can see that the natural lifetime is competitive with the bimolecular quenching rates, and at high exciton and charge density, the second order dependence of the quenching terms allows them to dominate. This reduces the relative number of excitons that are decaying via the radiative rate, thus decreasing the efficiency. These models have been successful in characterizing the rate constants and describing the roll-off behavior. For further details, see Chapter 3.

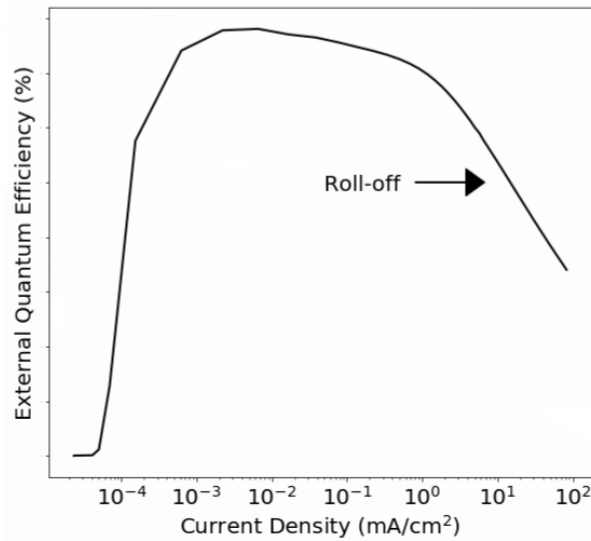


**Figure 2.13:** Efficiency roll-off as a function of current density

## 2.6 Recombination Zone Characterization

Both degradation and bimolecular quenching can be highly dependent on the exciton density and location, known as the exciton recombination zone (RZ).<sup>15,29,60,69,83–86</sup> Therefore, it is important to be able to characterize the spatial profile of excitons. This has been done by a variety of researchers using thin doping layers of a sensitizer molecule.<sup>68,70,80,85–87</sup>

In these experiments, the dopant is used to efficiently siphon excitons off of the emitter molecule and onto the sensitizer. In order to do this, Förster transfer to the sensitizer must be efficient, requiring significant overlap of the emitter emission and the sensitizer absorption. Erickson and Holmes [68] looked at the spatial extent of Förster transfer and found that transfer was efficient within a  $< 4$  nm radius. To characterize the recombination zone, sensitized layers are used and the effect of the local perturbation of the exciton density can be measured. Translating the sensitized strip across the device as shown in Figure 2.14 allows for comparison of the relative effects and thus determination of the relative magnitude of the recombination zone. The Förster radius gives the maximum spatial resolution that can be obtained using this strip translation.

A quenching (non-radiative) or emissive (radiative) sensitizer can be used for these experiments. With a quenching sensitizer, if the recombination zone overlaps with the sensitizer position, emission is lost and the efficiency is reduced. The reduction in EL intensity can be quantified by the EL ratio of the sensitized intensity compared to the unsensitized intensity,  $\beta$ .  $\beta$  is directly proportional to the unquenched excitons, therefore  $1 - \beta$  gives the ratio of quenched excitons.

For emissive sensitizers, given the requirement of emission-absorption overlap, red sensitizers are used. For simplicity, the sensitizer should show spectral separation of the emission from the emitter. The intensity of the sensitizer emission is a direct measure of the local exciton density. However, since the out-coupling is so strongly dependent on emitter position in the EML, it is essential to correct the intensity using a calculation of  $\eta_{OC}$ , discussed in Chapter 8. One may note that the quenching sensitizer method should also require out-coupling correction, but since the emission is not spatially isolated, calculation of the spatially averaged out-coupling efficiency would require prior knowledge of the recombination zone shape and therefore cannot be done. Emissive sensitizers often rely on the use of Pt(II) complexes, such as PtOEP or PtTPTBP.<sup>85,87</sup> Compared with Ir(III) complexes, Pt(II) shows a much longer exciton lifetime, and is therefore far more susceptible to bimolecular quenching.<sup>65</sup> If the sensitizer is in a regime of bimolecular quenching during the measurement, a compressed version of the recombination zone will be measured. This can be difficult to avoid at high current densities that may be of interest for measurement.

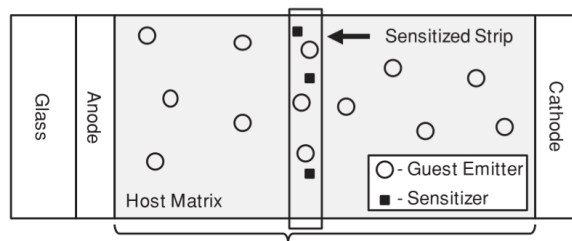


**Figure 2.14:** Recombination zone measurement architecture. The curly brace indicates the device stack. Figure taken from Erickson and Holmes [68]

An advantage of the emissive sensitizer is that the data generated can be analyzed either using the quenched ratio or using the emitted intensity. This can be helpful for quantifying error in the method, and is demonstrated in Figure 2.15. Here, we see the spatial dependence of the recombination zone for an architecture peaked at the ETL interface. Notice that the emissive sensitizer, PtTPTBP shows a less exaggerated RZ for all current densities. This is likely due to bimolecular quenching on the sensitizer, which is stronger at the higher exciton densities present at the ETL interface.

When constructing these sensitizer layers, there are two popular methods. First, the EML can be reproduced exactly with the addition of a light doping of the sensitizer. This creates a strip that exactly replicates EML, but increases the difficulty of the growth, requiring one more material in a co-deposition. An alternative is to use an extremely thin deposition of the sensitizer molecule in isolation, known as delta doping. A deposition of 1 Å is used, which since the molecular radius of the deposited material is larger than that, in reality, a discontinuous layer is produced. When the EML is continued on top of this discontinuous layer, this is equivalent to an extremely narrow strip of a mixed layer. This is advantageous because it makes the deposition much easier and creates a very narrow strip. However, it can be difficult to control the doping percentage as it is difficult to accurately measure films this thin. No quantification of error on these types of doping have been reported.

In order to accurately compare the recombination zone intensity, it is essential to ensure that no differences in the transport and injection properties occur with the introduction of the sensitizer. Since the sensitizer molecules will likely result in a trap state, it is essential to keep doping concentrations low, on the order of 1%. Evidence of minimal interference on the electrical properties by the sensitizer is provided by the current-voltage behavior. If the current-voltage characteristic is within error between all of the sensitizer devices, it is often assumed that the device is representative of the control.<sup>68</sup>

## 2.7 Single Carrier Devices

When investigating device behavior, it is often important to characterize the behavior of a single charge carrier.<sup>29,88,89</sup> To do this, devices have to be created that allow passage of only one carrier. This can be accomplished by establishing energetic barriers for the opposing charge, disallowing injection, or through heavy imbalance of mobility. Examples of hole and electron only devices are shown in Figures 2.16a and

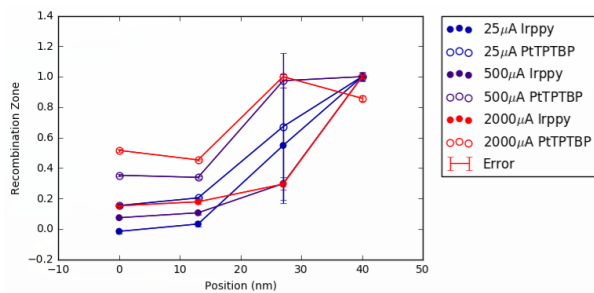


**Figure 2.15:** Recombination zone comparison for an emissive sensitizer analyzed using the quenched ratio and the emitted ratio as a function of current density.

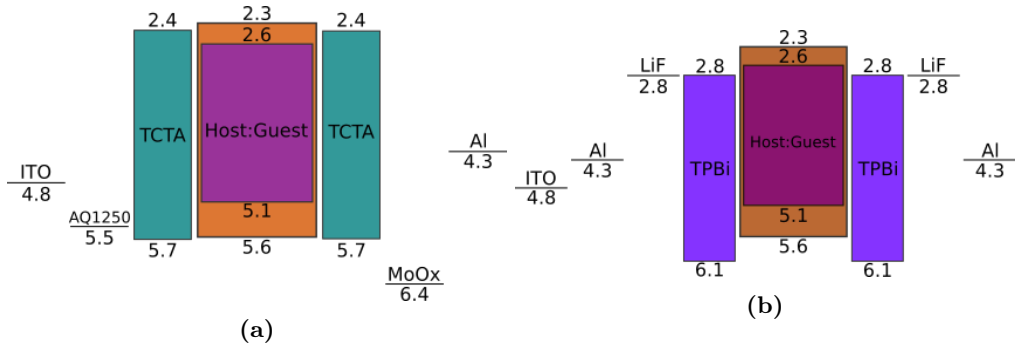


**Figure 2.16:** a. Hole only device. b. Electron only device.

2.16b. In Figure 2.16a, MoO<sub>x</sub> provides a deep energy barrier for electron injection. Additionally, TCTA is used, which has a high hole mobility and lower electron mobility, along with well aligned HOMO levels, encouraging hole transport. In this device, positive bias is applied to the ITO contact, for no particular reason other than tradition and that it works well. In Figure 2.16b, the ITO contact does not facilitate electron injection. Therefore, A thin layer of aluminum is doped on top of the ITO, along with LiF, which adjusts the interface energy to more align with electrons and block holes. TPBi is used to provide a transport barrier for holes and facilitate electrons. The same LiF-Al contact is used to promote electron injection. In this device, better current-voltage characteristics are seen with positive bias applied to the ITO, in my experience. This may be due to the properties of LiF at the ITO side interface, since in the experiments using this structure, a vacuum break occurred at that interface with LiF exposed. We have not investigated the differences in manufacturing techniques to explore this further.

Single carrier devices have been heavily investigated and modeled for their polaron and current-voltage behavior.<sup>12-14</sup> This can be used to help in analyzing these devices for dynamics and comparison to full device behavior.

## 2.8 Operational Lifetime

In typical lifetime characterization, devices are degraded while held at constant current density, recording the resulting luminance loss and voltage gain as a function of time. The lifetime is then reported as the time to reach some arbitrary fraction of the initial luminance.

### 2.8.1 Degradation Mechanisms

As degradation studies are an ongoing an extensive area of research, this section does not represent an all inclusive picture of degradation mechanisms. However, it does seek to outline the dominant mechanisms ob-

served in typical devices. In the most empirical case, the degradation of an OLED can be viewed wholistically as a stretched exponential curve with minimal physics.<sup>6,90</sup>

$$\frac{L(t)}{L_0} = \exp(t/\tau)^\beta \quad (2.5)$$

This approach is able to reproduce the decay behavior relatively well and the scaling with luminance, but only describes the decay by attributing behavior to emissive centers.

To delve deeper, individual degradation pathways must be investigated. These are typically separated into external and internal mechanisms.<sup>6</sup> External mechanisms are due to influences outside of the active materials impacting the device behavior, and are typically easy to identify, though avoiding is still a challenge, especially in long lived and large area commercial devices.<sup>91</sup> Internal or intrinsic degradation mechanisms are due to physical and chemical processes within the device. These processes can be significantly more difficult to investigate and various analytical techniques are often used to observe this behavior, as discussed in Section 2.8.3. Scholz et al. [6] goes into extensive discussion of observed degradation methods. In the research presented in this thesis, no chemical analysis of degradation products and molecular composition changes was done. Because of this, for the purposes of this discussion, physical degradation pathways, rather than chemical degradation mechanisms will be discussed. This type of analysis identifies sensitivity within the device to various influences and can potentially identify the rate limiting molecules, but does not show the degradation chemistry. The following sections seek to identify the most widely observed degradation mechanisms.

### 2.8.1.1 External: Dark Spots and Delamination

One of the most widely observed and characterized degradation phenomena is the formation of dark spots.<sup>94–97</sup> This has been long attributed to delamination of the cathode, assisted by water and oxygen contamination or pinholes in the cathode.<sup>92,93,97–99</sup> Around an impurity under the cathode, a hot spot, or a cathode pinhole, the metal starts to delaminate from the underlying organic stack, forming a bubble.<sup>99–101</sup> The field distribution around these dark spots creates high current around the edges, creating local high brightness regions. This causes the dark spot to grow at an accelerated rate, further accelerating degradation.<sup>100–102</sup>

Despite the long history and understood mechanism, dark spots continue to be a major problem in manufacturing of large area lighting panels.<sup>91</sup> The methods for preventing dark spots are largely understood, though control can be difficult. It has been found that carefully controlling vacuum levels along with oxygen and moisture exposure during manufacture helps to prevent dark spot formation from oxygen and moisture under the cathode. After manufacturing, oxygen and moisture can still get into the device through pinholes

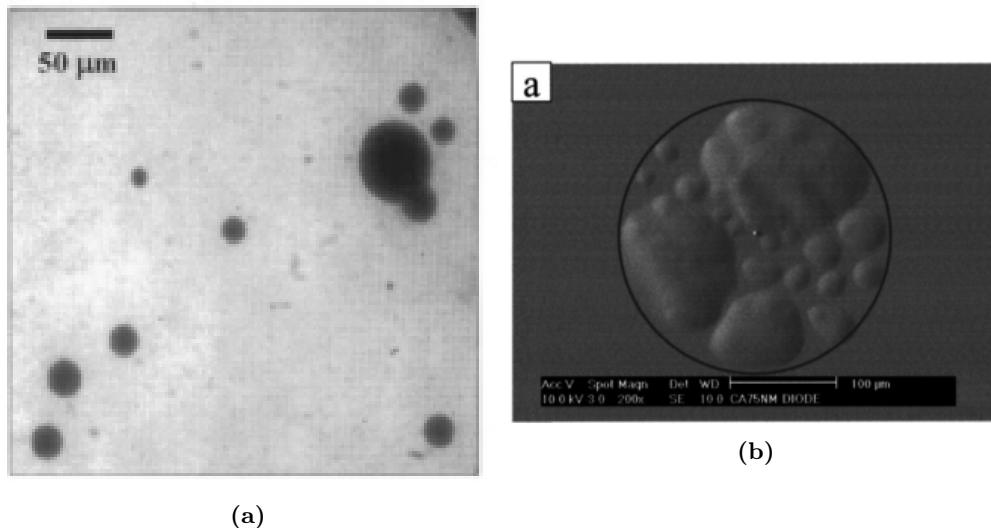


**Figure 2.17:** a. Dark spot in PL on an active device area, taken from Kolosov et al. [92]. b. Cathode bubbling where delamination has occurred under SEM, as shown in Wang et al. [93]

in the cathode, but this can be mitigated by careful packaging under a nitrogen environment. For long lived devices, the addition of a moisture desiccant within the packaging further decreases dark spot formation.

### 2.8.1.2 Exciton and Polaron

Most degradation mechanisms within a device are facilitated by the exciton and polaron population.<sup>6,69,84,86,103,104</sup> These excited particles within the device provide the excess energy that is responsible for breaking bonds and facilitating the chemical processes that cause molecular degradation. Reducing the exciton density by expanding the exciton recombination zone has been shown to extend lifetime.<sup>86,105–114</sup> Despite this knowledge, high exciton densities are still often needed due to high brightness of devices, which can not be fully counteracted by continuing to extend the recombination zone. In fact, most reduction in lifetime with brightness is attributed to increased exciton and polaron density.<sup>6</sup> In addition, it is often suggested that current is not uniform and typically confined to narrow pathways through the device.<sup>115</sup> This causes locally high exciton and polaron densities, even with well designed injection and transport for a wide RZ.

### 2.8.1.3 Interfaces

Some devices have shown sensitivity to charges and excitons at material interfaces within devices.<sup>15,116</sup> Through single carrier device investigation, some materials have been shown to be sensitive to conduction of one type of carrier.<sup>117</sup> In other cases, a buildup of charge or exciton density can occur at an interface, greatly increasing the degradation rate locally at the interface.<sup>118,119</sup> This type of degradation can result in the formation of Non-Radiative Recombination Centers (NRRCs).<sup>118,120–122</sup> NRRCs are cited, typically

of degraded molecules, that are able to recombine electrons and holes through a dark state who's emission is not seen. The higher density of trapped charge at an interface can lead to formation of exciplex and transport layer excitons at the interface.<sup>116</sup> Transport layer excitons can be detrimental to device behavior due to their UV energies, especially when combined with polarons, leading to bimolecular quenching and hot excitons that can be more damaging than the presence of excitons or polarons on their own.

Interfacial degradation is also an exciton and polaron driven process, but bares the critical distinction of sensitivity to location. In materials with known interface and single carrier sensitivity, it is important to engineer the exciton profile away from these interfaces to extend lifetime, as shown in my work, Hershey and Holmes [15], discussed in Chapter 5. This is contrary to the typical thought that only a broad recombination zone is important, discussed in the previous section. Some devices even show sensitivity to both exciton density and recombination zone position, again, discussed in 5.

### 2.8.2 Luminance Scaling

For commercially relevant devices, where the time to reach 50% of the initial luminance,  $t_{50}$  can be tens of thousands of hours, it is impractical to test devices under their intended operating conditions. Instead, lifetime testing can be done at an increased luminance from the true operating condition.<sup>6</sup> This can dramatically reduce the testing time of devices. The lifetime at other luminances can then be found using the scaling relation

$$L_0^n t_x = C \quad (2.6)$$

where  $L_0$  is the initial luminance,  $n$  is a scaling factor characteristic to the device, and  $C$  is a constant. To utilize this relation, several lifetimes are obtained at luminances above the operating condition in order to experimentally obtain a value for  $n$ . Subsequently, the lifetime of interest can then be extrapolated.

While widely used and observed, caution should be observed in the application of this relation. A variety of degradation mechanisms have been attributed to OLED behavior, as discussed in Section 2.8.1. All of these mechanisms are subject to different temporal dependences and have a variety of degrees of understanding to their functional dependence on time and luminance. At different luminances, different mechanisms may be dominant. For example, single excitonic processes may be dominant at low luminance, but may be overtaken by a bimolecular process at high luminance. The fact that OLEDs are frequently subject to several degradation mechanisms throughout the decay only further complicates the issue. The very idea of scaling law for all devices and at all current densities is unsound, and should be treated as a loose prediction. Over and underestimates of lifetimes using this relation are observed when trying to predict

actual lifetimes.<sup>123,124</sup>

### 2.8.3 Analysis Techniques

To expand on the luminance as a function of time, various analytical techniques are used to illuminate the degradation mechanisms. These can largely be divided into chemical analysis, modeling, and spectral characterization. These techniques offer valuable and unique insight, and are often used in combination for degradation analysis.

#### 2.8.3.1 Chemical Analysis

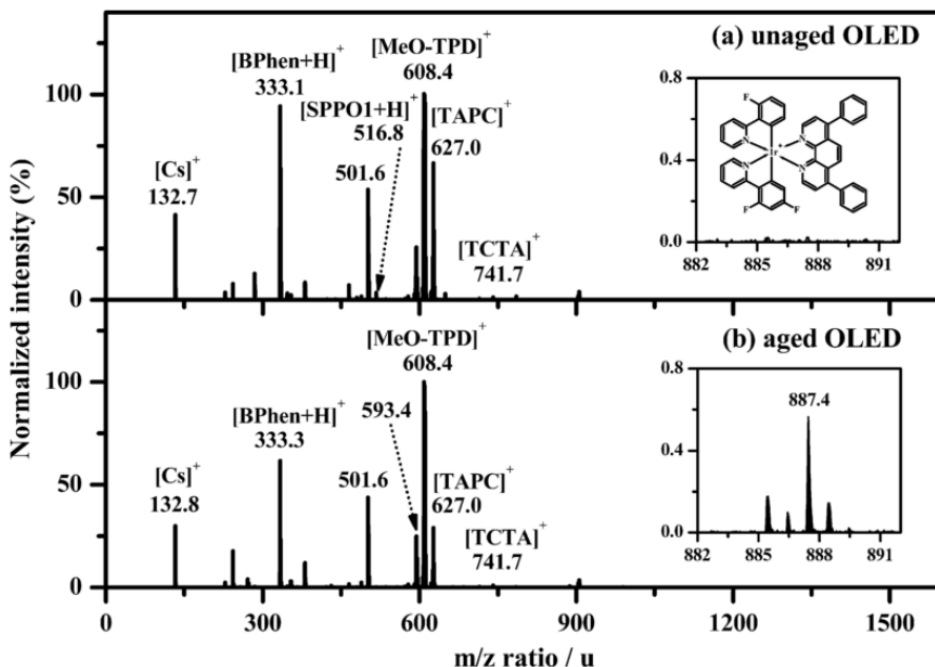


**Figure 2.18:** Mass spectroscopy data taken from Seifert et al. [125]

Perhaps the most obvious approach is to look directly at the chemical composition of degradation products and use this to inform on what molecules are degrading. A standard approach for doing this is Laser desorption/ionization time-of-flight mass spectroscopy (LDI-TOF-MS).<sup>125–127</sup> With this technique, a laser is used to ionize the sample material, and time-of-flight is used to characterize the molecular weight to charge ratio. An example of this data can be seen in Figure 2.18, taken from Seifert et al. [125]. Here, an unaged and aged sample are compared and peaks from known source material are identified. Differences that are seen are attributed to degradation, and can be compared to the expected spectra of proposed degradation products. In this case, a BPhen and FIr6 molecule have combined to form a new molecule. It is important to note that despite degradation to 15% of the initial luminance, the molecular signatures of degradation products are extremely weak, as seen by the scale on the inset in Figure 2.18. This is a common problem for

chemical techniques. In devices, the active material stack is only a few monolayers thick and small amounts of degradation product can have a large impact. Given the extremely low concentration and limited sample material, it can be difficult to do chemical analysis. Even at heavy degradation, if several degradation products are present, none may be in high enough concentration to be observed. Despite this drawback, understanding of results is very straight forward, making this a promising technique.

High performance liquid chromatography (HPLC) can also be used to view degradation products.<sup>122,128</sup> In HPLC, sample products are dissolved in a solution and filtered through a distillation column. Components can be categorized based on their transit time through the column. This technique offers similar results, but suffers from several drawbacks, namely that it can be difficult to dissolve all of the materials in a devices, and that identification of compounds requires a pure sample of the degradation product to serve as a calibration for the column.

Despite the direct interpretation of results, chemical techniques do have several drawbacks. First of all, these processes can be expensive and time consuming to perform, making it difficult to apply to large scale optimization of devices. In addition, it does not provide any temporal resolution on a single device, since this is an entirely destructive technique. This makes it difficult to understand any kinetic.

### 2.8.3.2 Modeling

Modeling efforts have been used to try to understand the functional dependence of exciton density dependence and attribute this to a material dependent rate constant.<sup>69,70,87,129</sup> All of these works model the exciton population as a function of time using the equation:

$$\frac{dN_{ex}(x,t,t')}{dt} = \gamma n(x,t,t')p(x,t,t') - \frac{N_{ex}(x,t,t')}{\tau} - K_{DR}Q(x,t')N(x,t,t') \quad (2.7)$$

where  $N_{ex}$  is the exciton density,  $n, p$  are the electron, hole densities,  $\gamma$  is the Langevin recombination rate,  $\tau$  is the exciton lifetime,  $K_{DR}$  is the defect quenching rate, and  $Q$  is the defect concentration. In this model,  $t$  is the short term dynamics, while  $t'$  represents the degradation scale evolution of parameters. The electron and hole populations are fixed to form a predetermined recombination zone shape. The generated defects serve as first order quenchers to the exciton population, as well as trap states that modify the recombination zone along with charge densities.

$$\frac{dQ(x, t')}{dt'} = \begin{cases} K_X n(x, t'), & K_X p(x, t') \\ K_X N(x, t') \\ K_X N^2(x, t') \\ K_X N(x, t')n(x, t'), & K_X N(x, t')p(x, t') \end{cases} \quad (2.8)$$

Applying this model for each of these mechanisms independently, then comparing the fitted results should indicate the dominant defect generation process. Giebink et al. [69] find for their device that exciton-polaron processes are dominant, though this process is likely system dependent. This model allows fitting of luminance and voltage behavior as a function of time and luminance, which are shown to be consistent. However, this model has a large number of rate constants that cannot be measured independently, and is largely over-parameterized. Caution must be taken with these results as they do not suggest a unique explanation of the physics happening in the device.

### 2.8.3.3 Spectral Characterization

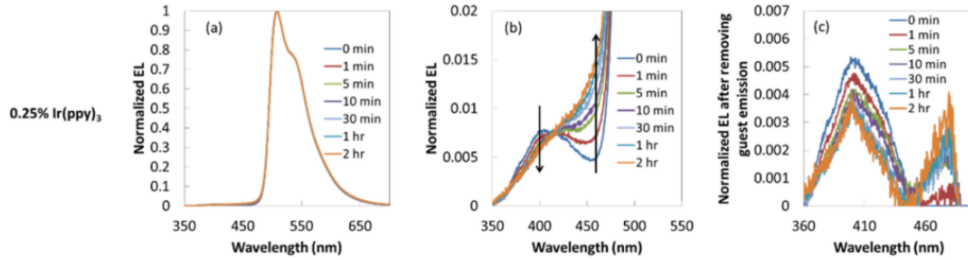


**Figure 2.19:** Emission from  $\text{Ir}(\text{ppy})_3$  and CBP, as reported by Zhang and Aziz [103] a. All emission, b. Emission shoulder, showing CBP emission, c. CBP emission with  $\text{Ir}(\text{ppy})_3$  background subtracted.

The electroluminescence spectra can also provide a large amount of information about the degradation state.<sup>6</sup> This is typically done in two schools of thought: intentional emission and observation of weakly emissive states. Weakly emissive states and host emission have been used to characterize aggregation within the host and guest molecules.<sup>103,130–132</sup> Within these studies, emission from the phosphorescent guest is characterized as a function of time, but careful inspection reveals weak emission from the host, as seen in Figure 2.19.<sup>103</sup> In this figure, the weak CBP emission can be seen in the shoulder of the guest emission, and the losses during degradation characterized. This study finds that host molecules are aggregating due to exciton and positive polaron interactions, accelerating degradation.

Another use of this technique is to track changes in the exciton recombination zone. This has been used in simplified bilayer devices where changes in relative peak intensities between two emissive species can indicate a shift of the RZ from one side of the device to the other.<sup>132,133</sup> This type of spectral characterization provides the temporal behavior of degradation that chemical analysis is lacking, but does not relate to

physical processes within the device quantitatively, at least directly. In fact, the understanding of physical mechanisms from the spectral changes can be far from straight forward.

Spectral characterization has been used recently as an extension of a modeling approach by Coburn and Forrest [70], to interesting effect. In this study, characterization of the exciton confinement within the emissive layer is desired. To study this, sensitizer doping layers are used outside of the emissive layer to probe for exciton leakage, using the red phosphor PtOEP, with emission shown in Figure 2.20. Using PtOEP, weak emission is seen in both cases, but is shown to increase in magnitude on the ETL side during degradation. This could indicate a decrease in exciton confinement, but would also be the case if holes were more efficiently leaking through the device. To rule out hole leakage, a fluorescent dopant is used, which would not be able to receive diffusing triplet excitons. Using DCM2, a fluorescent dopant, no increase in emission is seen, indicating that exciton confinement, not hole leakage, is responsible for this behavior. This approach of using modeling in combination with a spectral technique is very promising at providing both more information to aid in modeling, and a more physical understanding to the spectral techniques.

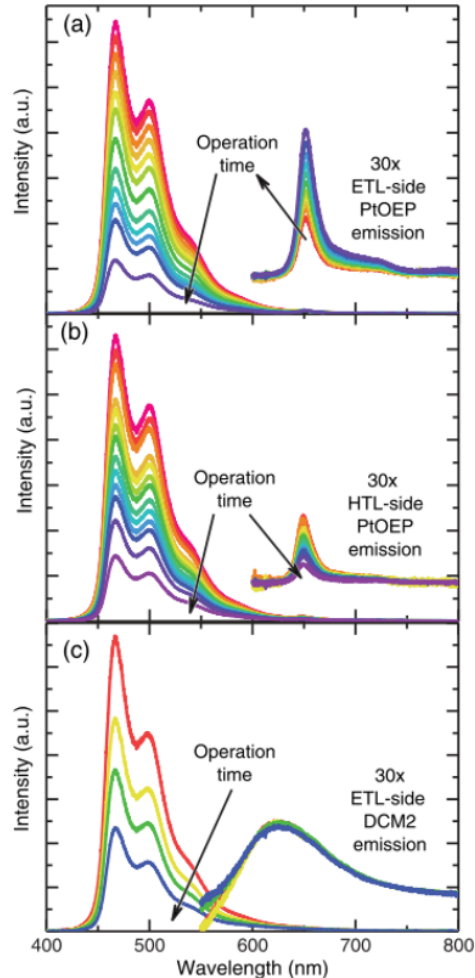


**Figure 2.20:** Device emission spectra containing a. PtOEP sensitizer on the ETL side of the device, b. PtOEP sensitizer on the HTL side of the device, DCM2 sensitizer on the ETL side of the device. Reproduced from Coburn and Forrest [70]

# Chapter 3

## Transient and Steady-State Dynamics

This section is an extension of my previous work entitled “*Unified analysis of transient and steady-state electrophosphorescence using exciton and polaron dynamics modeling*”.<sup>15</sup>

### 3.1 Motivation

As discussed in Chapter 2, modern OLEDs are typically based around Phosphorescent emitters in order to realize 100% internal efficiencies.<sup>7,9,30,134</sup> However, these phosphorescent emitters, while allowing emission out of the triplet excitonic state, also suffer from the drawback of a longer exciton lifetime, typically on the order of  $10^{-6}$ - $10^{-3}$  s.<sup>9,135</sup> An increased lifetime leads to a larger steady-state triplet exciton density compared to a fluorescent device operating at the same luminance. This becomes problematic at the high current densities associated with high brightness due to well documented quenching events.<sup>29,55,61,64,65,80,136</sup> These quenching events lead to a reduced quantum efficiency at high-current, and termed the “Efficiency roll-off”.

Efficiency roll-off is well attributed to quenching and is ubiquitous to phosphorescent OLED behavior.<sup>29,55,59,60</sup> While previous works have attributed the roll-off to quenching, they have failed to provide a complete picture of the exciton and charge dynamics within the device. All of these works have utilized a differential equations model for the exciton dynamics, solved in the steady state. This becomes apparent

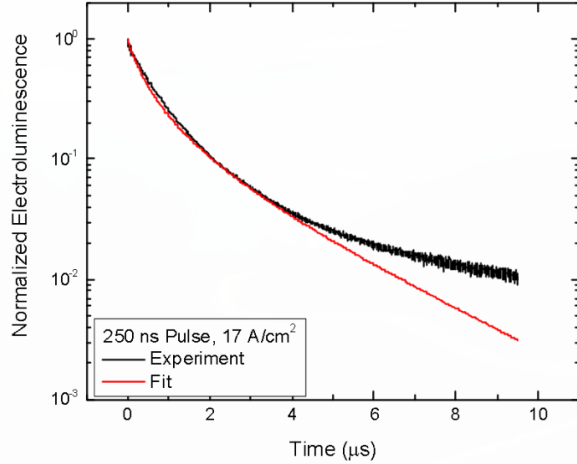


**Figure 3.1:** Fitting the transient electroluminescence decay without polaron dynamics.

when investigating the transient electroluminescence (EL), where a transient voltage pulse, on the order of 500 ns is applied to the device and the resulting luminance is recorded as a function of time. Figure 3.1 is an attempt to fit the transient luminance decay using the model presented by Reineke *et al.*<sup>29</sup> which well fits the efficiency roll-off. Indeed, this is a well known problem with existing models, and previous attempts to model the transient EL have utilized an empirical biexponential function to quantify the decay.<sup>55,60,66,137</sup> In addition to failing to replicate the luminance decay, no known previous efforts have been made in trying to replicate the experimental transient EL luminance rise.

In addition to the problems with the transient electroluminescence, the interpretation of the existing model without a full dynamics picture can lead to false predictions. Figure 3.2a shows what a quenching model predicts for the roll-off as a function of increasing recombination zone width.<sup>55</sup> However, even in the most idealized case of a gradient emissive layer device, where no additional interfaces come into play, the predictive model fails to replicate the behavior, as shown in Figure 3.2b. While this device is of little interest for further investigation due to the extreme thickness, the point stands that this model has glaring assumptions for it's applications.

Both the transient EL and the recombination zone dependence issues arise due to an incomplete picture of the device physics, more specifically in the area of polaron dynamics. This work sought to address these issues by including polaron dynamics. Since the steady-state solution of existing models is able to accurately replicate steady-state performance, the transient EL is utilized as well as the steady-state solution to ensure that the underlying physics are accurately captured. A valid solution should be able to accurately fit both regimes using the same model parameter values. In order to leverage previous work, the archetypical green-emitter tris[2-phenylpyridinato-*c<sub>2</sub>,N]Iridium(III) ( $\text{Ir}(\text{ppy})_3$ ) is used for the extensively characterized photophysics.<sup>7,66,138–141</sup>*

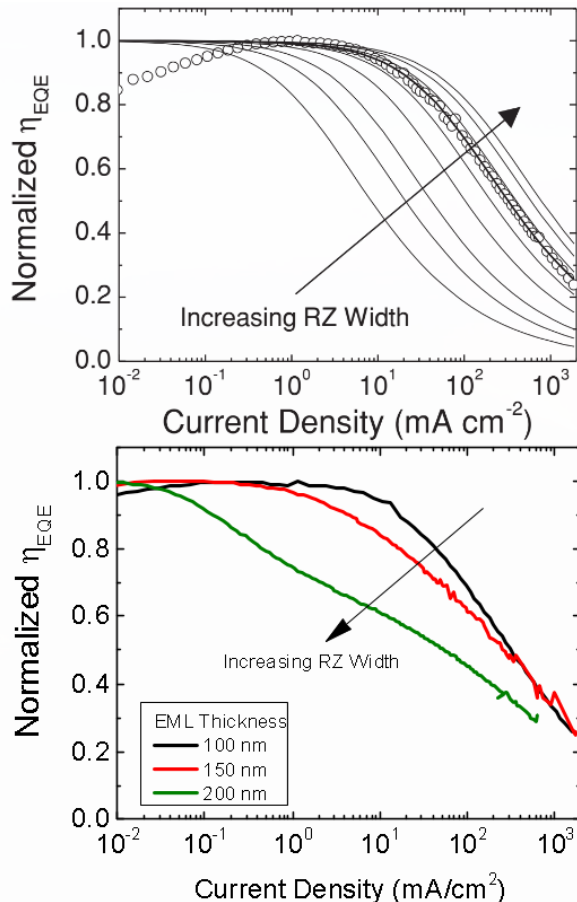


**Figure 3.2:** (a) Efficiency roll-off predicted by Erickson *et al.* 2014 as a function of recombination zone width.<sup>55</sup>  
(b) Observed efficiency roll-off for gradient EML devices.

## 3.2 Theory

### 3.2.1 Exciton Dynamics

The dominant processes that influence the exciton population, first formalized by Reineke *et al.*<sup>29</sup>, have been identified as natural exciton decay, via radiative and non-radiative processes, triplet-triplet annihilation, triplet-polaron quenching, and exciton generation.<sup>55,61</sup> In triplet-triplet annihilation, two triplets are able to interact, and one exciton transfers its energy to the other, resulting in one molecule relaxing to the ground state and the other forming a hot excited state. This hot state releases this additional energy to heat and typically relaxes back to the  $T_1$  state. Triplet-polaron quenching is the interaction of a polaron with a nearby triplet exciton. Here, one of the charges of the exciton non-radiatively recombines with the polaron of the opposite charge, leaving a remaining loose charge. Excitons are also subject to field dissociation, but this mechanism is ignored in this work. Field dissociation is typically observed for fields larger than  $2.5 \times 10^6$  V/cm. This is near the maximum field used for this study, and would be important to consider for higher voltage characterization.

In agreement with previous models, singlet-triplet exciton intersystem crossing and host-guest exciton energy transfer are assumed to be fast compared to exciton decay.<sup>8,29,66</sup> Since these mechanisms are much faster, they will not be rate-limiting processes and can thus be omitted from the differential equations model without sacrificing accuracy. Within an operational device, electron and hole populations are indistinguishable. Therefore, the electron ( $n_e$ ) and hole ( $n_h$ ) densities are treated as a single generalized polaron population,  $n_{pol} = n_e + n_h$ . For simplicity, the model developed here treats the exciton and polaron populations as spatially uniform and confined to the exciton recombination zone. An spatial inhomogeneity in exciton and polaron density as well as their overlap is absorbed into the bimolecular rate constants. It is important to note that due to this assumption, rate constants are a property of the device stack, and not just a material property. With these assumptions, the dynamic processes determining exciton density ( $n_{ex}$ ) can be summarized in the following one-dimensional rate equation:

$$\frac{dn_{ex}}{dt} = -\frac{n_{ex}}{\tau} - \frac{1}{2}k_{TT}n_{ex}^2 - k_{TP}n_{pol}n_{ex} + G_{ex} \quad (3.1)$$

where  $\tau$  is the natural exciton lifetime, determined by the radiative ( $k_r$ ) and non-radiative ( $k_{nr}$ ) decay rates by  $\tau = 1/(k_r + k_{nr})$ ,  $k_{TT}$  is the rate constant for triplet-triplet annihilation,  $k_{TP}$  is the rate constant for triplet-polaron quenching, and  $G_{ex}$  is the exciton generation rate. As this is a one-dimensional model,  $G_{ex}$  is a spatially uniform generation rate, a simplifying assumption. Many studies have modeled the exciton recombination zone profile, relying on material energy levels, as well as mobilities.<sup>142–146</sup> While these

models are more accurate and explicit, in the way that they capture the physics, they also increase the dimensionality of our model, as well as increasing the parameterization; requiring separate electron and hole rate equations, mobilities and energy levels for every material. Even with this increased accuracy of the physical processes, identifying if the predicted exciton recombination zone is accurate requires significant additional measurements. Since the goal of this work is to provide a functional model to accurately predict the transient and steady-state device behavior, spatially uniform dynamics are assumed. Here, exciton formation is treated using a Langevin recombination formalism based on the polaron density.<sup>145,147,148</sup>

$$G_{ex} = \frac{k_F}{4} n_{pol}^2 \quad (3.2)$$

where  $k_F$  is the rate constant for exciton formation. The factor of four accounts for the diversity of the polaron population and assumes that electrons and holes are in equal proportion. The accuracy of this pre-factor is reduced for imbalanced charge, and is investigated in Section 3.7.2. For  $n_e:n_h$  ratios 2:1 or better, less than 20% error is found in this term.

### 3.3 Polaron Dynamics

Previous models for efficiency roll-off have ignored polaron dynamics and assumed that all polarons readily form excitons. The steady-state polaron density is then modeled using a space charge limited model.<sup>12</sup> To attribute physics to this process, a simple picture of polaron dynamics is assumed, consisting of charge injection and transport, exciton formation, and polaron loss. In order to preserve our one-dimensionality, polarons must be uniformly distributed. Without competing losses in the transport layers, all injected polarons must eventually reach the emissive layer. We further assume that polarons easily enter that emissive layer and that the majority of polaron build up occurs within the emissive layer, rather than the transport layers. Therefore, the charges injected from the current density,  $J$ , are uniformly generated in the emissive layer by  $G_{pol} = 2J/ew$ . Here,  $e$  is the electron charge, and the factor of two arises from an assumption of equal charge injection. In a well balanced device, the measured current forms holes on one side of the device and electrons on the other, and are both injected into the device. This is discussed extensively in Section 3.7.1 Polaron losses to exciton formation mirror the exciton formation rate presented in Equation 3.2, though at twice the rate due to two polarons forming one exciton.

The introduction of polaron loss from the emissive layer through the device without forming excitons is essential to address the limitations of previous models. Without this term, peak internal quantum efficiency of all devices is assumed to be 100% and the roll-up of efficiency at low current can not be explained. In

order to capture polaron loss, a first order approximation is made for loss in that only the majority charge carrier can be lost and leaks through the device with a characteristic time,  $\tau_l$ . With these mechanisms, the full polaron dynamics can be expressed as:

$$\frac{dn_{pol}}{dt} = \frac{-k_F}{2} n_{pol}^2 - \frac{n_{pol}}{\tau_l} + G_{pol}. \quad (3.3)$$

### 3.3.1 Transient Electroluminescence

In this work, given a full model for polaron dynamics, the model is easiest to solve starting from the application of the current pulse, rather than at peak luminescence. Under pulsed electrical excitation, Equations 3.1 and 3.3 can be solved at the beginning of the pulse with the initial conditions  $n_{ex} = n_{pol} = 0$ . Upon the application of a voltage pulse, there is a time delay before polarons reach the emissive layer, as evidenced by the delay in luminance turn on. This has been previously attributed to charge injection and transport in the emissive layer.<sup>149</sup> The injection time varies with device area due to the device capacitance and accounts for the majority of the delay time for large devices. Transport is dependent on the mobility, as well as the field, which is a function of time due to the device capacitance. These times can be well predicted using the following equations:

$$t_{inj} = \tau \log \left( 1 - \frac{V_{th}}{V_0} \right) \quad (3.4)$$

$$d = \int_0^{t_{trans}} \mu_0 E_0 \exp \left( \sqrt{\gamma E_0 \left[ 1 - \left( 1 - \frac{V_{th}}{V_0} \right) e^{-t/\tau} \right]} \right) \left[ 1 - \left( 1 - \frac{V_{th}}{V_0} \right) e^{-t/\tau} \right] dt \quad (3.5)$$

where  $\tau$  is the RC time constant of the device,  $V_{th}$  is the voltage injection threshold,  $t_{inj}$  is the injection time,  $t_{trans}$  is the transport time,  $d$  is the transport layer thickness,  $\mu_0$  is the base mobility,  $\gamma$  is the field dependent mobility term,  $E_0$  is the field and  $V_0$  is the voltage. A prediction of the delay time as well as experimental values are shown in Figure 3.3. Interestingly, the functional dependence of the model accurately reproduces the extracted data. The mismatch in absolute value is due to the use of the geometric capacitance

in the model, and requires a scaling factor of 2.5 of the geometric capacitance for the calculated and fit delay times to agree. This factor is similar to that predicted by Liu et al. [150] for similar structures. This suggests that the effective charge distribution in our devices is about twice as wide as the emissive layer.

After this delay, constant current polaron generation is assumed for the remainder of the voltage pulse to calculate polaron generation. When the voltage pulse is removed,  $G_{pol}$  goes to 0 and the decay can be solved using Equations 3.1 and 3.3. This model does allow polarons to continue to form excitons after the voltage has been removed. In the transient regime, if the pulse width is shorter than  $\tau_l$ , polarons are not able to traverse the emissive layer during the voltage pulse. Once the voltage is removed, there is no longer a driving force for polaron leakage via drift. Under this assumption, the leakage term in Equation 3.3 can be ignored. After the full device behavior is fit, the validity of this assumption can be assessed based on the fit values for  $\tau_l$ .

### 3.3.2 Efficiency Analysis

The maximum external quantum efficiency of an OLED is often expressed as<sup>9,151</sup>

$$\eta_{EQE} = \eta_{OC} \eta_{PL} \chi \eta_{EF} \quad (3.6)$$

where  $\eta_{EQE}$  is the external quantum efficiency,  $\eta_{OC}$  is the out-coupling efficiency,  $\eta_{PL}$  is the photoluminescence efficiency of the emissive molecule,  $\chi$  is the fraction of excitons that are quantum mechanically allowed to emit (In the case of phosphorescent molecules,  $\chi = 1$  and  $\gamma$  is typically referred to as the charge balance. While frequently applied, this expression suffers from two major limitations: first, there is no accounting for losses due to exciton quenching, and second, charge balance losses are not strictly defined. Since this equation is intended for the maximum efficiency, further modification would have to be done to account for quenching, as is done in Chapter 4. The charge balance factor,  $\gamma$  is typically used as a correction factor to account for differences between the observed  $\eta_{EQE}$  and the other calculated factors in Equation 3.6. It is widely hinted at that charge balance relates to the carrier balance, but no formalism is ever given, so it cannot be calculated. Given our full dynamics model, we are able to be explicit in both of these areas in a meaningful way. The internal quantum efficiency of a device is simply the ratio of the radiative exciton rate to the rate of electron injection, and we can therefore recast Equation 3.6 as

$$\eta_{EQE} = \eta_{OC} \frac{n_{ex} k_r}{G_{pol}/2}. \quad (3.7)$$

Note that in this equation, exciton quenching is accounted for in the  $n_{ex}$  term because in the steady-

state,  $n_{ex}$  is reduced according to this quenching, which is competitive with  $k_r$ . Dynamically, the charge balance factor is the fraction of injected polarons contributing in exciton formation. This can be viewed as the efficiency of Equation 3.3 to form excitons. Given this interpretation, we will recast the charge balance factor  $\gamma$ , as an explicitly defined exciton formation efficiency  $\eta_{EF}$  as

$$\eta_{EF} = \gamma = \frac{\frac{1}{2}k_F n_{pol}}{G_{pol}} = \frac{\frac{1}{2}k_F n_{pol}}{\frac{1}{2}k_F n_{pol} + \frac{1}{\tau_l}} \quad (3.8)$$

Equations 3.7 and 3.2 allow us to rigorously tie  $\eta_{EQE}$  and  $\eta_{EF}$  to dynamic processes within the device in a quantitative manner.

### 3.4 Experimental Details

Devices used for measurements of transient and steady-state EL had the following structure: ITO (150 nm)/poly(3,4-ethylenedioxythiophene)-poly(styrene sulfonate) (PEDOT-PSS) (40 nm)/tris(4-carbazoyl-9-ylphenyl)amine (TCTA) (30 nm)/10% tris[2-phenylpyridinato-C2,N]Iridium(III) ( $\text{Ir}(\text{ppy})_3$ ) doped in 4,40-Bis(N-carbazoyl)-1,10-biphenyl (CBP) (10 nm)/bathophenanthroline (Bphen) (30 nm)/LiF (1 nm)/Al (100 nm). Transient PL decays were measured using 60-nm-thick films of CBP doped with 10%  $\text{Ir}(\text{ppy})_3$  deposited on quartz slides. The hole-only device structure used for steady-state PL quenching measurements had the following structure: ITO (150 nm)/PEDOT-PSS (40 nm)/10%  $\text{Ir}(\text{ppy})_3$  in CBP (60 nm)/Au (50 nm). The gold cathode was used to prevent electron injection. Transient EL measurements were conducted using a voltage pulse generator (HP 8114a) with pulse amplitudes ranging from 5–40V and pulse widths ranging from 250 ns–500 ns with a period 500 ls. Luminescence was recorded using a set of collection lenses focused onto a fast photodiode (Thorlabs DET36A). Pulsed  $\eta_{EQE}$  measurements were conducted using the HP 8114a pulse generator until the device reached steady state current and luminance, which were recorded. Overlapping points with the steady state  $\eta_{EQE}$  measurement were used to calibrate the luminance-current ratio to the  $\eta_{EQE}$ . The photodiode signal was recorded using an oscilloscope (Tektronix TDS5104b). Transient PL measurements were collected using a pulsed nitrogen laser (Optical Building Blocks) with a pulse length of approximately 1 ns and emission wavelength of  $\lambda = 337$  nm at a repetition rate of 6 Hz. Laser light was focused on the sample using a series of lenses, with collection carried out using the same techniques already described for transient EL. Incident laser power was measured using a Coherent EnergyMax 10MB-HE detector. Film thicknesses and optical constants used for modeling the out-coupling efficiency in Equation 3.7 were obtained using a J. A. Woollam variable angle spectroscopic ellipsometer (VASE) using a Cauchy dispersion model.

### 3.5 Exciton Quenching in Photoluminescence

Photoluminescence measurements have been previously used to extract the rate constants for triplet-triplet annihilation and triplet-polaron quenching.<sup>29,55</sup> This is important because it allows an independent confirmation of the extracted rate constants extracted during the electroluminescence fitting. The transient photoluminescence exposes the natural exciton lifetime,  $\tau$  and at high incident flux, the triplet-triplet annihilation rate constant,  $k_{TT}$ . This measurement involves an incident laser pulse, in this case, from a 337 nm nitrogen laser, which is able to excite a large exciton population. The pulse width of the nitrogen laser is 1ns and is much faster than  $\tau$  or  $k_{TT}$ , allowing us to use Equation 3.1 with the initial boundary condition  $n_{ex} = A(E_{pulse}/hfV)$  where  $A$  is the absorbed fraction of photons,  $E_{pulse}$  is the pulse energy,  $hf$  is the photon energy and  $V$  is the film volume. Since this is optical only excitation, the other boundary condition is  $n_{pol} = 0$  and we can ignore Equation 3.3.<sup>29,55,66</sup> For CBP films doped with Ir(ppy)<sub>3</sub>, good agreement with the model is observed across a range on initial exciton densities, as shown in Figure 3.4(a). The exciton lifetime,  $\tau$  was found to be mostly independent of exciton density and was globally fit to  $1.5 \pm 0.2 \mu s$ . The triplet-triplet annihilation rate constant appears to be a function of intensity and ranges from  $k_{TT} = 2.4 \times 10^{-13} \text{ cm}^3/\text{s}$  at  $n_{ex_0} = 4.1 \times 10^{18} \text{ cm}^{-3}$  to  $k_{TT} = 6.9 \times 10^{-14} \text{ cm}^3/\text{s}$  at  $n_{ex_0} = 1.1 \times 10^{20} \text{ cm}^{-3}$ . These extracted values and trend with intensity are in good agreement with previous reports.<sup>29,55,152</sup> It is important to note, that the exciton environment is very important for these values. Previous studies have shown that the presence of a metal cathode on top of the film can significantly reduce the exciton lifetime by allowing additional non-radiative recombination via surface plasmon coupling.<sup>56</sup> This becomes important in the comparison of these parameters with those obtained under electroluminescence

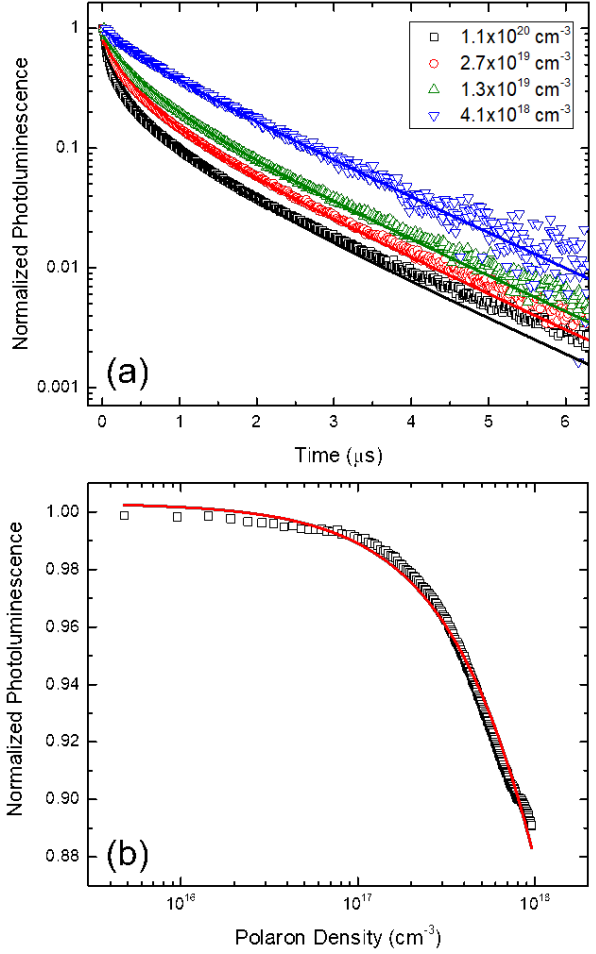


**Figure 3.4:** (a) Transient photoluminescence (PL) decays for several initial exciton densities with fits shown as solid lines using Equation 3.2. Fit parameters are discussed in SECTION. Exciton densities are calculated using measured incident power and beam size in combination with Beer's Law. (b) Steady-state PL quenching as a function of polaron density and the resulting fit from Equation 3.11 shown as the solid line.

within a device. A more representative experiment would have involved a full device stack with cathode, rather than just a film. Alas, I did not have that foresight for this experiment.

Triplet-polaron quenching rate constant measurement is done in single carrier devices as a function of polaron density. It is largely uninvestigated as to the differences between electrons and holes, but in previous works, hole only currents are used, a precedent which will be followed in this work.<sup>29,55</sup> A steady-state exciton population is generated optically, in this case, a 405 nm laser. In a single carrier device, a space charge limited current model featuring an exponential trap distribution is often used.<sup>12,14,84</sup> This model is employed largely because it fits the obtained current-voltage behavior most closely. In reality, a single trap state would be expected, as that is what is introduced by Ir(ppy)<sub>3</sub> in a doped film. These models are frequently employed, despite their inaccuracies, largely for simplicity. A more accurate determination of polaron density is discussed in Chapter C. However, in a space charge limited model with an exponential trap distribution, the current density voltage relationship can be modeled using

$$V = \left[ \frac{J}{e\mu N_C} d^{2l+} \left( \frac{eN_0 k_B T_t}{\epsilon} \right)^l \right]^{\frac{1}{l+1}} = CJ^{\frac{1}{l+1}}, \quad (3.9)$$

where  $N_C$  is the density of states at the transport level,  $\epsilon$  is the permittivity,  $\mu$  is the mobility,  $L$  is the device thickness and  $l = T_t/T$  with  $T_t$  being an experimentally determined characteristic temperature of the trap distribution. The Polaron density is then given by

$$n_{pol} = eN_c \left( \frac{\epsilon V}{ed^2 N_0 k T_t} \right)^l. \quad (3.10)$$

Combining Equation 3.10 with Equation 3.1, the ratio of the steady-state PL intensity ( $L$ ) to the PL intensity in the absence of polarons ( $L_0$ ) can be written as<sup>29</sup>

$$\frac{L(n_{pol})}{L_0} = \frac{1}{1 + \tau k_{TP} n_{pol}} \quad (3.11)$$

After fitting the current density-voltage characteristics of the device are fit using Equation 3.9, Equations 3.10 and 3.11 can be used to extract the triplet-polaron rate constant for a given value of  $\tau$ . In this case, we use  $\tau$  as extracted from the transient PL measurements. The fit obtained for a CBP Ir(ppy)<sub>3</sub> hole only device is shown in Figure 3.4b. This device utilizes a gold cathode to prevent electron injection and shows minimal exciton formation, as expected. The organic stack is the same as the emissive layer of the investigated device. In fitting the current density-voltage characteristics using Equation 3.9, a value of  $l = (2.4 \pm 0.2)$  was found. The extracted triplet-polaron quenching rate constant from fitting Equation 3.11 was  $k_{TP} = (2.8 \pm 0.2) \times 10^{-13}$  cm<sup>3</sup>/s and is agreement with previous measurements.<sup>29,55</sup>

## 3.6 Application to Devices

In order to fit both the steady-state and transient regimes, decisions need to be made as to a methodology for extracting parameters. The obvious choice may seem to be to try to produce a global fit by fitting both regimes simultaneously. The major draw back of this approach is the value of  $\tau_l$ . Since this is a function of the applied field, this is not single valued and relies on knowing the field dependence. Additionally, the steady-state provides little insight into the actual quantities of  $\tau$ ,  $k_{TT}$ ,  $k_{TP}$ , and  $k_F$ , and only the ratio of radiative and non-radiative processes is needed for a quality fit of the efficiency roll-off. Additionally, within this model, only  $n_{ex}$  is experimentally available to fit, and the fit parameters are not independent. The most obvious example of this is the values of  $k_{TT}$  and  $k_{TP}$ , which have similar impact on the exciton population and similar formulation. This makes it near impossible to distinguish a dominant mechanism between these two, and results for exact values of quenching constants need to be considered with caution. This methodology only gives a net effect of the two quenching mechanisms in total, rather than a true separate measurement of both quantities as is obtained in the PL quenching measurements, discussed in Section 3.5.

With these limitations addressed, the method used for this discussion to fit all of the device physics has been carefully considered to achieve the highest parameter sensitivity. The bimolecular quenching constants are most sensitive to the efficiency roll-off since small changes in the quenching constants make a large impact on the roll-off behavior. However, the lifetime and exciton formation can only be determined to within a fixed ratio. In contrast, the exact values of lifetime and exciton formation rate are critical to the behavior of the transient EL while the bimolecular quenching constants are difficult to probe in the current regime investigated. In order to use these sensitivities, a quenching only model (ignoring  $\tau_l$ ) to fit the normalized efficiency roll-off, such has been previously reported, is used to determine the bimolecular quenching rates,  $k_{TT}$  and  $k_{TP}$ . Quenching only models can only fit the normalized  $\eta_{EQE}$  roll-off because without a polaron loss term,  $\eta_{EF}$  is assumed to be 100% and the exact magnitude of efficiency cannot be reproduced. Initial values for all parameters, except  $k_F$  which is previously unmeasured, are determined by the photoluminescence measurement values. With these quenching rates fixed, the transient EL is fit using Equations 3.1 and 3.3 in order to determine  $\tau$  and  $k_F$ . Remember that in the transient regime for short pulses, we can assume that  $\tau_l = \infty$  and can be ignored.

With these critical rate constants determined, we will revisit the efficiency as a function of current density. In the first pass, we ignored the exact value of efficiency and only fit the normalized roll-off. Now, since we know the other parameters, we can revisit  $\eta_{EQE}$ , now matching the exact profile for all currents, by conducting a point-by-point fit for  $k_F$ . This fit for  $k_F$  can then be used to calculate  $\eta_{EF}$  and can be compared to a drift model, to assess its validity.

### 3.6.1 Quenching Only Steady-State Fit

To measure transient and steady-state EL, devices were constructed using the architecture discussed in Section 3.4. These devices had an  $\eta_{\text{EQE}}$  of  $(9.7 \pm 0.1)\%$ . Equations 3.1 and 3.3 were used to fit the peak normalized steady-state efficiency roll-off with  $\tau_l = \infty$ . Again, omitting a polaron loss term, this model assumes that all roll-off behavior comes from quenching. Parameters were initialized using the values obtained from PL quenching measurements, described in Section 3.5. An experimental fit is shown in Figure 3.5 and shows good agreement, except at very high currents associated with pulsed  $\eta_{\text{EQE}}$  measurements. Parameters are summarized in Table 3.1 and are in good agreement with those previously reported.<sup>29,66</sup>

	Transient EL	Efficiency Roll-off
$\tau$ (s)	$6.9 \pm 0.1 \times 10^{-7}$	$6.1 \times 10^{-7}$
$k_{\text{TT}}$ (cm <sup>3</sup> /s)	$7.1 \times 10^{-12}$	$7.1 \times 10^{-12}$
$k_{\text{TP}}$ (cm <sup>3</sup> /s)	$3.3 \times 10^{-13}$	$3.3 \times 10^{-13}$
$k_F$ (cm <sup>3</sup> /s)	$7.7 \pm 3.5 \times 10^{-12}$	$1.6 \times 10^{-11}$

**Table 3.1:** Fit parameters extracted from transient and steady-state electroluminescence. Transient EL fit parameters averaged over all measured current densities.  $\eta_{\text{EQE}}$  roll-off parameters averaged over several measured devices. Triplet-triplet annihilation and triplet-polaron quenching rates are fixed to those obtained from fitting the normalized efficiency roll-off.

### 3.6.2 Transient Modeling

Transient EL measurements were conducted on the same devices used for the efficiency measurements described in Section 3.6.1. Pulse widths ranging between 250–500 ns with a period of 500 ls were used with current densities ranging between 0.5–50 A/cm<sup>2</sup>. Fast Fourier Transform (FFT) filtering is used to remove experimental noise from the measured signal to increase fit accuracy. The bimolecular quenching rate constants are fixed to the values determined from the fitting of the steady-state efficiency roll-off (Table 3.1). The exciton lifetime and exciton formation rate constant are allowed to vary to fit the transient EL and are summarized in Table 3.1. The value of  $\tau$  is shorter than that obtained under transient PL, likely due to the cathode present for EL transient studies.<sup>56</sup> Fits using this model are shown in Figure 3.6 and show excellent

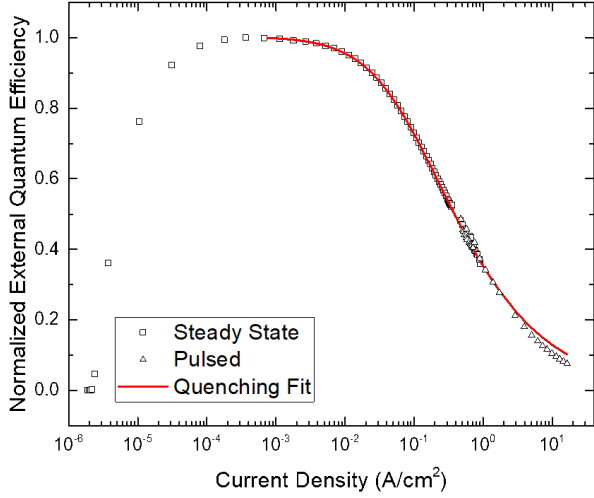


**Figure 3.5:** Normalized experimental  $\eta_{\text{EQE}}$  as a function of current density. Solid line is a fit to the data using Equation 3.1 and 3.3 in the absence of polaron loss. Pulsed EQE measurements are conducted using low duty cycle pulses to steady-state luminance to reduce Joule heating in device.

agreement above the detection limit. The initial turn on is well replicated by the luminance delay model discussed in Section 3.3.1

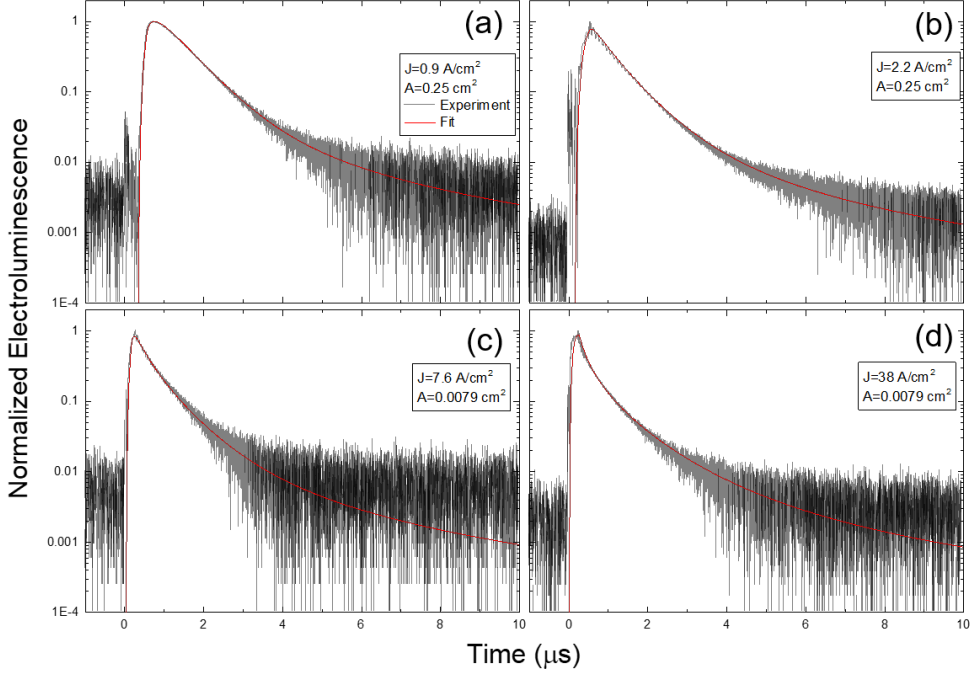


**Figure 3.6:** Transient electroluminescence (EL) for four different current densities ( $J$ ) and device areas ( $A$ ). (a)  $0.25 \text{ cm}^2$  device at a current density during the pulse of  $J = 0.9 \text{ A}/\text{cm}^2$  (b)  $0.25 \text{ cm}^2$  device at  $J = 2.2 \text{ A}/\text{cm}^2$  (c)  $0.0079 \text{ cm}^2$  device at  $J = 7.6 \text{ A}/\text{cm}^2$  (d)  $0.0079 \text{ cm}^2$  device at  $J = 38 \text{ A}/\text{cm}^2$

### 3.6.3 Transient Term Efficiency

Utilizing the understanding of dynamics developed here, the efficiency of each component in Equation 3.1 for the transient EL can be analyzed. This is shown for representative high and low current density behavior in Figure 3.7. At the application of the voltage pulse, exciton generation is the dominating feature, resulting in a steep rise in luminescence. As the exciton and polaron populations peak, the resulting dependence is seen on the bimolecular quenching terms, leading to the curvature seen before and after the removal of the injected current. During the decay, the exciton and polaron populations rapidly decrease due to quenching, resulting in the natural exciton lifetime becoming the dominant behavior. As the exciton population further diminishes, formation of excitons from the residual polaron population is observed, resulting in the slow decay seen at long times. Figure 3.7a shows the decoupled EL transient behavior at a low current density where exciton formation and the natural lifetime are always competitive processes, resulting in the slow rollover in the experimental behavior of Figure 3.6a. Slightly higher current densities do not show the bimolecular terms rise to prominence, resulting in the linear decay after the pulse seen in Figure 3.6b. Bimolecular quenching terms show increasing importance with current density, especially at times soon after the removal of voltage.

We see this behavior in Figures 3.6c and 3.6d with the decoupled high current density behavior of Figure 3.6d demonstrated in Figure 3.7. Here, we are able to see that bimolecular quenching events dominate when the exciton density is peaked after the removal of voltage.

### 3.6.4 Extracting Exciton Formation Efficiency

Thus far in the fitting, the introduced model has successfully fit the transient EL and steady-state efficiency roll-off using Equations 3.1, 3.2, and 3.3 by including polaron dynamics in the absence of charge leakage. However, only the efficiency roll-off and the normalized reduction in magnitude have been modeled. By including the polaron transit time in the analysis, the exact magnitude can be fit for both the rise and fall of efficiency. Starting with the experimental  $\eta_{\text{EQE}}$  as a function of current density, Equation 3.7 can be used to find the exciton density,  $n_{\text{ex}}$ , as a function of current density, which in turn allows Equations 3.1 and 3.3 to be solved in the steady-state for  $\tau_l$ . The out-coupling efficiency,  $\eta_{\text{OC}}$ , is separately determined using optical modeling and found to be  $\eta_{\text{OC}} = 17.7\%$ .<sup>10,11</sup> The details of this calculation are discussed in Chapter 8. The radiative rate in Equation 3.7 can be extracted from measurements of  $\tau$  and  $\eta_{\text{PL}}$  as  $\eta_{\text{PL}} = \tau k_r$ . Once the exciton population is known, Equation 3.1 can be solved for the polaron population,  $n_{\text{pol}}$  using the fit values from the transient EL. With  $n_{\text{pol}}$  and  $G_{\text{pol}}$

known, Equation 3.3 can be used to extract the  $\tau_l$  needed to reproduce the experimental  $\eta_{\text{EQE}}$ . This technique produces an exact match of the shape and magnitude of the efficiency, including both the roll-up and roll-off. This is the first time in literature that a quantitative physical explanation has been attributed to the roll-up. Any error in this method are absorbed into  $\tau_l$ . Extracted values of  $\tau_l$  are shown in Figure 3.8. In order to justify these values, a simple drift model explanation can be used, quantified by

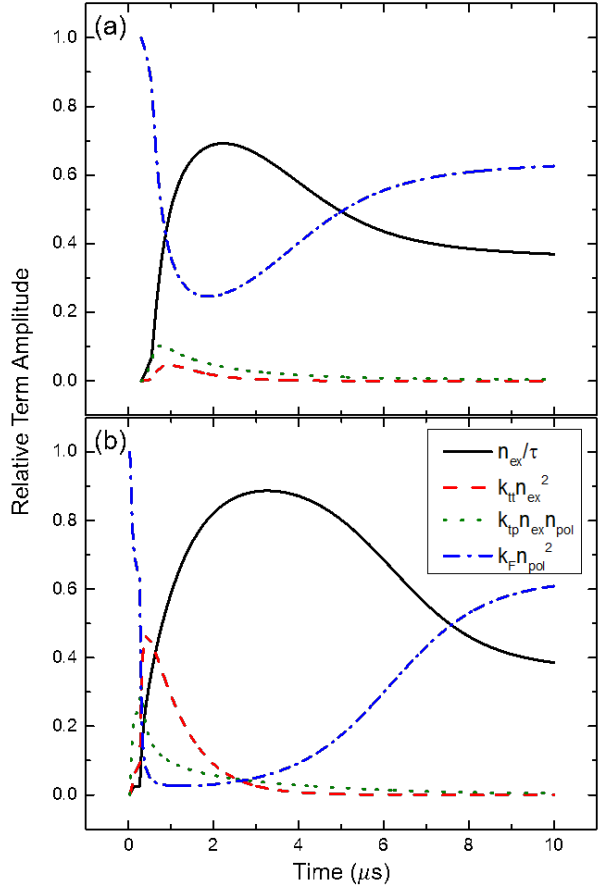


**Figure 3.7:** Term efficiency for each dynamical process influencing the exciton population for (a)  $0.25 \text{ cm}^2$  device operated at  $0.9 \text{ A/cm}^2$  for 500 ns and (b)  $0.785 \text{ mm}^2$  device operated at a current density of  $38 \text{ A/cm}^2$  for 250 ns. Relative term amplitude is calculated as the magnitude of each term in Equation 3.1 divided by the sum of absolute values of each term.

$$\tau_l = \frac{w}{E\mu(E)}. \quad (3.12)$$

Where  $\mu$  is the mobility, obtained from Parshin et al. [153],  $w$  is the device width, and  $E$  is the electric field. This simple explanation for  $\tau_l$  holds very well at low current density, corresponding to the efficiency roll-up, as well as the peak efficiency. Deviation from this model occurs as current density increases past  $10^{-1}$  A/cm<sup>2</sup>. However, in this regime, exciton and charge densities are becoming increasingly high, and the predicted values become increasingly non-physical. It is expected that in this regime, this simple model described in Equation 3.12, would break down.

### 3.6.5 Drift Model

With the transit time known, Equation 3.8 can be used to find  $\eta_{EF}$ , shown in Figure 3.8. Charge balance remains relatively constant throughout the onset of roll-off and only falls when the efficiency approaches one quarter of its initial value. Using a different modeling approach, Giebink and Forrest [60] find that for a similar system, a larger portion of the roll-off is due to a loss of charge balance, likely due to a thicker emissive layer and differing transport layers than those used in this study. With the dependence of the charge balance factor on current density established, the validity of the assumption of uniform charge balance during the fit of the normalized efficiency roll-off in Section 3.6.1 can now

be assessed. The charge balance, seen in Figure 3.8, remains almost constant for the majority of the roll-off but deviates at high current density, suggesting that the high current density regime should not be fit with the quenching only model. However, the fit shown in Figure 3.5 is not limited by this restriction as there is excellent agreement between the model and experiment in the regime of near constant charge balance, with the only discrepancy in the fit coming at high current density where the model assumptions break down. Returning to fit the normalized efficiency in the regime of near constant charge balance, as defined by Figure 3.8, while holding  $\tau$  and  $k_F$  constant,  $k_{TT}$  and  $k_{TP}$  are found to be  $(4.5 \pm 0.4) \times 10^{-12}$  cm<sup>3</sup>/s and  $(2 \pm 3) \times 10^{-12}$  cm<sup>3</sup>/s, respectively. This small variation of quenching parameters does not change the fit quality for the

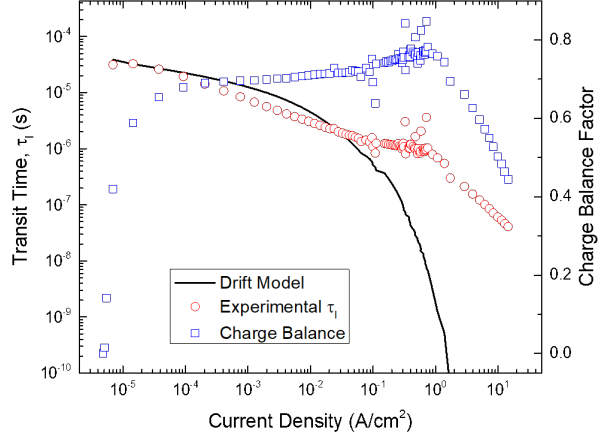


**Figure 3.8:** Transit time extracted from  $\eta_{EQE}$  measurements are shown as the red circles. Predictions using the drift model are calculated using Equation 3.12. The drift model assumes a uniform electric field. Good agreement between the experimental transit time and the drift model is found for a field distributed over 20 nm. The charge balance factor is shown as a function of current density in blue squares.

regime in question. Repeating the fitting process in this regime yields no significant differences in  $\tau$  and  $k_F$  or the dependence of charge balance on current density.

### 3.7 Understanding Assumptions of Polaron Model

In the model described in this work, electrons and holes are summarized into a generalized polaron population with the dynamics described using Equation 3.3. To understand the impacts that this has on calculating the polaron injection rate and the exciton formation rate, the electrons and holes must be independently examined. The most complete dynamics picture related to the developed model would express individual electron and hole injection as well as individual transit times. This full picture can be written as:

$$\frac{dn_h}{dt} = -k_F n_e n_h - \frac{n_h}{\tau_{lh}} + \frac{J_h}{ew} \quad (3.13)$$

$$\frac{dn_e}{dt} = -k_F n_e n_h - \frac{n_e}{\tau_{le}} + \frac{J_e}{ew} \quad (3.14)$$

where  $n_e$  and  $n_h$  are the electron and hole population densities,  $n_e$  and  $n_h$  are the electron and hole transit times, respectively,  $J_h$  and  $J_e$  and are the single carrier injected currents. While more accurate, Equation 3.13 and 3.14 pose several problems for replicating device behavior due to the inability to distinguish between carriers during device operation. This is further complicated by the inability to separately measure the single carrier injected currents and leak rates due to transit times. To better understand the approximations used in Equation 3.3, a detailed analysis of current injection is presented, followed by error analysis of the exciton formation term based on the composition of the polaron population.

#### 3.7.1 Carrier Injection

Let  $J$  be the total current within our device. This must be maintained throughout our circuit assuming no charge buildup. Within the device, the total current can be written as  $J = J_e + J_h$ . Experimentally,  $J$  is the only measurable current as we are not able to distinguish between electron and hole or leaked currents. The current incident on either contact will be referred to as  $J_1$  and  $J_2$ . These currents are summarized in Figure 3.9. In the case of no leakage current, there must be complete recombination in the emissive layer. Therefore all of the externally measured current from one side of the device contributes only to electron current and all current on the other side contributes only to hole current.

$$J_1 \rightarrow J_h = J_2 \rightarrow J_e \quad (3.15)$$

This maintains constant current throughout the external circuit. No charges are allowed to leave the emissive layer without recombining with the opposite charge species and constant current maintains that  $J_e = J_h$ . The injected polaron density is then:

$$\frac{J_e}{ew} + \frac{J_h}{ew} = \frac{J_1 + J_2}{ew} = \frac{2J}{ew} \quad (3.16)$$

This expression becomes more complicated when charge leakage is allowed. Let us assume that holes are the only leaking species. Let  $J_l$  be the current leaking through the emissive layer. On the hole side of the device, all current is hole current. However, on the electron side of the device, the measured current is a combination of the electrons injected and the leaked holes.

$$J_1 = J_h \quad (3.17)$$

$$J_2 = J_e + J_l \quad (3.18)$$

For current continuity, the current on either side of the device must be equal.

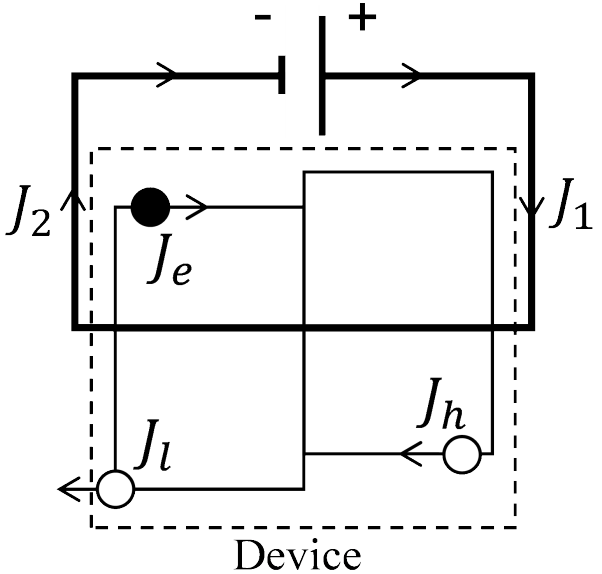


**Figure 3.9:** Current density formalism within the circuit.  $J_1$  and  $J_2$  are the currents measured on either side of the device.  $J_e$  and  $J_h$  are the electron and hole currents within the device and  $J_l$  is the unbalanced current, assumed to be only holes, that leaks out of the opposing contact.

$$J = J_h = J_e + J_l \quad (3.19)$$

From this expression and the experimentally measured current, it is not possible to know the electron and hole currents independently without making some assumption about the leaked current. If both carriers are allowed to leak, there is a leakage term on the hole current side of Equation 3.18 as well. Without additional information about the proportion or magnitude of the leaked current, there is no exact expression for polaron injection in terms of  $J$ . Therefore, the approximation is used that the polaron injection and loss due to leakage can be written as:

$$G_{pol} - \frac{J_l}{ew} = \frac{2J - J_l}{ew} \quad (3.20)$$

This is the expression used in the final model, assuming the charge leakage can be written in terms of the

total population and a transit time for leakage as  $J_l/ew = n_{pol}/\tau_l$  and  $G_{pol} = 2J/ew$ . The approximation in Equation 3.19 is strong assuming is small relative to  $J_h$  and  $J_e$ .

### 3.7.2 Charge Imbalance

In the exciton formation term of Equation 3.3, the factor of two in the denominator assumes that charges are in equal proportion. More generally, Equations 3.14 and 3.13 can be used to evaluate the error in this term as the charge balance increases. Let the carrier ratio be defined as:

$$\alpha = \frac{n_h}{n_e + n_h} \quad (3.21)$$

This is different from the charge balance we have defined in the text as this is an actual ratio of carriers, rather than the exciton formation efficiency. Additionally, let  $n + pol = n_e + n_h$  be the polaron population density. With these definitions, the terms for polaron loss to exciton formation of Equations 3.14 and 3.13 can be summed as:

$$\left[ \frac{dn_{pol}}{dt} \right]_{formation} = -2k_F n_{pol}^2 \alpha(1 - \alpha) \quad (3.22)$$

In the case of perfect balance, the expression  $\alpha(1 - \alpha) = 1/4$  and agrees with Equation 3.3. The variation in  $\alpha(1 - \alpha)$  as a function of  $\alpha$  can be seen in Figure 3.10. With charge ratios up to 1:3, there is less than a 20% error in this expression. The high efficiency devices examined in this work are expected to operate in this regime, and the value of  $\alpha(1 - \alpha)$  should not change the value of  $k_F$  significantly.

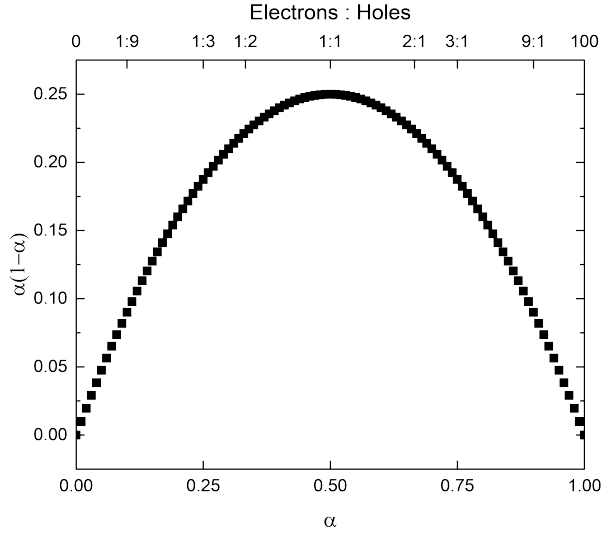


**Figure 3.10:** The quantity  $\alpha(1 - \alpha)$  is plotted as a function of the polaron composition,  $\alpha$  and the electron to hole ratio.

## 3.8 Conclusion

A universal dynamics model has been successfully implemented that allows the fitting of the transient and steady-state EL behavior of OLEDs using Ir(ppy)<sub>3</sub> as an emitter. This model relies upon the previously studied parameters  $\tau$ ,  $k_{TT}$ , and  $k_{TP}$  as well as introducing polaron dynamics in the form of an exciton formation rate,  $k_F$  and polaron leakage time  $\tau_l$ . This model has been used to deconstruct all features of the transient EL over three decades of decay. The fit parameters  $\tau$ ,  $k_{TT}$ , and  $k_{TP}$  have all been verified

independently using PL studies in agreement with the proposed model. The steady-state efficiency has been fully characterized using quenching and charge leakage through the device. The behavior of the investigated devices suggests that charge leakage through the emissive layer dominates the roll-up in efficiency, while bimolecular quenching is responsible for the majority of the roll-off in efficiency.

This model has successfully been able to model all of the device physics present in the electroluminescence behavior. However, one of the initial goals of this project was to be able to quantify the bimolecular rate constants more effectively within a device. In this regard, the model is not useful as  $k_{TT}$  and  $k_{TP}$  are codependent and their relative values are still unknown.

## Chapter 4

# Integrated Photoluminescence Lifetimes

As OLEDs become fully a fully commercialized technology, several challenges still exist that need to be overcome to realize full potential. Chief among these is the operational lifetime, which has been a key focus of recent studies.<sup>6,94,125–127</sup> Lifetime is typically characterized at constant current density, recording the luminance loss and voltage as a function of time. The lifetime is then reported as the time to reach some arbitrary fraction of the initial luminance. Unlike the steady-state efficiency, it is difficult to optimize a device lifetime by brute force. Due to the long lifetime of devices, even under accelerated aging, it takes a substantial amount of time to characterize devices and iteratively improve a design. This reality makes it essential to have a deeper insight into the processes that are limiting lifetime.

While this simple lifetime characterization is effective for device to device comparison, further insight into the mechanism is found wanting. Modeling techniques are used extensively for degradation characterization, using the mechanisms outlined in Chapter 2.8.1.<sup>69,70,154</sup> While these techniques are able to reproduce the decay characteristics with a root in physical mechanisms, they suffer from over-parameterization and introduce parameters that cannot be experimentally confirmed. As discussed in Chapter 2.8.3, a variety of chemical, structural, and spectroscopic techniques are often employed to gain further insight into the physical processes.<sup>6,103,125,126,155</sup> These techniques can be insightful, but are difficult to apply on a large scale due to the additional processing time. Post degradation analysis does not provide a temporal characterization of degradation without processing individual devices at several decay points, which can be extremely time consuming. Additionally, it may be helpful to categorize luminance loss into different luminance loss pathways, which few of these techniques are able to do. It would be beneficial to have a technique that is able to provide more information during the degradation, without increasing experimental time, as well as provide a way to decouple loss pathways. This is done by introducing an optical pump to independently measure

$\eta_{PL}$  as a function of time. Similar techniques have been utilized before, but have lacked completeness in their care to treat assumptions, as well as their resolution.<sup>122,156,157</sup>

This chapter demonstrates a method for decoupling the device photoluminescence loss from the exciton formation losses during operational lifetime testing. This is a summary and extension of my work entitled Hershey et al. [85] as well as some error analysis from Bangsund and Hershey [158].

## 4.1 Luminance as Efficiency Loss

When OLEDs are degraded at constant current density, luminance loss is observed. As discussed in Chapter 2.3.2, quantum efficiency is the ratio of photons leaving the device per electron input. Therefore, at constant current density (or constant electron flux), luminance loss is actually an efficiency loss. Chapter 3 extensively discussed a revised formalism for understanding OLED efficiency. In particular, we will take advantage of the formalism of exciton formation efficiency. For decoupling luminance loss pathways, a categorical expression for  $\eta_{EQE}$  is desired, rather than the dynamics approach taken in Equation 3.7, therefore Equation 3.6 is modified to include a quenching term, yielding

$$\eta_{EQE} = \eta_{PL} \eta_{OC} \chi \eta_{EF} \eta_\tau \quad (4.1)$$

where  $\eta_\tau$  is the fraction of excitons that relax via the natural exciton lifetime,  $\tau$ . this term is current-density dependent and captures the quenching events discussed in Chapter 3. It is also important to note that during degradation,  $\eta_{EF}$  captures not only the previously discussed polaron loss due to leakage events, but also the formation of non-radiative recombination centers (NRRCs). NRRCs are states that form excitons off of the emissive molecule and allow charge recombination without forming light, which have been shown to be present in degrading devices.<sup>118,122</sup> The interpretation of  $\eta_{EF}$  as the exciton formation efficiency needs to be clarified to be the efficiency of exciton formation on the emissive molecule, but remains otherwise unchanged.

During degradation, to categorize efficiency loss, each term in Equation 4.1 could be considered to be time dependent. However, it is reasonable to assume that some of these terms are unchanged, or have minimal impact. The exciton's radiative spin fraction,  $\chi$  is a quantum mechanical property of the emissive molecule. Therefore, without changes in the emissive molecule, this term should remain constant. If emission from another state was observed spectrally, this would indicate a need to adapt Equation 4.1 for multiple emissive states, greatly complicating this process. Thankfully, that is of yet unobserved in our research.

The out-coupling efficiency,  $\eta_{OC}$ , is a property dependent on the layer optical constants and thicknesses. Without significant changes in molecular composition and morphology, it is unlikely that  $\eta_{OC}$  should change. The most likely way to create these changes would be through crystallization. This can be investigated by looking at the devices under crossed polarized optical microscopy.<sup>5</sup> Figure 4.1 shows that in our devices, no crystallization is observed. The reference photo, taken from Fielitz *et al.*<sup>5</sup> demonstrates how apparent crystallization would be if present. It is also important to note that  $\eta_{OC}$  depends on the emitter distribution within the device, and thus the recombination zone. If there is a shift in RZ, out-coupling is likely to change. It is difficult to assess recombination zone and unprecedented to measure as a function of degradation.

However, this problem is minimized in thin emissive layers, so studies should attempt to focus on thinner EML devices to reduce error.

Lastly,  $\eta_\tau$  is assumed to be constant for this work since it cannot be measured quantitatively. An approximation of the impacts of this term are discussed in Section 4.2.4

With these terms assumed to be constant, the only time dependent terms are  $\eta_{PL}$  and  $\eta_{EF}$ , and the time dependent version of Equation 4.1 can be written as

$$\frac{\eta_{EQE}(t)}{\eta_{EQE}^0} = \frac{\eta_{PL}(t)}{\eta_{PL}^0} \frac{\eta_{EF}(t)}{\eta_{EF}^0} \quad (4.2)$$

where  $X^0$  is the initial value of the parameter before degradation. Since  $\eta_{EQE}(t)$  is the luminance loss as a function of time, an independent measurement of  $\eta_{PL}$  would allow a full decoupling of  $\eta_{EQE}$  into  $\eta_{PL}$  and  $\eta_{EF}$ .

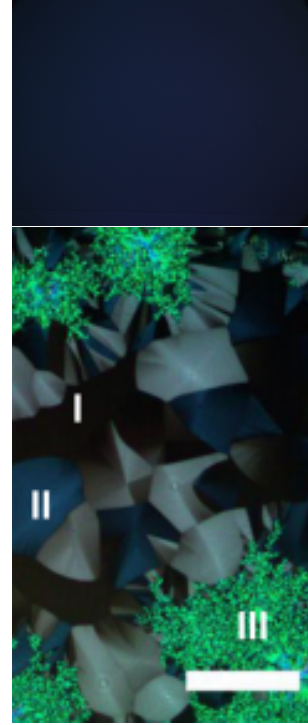


**Figure 4.1:** Cross polarized optical micrographs of (a) active device area (b) crystallized film from Fielitz *et al.*<sup>5</sup> (I) Orthorhombic phase, (II) Triclinic Phase, (III) 200  $\mu$ m scale bar

## 4.2 Photoluminescence Characterization

In order to independently measure  $\eta_{PL}$  during degradation, intermittent optical excitation is done using a laser, as shown in Figure fig:schematic. The laser forms a 1mm diameter circular spot on the active device

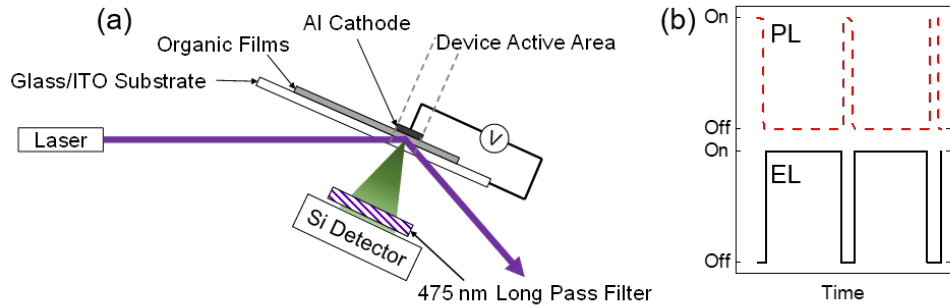


**Figure 4.2:** (a) Experimental configuration for the measurement of electro- (EL) and photoluminescence (PL) during OLED degradation. Laser excitation is incident on a subsection of the device area. The laser is aligned so that neither the incident nor reflected beam strikes the detector. Stray laser light is removed by a  $\lambda=475$  nm dielectric long pass filter. (b) Excitation scheme. EL and PL signals are probed independently with no temporal overlap. (c) External quantum efficiency versus current density and luminance for devices having emissive layer thickness of 10 nm, 20 nm and 30 nm.

area. The photoluminescence loss observed from this measurement can be related to the photoluminescence efficiency loss by

$$\frac{\eta_{PL}(t)}{\eta_{PL}^0} = \frac{L_{PL}(t)}{L_{PL}^0} \frac{I^0}{I(t)} \frac{\alpha^0}{\alpha(t)} \quad (4.3)$$

where  $L_{PL}$  is the experimentally measured luminance,  $I$  is the pump intensity, and  $\alpha$  is the film absorption. The pump intensity,  $I$ , can be measured and is observed to remain constant within error during the degradation. The absorption,  $\alpha$ , has also been measured before and after degradation, and is found to be constant within error. However, the sensitivity of the absorption measurement may not reflect the sensitivity of the  $\eta_{PL}$  measurement. An alternative method to verifying the  $\eta_{PL}$  measurement is presented in Section 4.2.5.

In traditional lifetime measurements, constant current density excitation is used. In order to measure  $\eta_{PL}$  as well, the current is paused every 10 minutes long enough to stabilize the laser and take a measurement, before the current is resumed. This takes on the order of 20 seconds, and is shown in Figure 4.2b. To make these measurements comparable with traditional lifetimes, time is reported as the elapsed time under

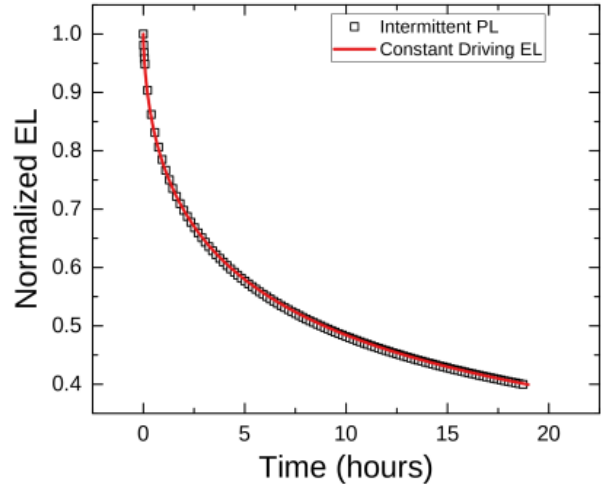


**Figure 4.3:** Lifetime obtained under a constant driving current is shown in red solid line. Lifetime under the same conditions but with PL measurement breaks is shown in open squares. Strong agreement is observed.

electrical current, with the laser breaks subtracted. This method has been shown to accurately match the traditional lifetime measurements, without additional degradation due to the PL measurement or relaxation from the breaks in current, as shown in Figure 4.3.

The accuracy of this measurement technique relies heavily on several testing considerations and assumptions. Important considerations of testing conditions and sources of error are discussed in the following sections.

### 4.2.1 Light Selection

Light sources for optical pumping are required to be powerful enough to pump the emitter sufficiently for measurement, stable enough to maintain output power for lifetimes over 100 hours, and long lived. Ideal candidates are lasers and high power lamps, though lamps often have a long warmup time, which is not ideal for the short on time needed for this experiment. Lamps do have the advantage that they can pump all of the device active area, getting a better sample of the behavior, though lasers can be expanded for the same effect.

During the optical pumping, it is important to only pump the emissive layer, and for the most direct measurement of  $\eta_{PL}$ , only the emitter molecule. To accomplish this, careful selection of wavelength must occur. Figure 4.4 shows the optical extinction coefficient for several materials. Ideally, the pump wavelength should be selected so that the emitter molecule has significant absorption, but the host does not. This is relatively easy for the green emitter,  $\text{Ir}(\text{ppy})_3$  where a wide range of pumps would work between 375 and 500 nm. However, this becomes extremely difficult for blue emitters such as  $\text{Fir}(\text{pic})$ , where hosts are more resonant with the emitter. In this case, the host may have to be pumped and exciton transfer from the host to the guest will be included in the measurement. Even with this, the transport layers would have to have higher triplet energies than the emitter.

Due to these limitations, lasers are ideal light sources for green emitters, since they are easily manipulated optically to pump multiple devices. Here, the limitations of available laser wavelengths are less important due to the wide pumping window. However, for blue emitters, a lamp may be a more viable option as it would allow filtering or monochromation to be more selective of wavelength.

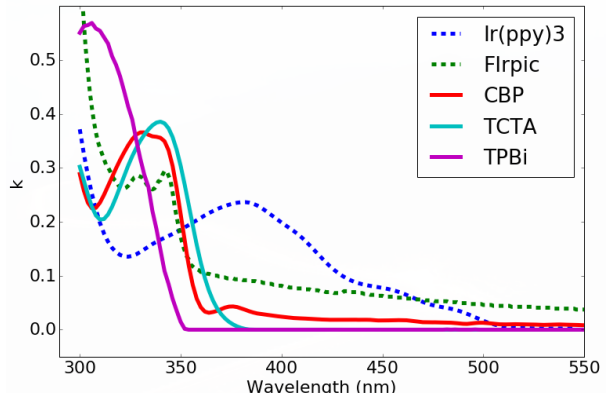


**Figure 4.4:** Extinction coefficients shown for the green emitter  $\text{Ir}(\text{ppy})_3$  and blue emitter  $\text{Fir}(\text{pic})$  as well as a few host materials.

### 4.2.2 Absorption - Recombination Overlap

For the measurement of  $\eta_{PL}$  to accurately reflect the useful degradation of the emissive layer, it is important for the optical pump absorption to agree with the recombination zone within the device. To illustrate this, Figure 4.5 shows a device where there is disagreement between the absorption and the recombination zone. Assuming an exciton driven process, defect formation and degradation will focus around the recombination zone. However, optical measurements will probe in the absorption region, which is less degraded than the electrically driven luminance is reflecting. This leads to a systematic underestimate of the actual  $\eta_{PL}$  degradation within the device.

To quantify this error for a particular device, a degradation and defect generation model must be employed in order to quantify the degradation profile within the device. Additionally, the absorption profile and recombination zone must be known (or estimated). The absorption profile can be calculated using a transfer matrix formalism.<sup>159</sup> The code used to calculate this is provided in Appendix D. The recombination zone can be measured using sensitizer molecules using the method outlined in Chapter 2.6. An excellent example of executing this analysis demonstrated by Bangsund et al. [86]

### 4.2.3 Contact Degradation

Exposure to UV light has been shown to enhance photodegradation of the organic/LiF/Al interface within devices.<sup>133,155</sup> This has been shown to be due to the dissociation and diffusion of positive ions from this interface, likely due to LiF. This becomes problematic in this measurement due to the  $\eta_{PL}$  measurement, as illustrated in Figure 4.6. Here, the optical pump has formed a dark spot on the active area of the device and accelerated degradation.

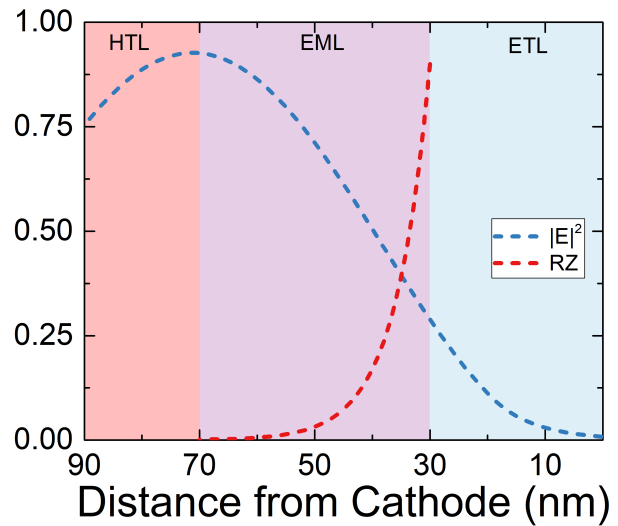


**Figure 4.5:** Exciton recombination zone (RZ) and pump intensity  $|E|^2$  for a hypothetical thick EML device are shown.

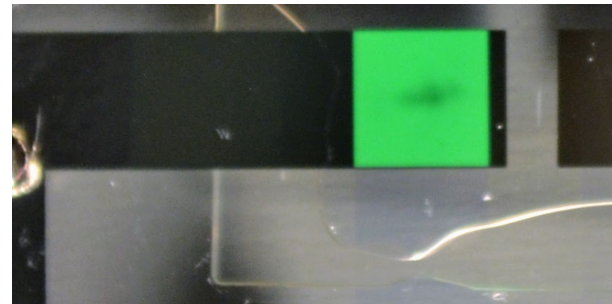


**Figure 4.6:** Dark spot formation on a device after exposure to a 405 nm laser.

To minimize this behavior, the laser intensity incident on the device must be kept low. We have found through trial and error that incident powers below  $10 \text{ mW/cm}^2$  for a  $405 \text{ nm}$  laser do not exhibit this dark spot formation. Devices can be inspected after lifetime testing to ensure that no degradation occurred. We have also observed that for longer wavelengths, the damage power threshold increases and higher power can be used.

#### 4.2.4 Quenching Changes During Degradation

Equation 4.1 introduces a quenching term,  $\eta_\tau$ , into  $\eta_{\text{EQE}}$ . This term captures bimolecular quenching losses which occur at high current and exciton densities. During lifetime measurements, the exciton density decreases as the efficiency reduces, which will change  $\eta_\tau$ . To quantify this, the model presented in Chapter 3 can be used. Using this dynamics formalism, we can define  $\eta_\tau$  as

$$\eta_\tau = \frac{1/\tau}{1/\tau + \frac{1}{2}k_{\text{TT}}n_{ex} + k_{\text{TP}}n_{pol}}. \quad (4.4)$$

To find  $\eta_\tau$  at the end of degradation, the change in  $n_{ex}$ ,  $n_{pol}$ , and  $\tau$  must be known. The change in  $\tau$  is known from  $\eta_{\text{PL}}$ , as discussed in Section 4.2.5. The exciton population,  $n_{ex}$ , is known from luminance as discussed in Chapter 3 and the temporal dependence follows the luminance loss assuming the radiative rate remains constant (which we assume). The polaron population likely increases to account for the decrease in our exciton density, but is difficult to quantify. Therefore, for this argument, we will assume it remains constant, though it will likely counteract some of the error that this method will estimate. With the temporal dependence of these quantities known, the time dependence of Equation 4.4 can be written as

$$\frac{\eta_\tau(t)}{\eta_\tau^0} = \frac{1/\tau}{1/\tau + \frac{1}{2}k_{\text{TT}}n_{ex} + k_{\text{TP}}n_{pol}} \frac{1/(R_{PL}(t)\tau) + \frac{1}{2}k_{\text{TT}}(R_{EL}n_{ex}) + k_{\text{TP}}n_{pol}}{1/(R_{PL}(t)\tau)} \quad (4.5)$$

where  $R_X$  is the degradation ratio of that term. Since degradation decoupling results are presented assuming  $\eta_\tau(t) = C$ , the presented out-coupling results can be corrected using  $\eta_\tau^0/\eta_\tau(t)$  as a multiplicative correction factor, presented in Figure 4.7. In this figure, minimal correction is needed for low exciton and polaron populations. This only becomes important in regimes where bimolecular quenching are strong.

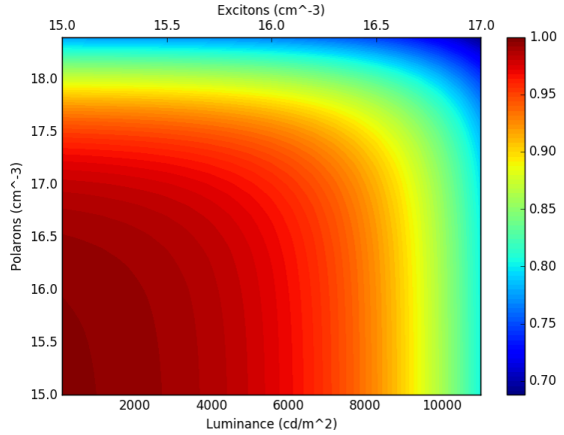


**Figure 4.7:** Multiplicative correction factor for exciton formation efficiency due to changes in quenching during lifetime. Shown as a function of polaron and exciton density as well as luminance, assuming a  $10 \text{ nm}$  emissive layer.

Again, it is important to note that if changes in the polaron population are accounted for, this correction factor would be further reduced.

#### 4.2.5 Verification with Exciton Lifetime

Alternative to the method for establishing the accuracy of the  $\eta_{PL}$  degradation presented in Equation 4.3, the exciton lifetime can be used. From photophysics, we have

$$\eta_{PL} = \frac{k_r}{k_r + k_{nr}} \quad \tau = \frac{1}{k_r + k_{nr}} \quad (4.6)$$

where  $k_r$  and  $k_{nr}$  are the radiative and non-radiative decay rates, respectively. From these equations, it is apparent that if  $k_r$  remains constant during the degradation,

$$\frac{\tau(t)}{\tau^0} = \frac{\eta_{PL}(t)}{\eta_{PL}^0}$$

Therefore, if the exciton lifetime,  $\tau$  is measured as a function of decay, it should have a 1-to-1 correlation with the observed PL loss if an accurate measure of  $\eta_{PL}$  is being conducted. To do this,  $\tau$  is measured from the transient photoluminescence decay at low pump intensity so that minimal triplet-triplet annihilation is observed. This is done on a 337 nm pulsed nitrogen laser, recorded with a fast photodiode connected to an oscilloscope. This have been done for a variety of device architectures, an example of the results being shown in Figure 4.8 for the devices discussed in Chapter 5.1. Here we see that we are accurately measuring  $\eta_{PL}$  for this device since a strong correlation is observed. The large amount of scatter observed in the 10 nm EML results are believed to be due to the thin EML and small amount of material, producing low signal.

It is important to note for this confirmation of  $\eta_{PL}$ , that this only demonstrates that no absorption or pump intensity deviations are causing error in our measurement. Since the transient photoluminescence and photoluminescence degradation are both pumped optically, both are subject to the recombination zone and absorption mismatch problem discussed in Section 4.2.2.

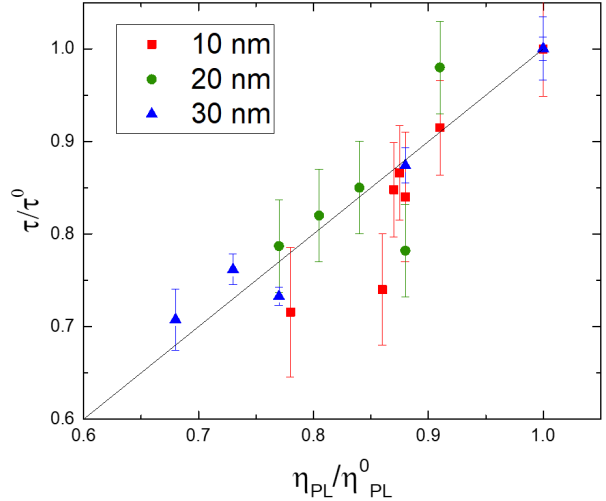


**Figure 4.8:** Exciton lifetime ratio extracted from transient PL measurements on degraded and undegraded devices as a function of PL degradation for several emissive layer thickness.

## 4.3 Experimental Implementation

### 4.3.1 Motivation

The conceptual idea of decoupling  $\eta_{EF}$  and  $\eta_{PL}$  during degradation was first investigated in our group without specialized equipment. Devices were fabricated and aged to varying points in the degradation in the same method as traditional lifetime measurements. After degradation, the device fluorescence was measured using a Photon Technologies International (PTI) fluorometer and compared to a control device. In this way, a PL curve can be produced, shown in Figure 4.9. In this graph, the control is taken as 1 at  $t = 0$  and each subsequent point consists of at least one device with three averaged fluorescence measurements for error bars. Though a proof of concept, this method is riddled with experimental problems. First off, experimental throughput is extremely low, since producing any  $\eta_{PL}$  curve requires separate aging of a device for every desired point. Even for the 5 point curves shown, this is extremely equipment heavy. Additionally, every point must be individually measured on the PTI, requiring substantial active lab time from the experimenter, as well as machine time.

The second and more restricting problem with this technique is the large error bars. As shown in Figure 4.9, with error bars of  $\pm 10\%$ , it is impossible to differentiate between devices. These large error bars for any individual point are caused by differences in loading into the PTI. In this measurement, the raw magnitude of the spectra is being extracted for comparison, and is highly dependent on the exact position of the sample within the excitation beam, as well as alignment with the collection optics and any angular deviation, changing reflection.

Furthermore, this method has no way of eliminating sample-to-sample variation from the  $\eta_{PL}$  curve without reproduction of all experimental points, requiring dramatic increase in machine time. Because of this, only speculation as to the accuracy of the curvature and validity of any data point can be made. Comparison between devices, especially in the temporal behavior becomes impractical due to the experimental time and uncertainty.

These initial experimental techniques demonstrated the need for a new testing method. Ideally, this method would automatically measure  $\eta_{PL}$  on the same sample, dramatically reducing experimental time and throughput limitations. This automatic measurement can have the added benefit of reducing measurement

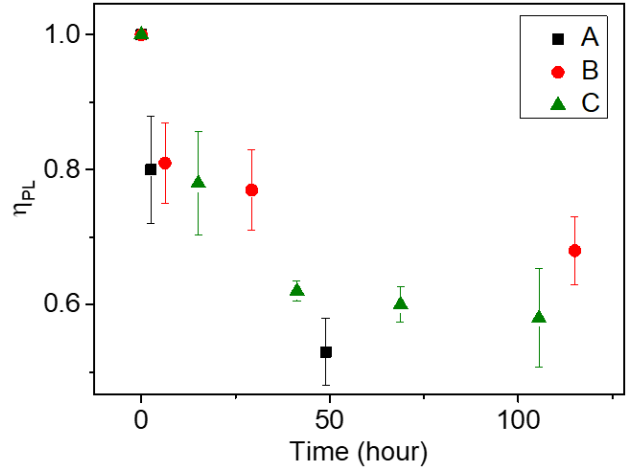


**Figure 4.9:** Initial Attempts at measuring  $\eta_{PL}$  during degradation using individual devices from the PTI.

error by holding the sample fixed throughout the decay and ensuring alignment. While sample-to-sample variation may still be an issue, it is no longer a problem in collecting a full dataset.

### 4.3.2 Development

In order to accomplish this automated measurement, the  $\eta_{PL}$  measurement needed to be conducted in an automated way. A light source capable of producing a constant illumination source over the course of hundreds of hours was needed. A lamp source, such as the PTI was initially considered, but found to have lifetimes similar to the OLED lifetimes. The lamp would not be able to be turned on and off throughout the test since lamps require substantial warmup time to achieve steady-state. Instead, a laser was used since they can be rapidly turned on and off, eliminating any need for blocking the light source during EL measurement. To account for any fluctuations in laser power over time, the power can be measured as a function of time and corrected for if needed.

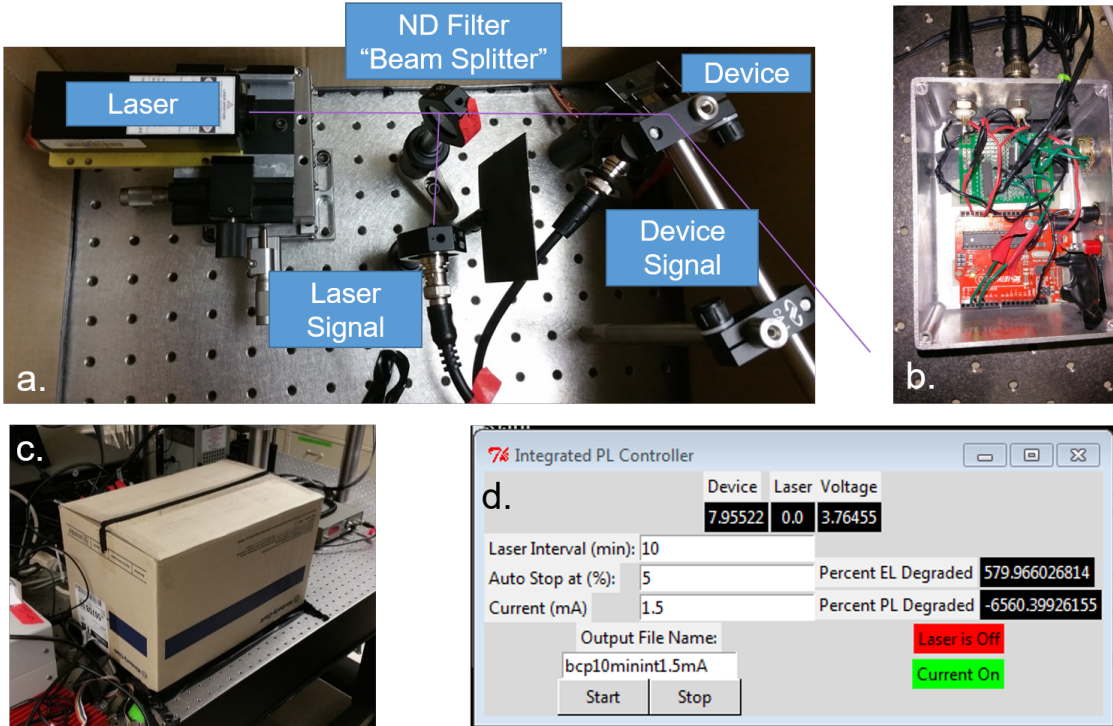


**Figure 4.10:** First generation lifetime box setup. a. Box layout b. Electronics c. dark enclosure (cardboard box) d. software interface

The first generation implementation of this setup is shown in Figure 4.10. This was a single channel device degradation, with the laser and splitter shown in the Figure 4.10a on the left and the device and photodiode collection shown on the right. Laser power detection relied on the split signal into the photodiode. The electronics are shown in Figure 4.10b and control the laser, current source and voltage measurements, and photodiode measurements. The laser was controlled by switching the interlock using an Arduino (red

PCB). A constant current source was implemented, with the current being set using the potentiometer on the front of the box. This had to be set and measured manually and was only recorded in the software, not set. Photodiode signals were converted to voltages using the green PCB and recorded using the Arduino. The software, shown in Figure 4.10d recorded all measurements and controlled the current, laser, and measurement timings. This was implemented in Python, using the Tk graphics library to create the GUI. At this initial stage, the software only had to interface with the Arduino, and did so using the Serial library. The Arduino was programmed to accept commands to turn on and off the laser and current, or report measurement values for voltage and the signals from either photodiode.

Soon after development, the limited resolution of the photodiode measurements, as well as the limitations of the manual current source were realized. In our traditional measurements of lifetime, a Keithley 26xx source meter was used for sourcing current and measuring signals. This Keithley was rapidly integrated into the system to allow better measurements and more accurate current control. The laser was replaced by a laser from Coherent which offered brighter and more stable power, as well as programmatic control.

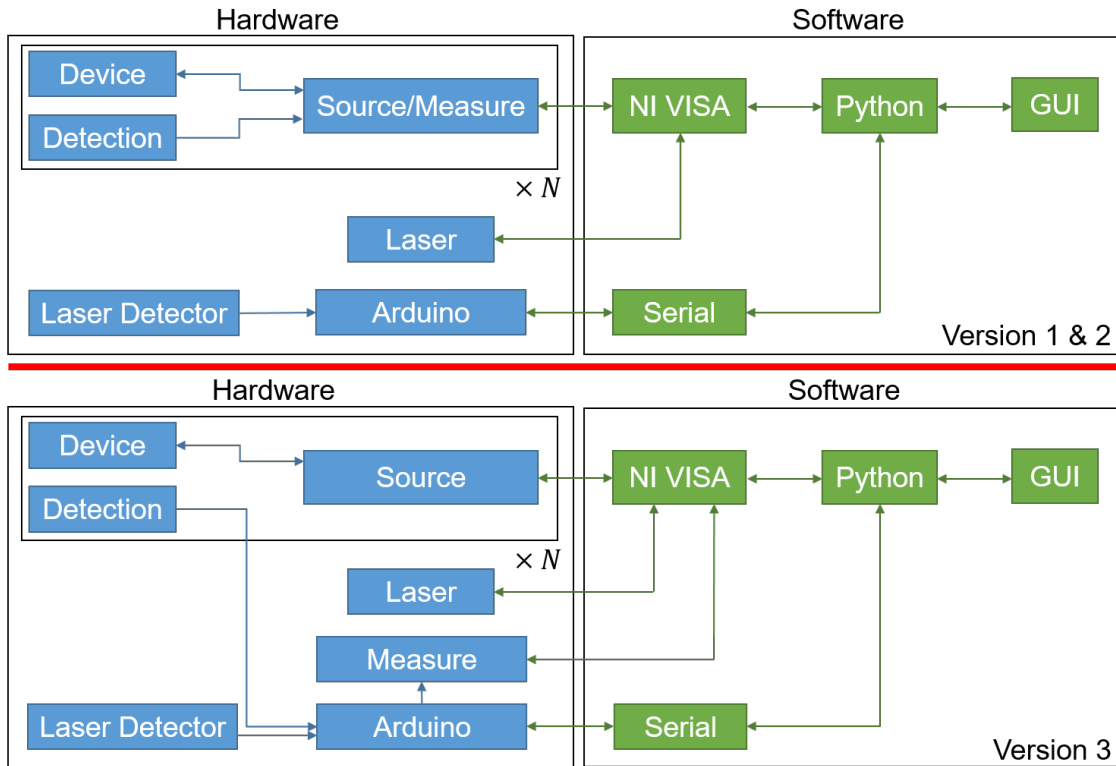


**Figure 4.11:** Box workflow summary. Top panel shows the operation of Boxes 1 and 2, bottom shows Box 3.

After this early development and hardware changes, little has changed about general workflow of this experiment. However, rather than individual boxes for each experiment, a single laser has been multiplexed to excite up to six different devices, dramatically cutting costs. Each experimental setup consisting of a single laser and multiple testing devices is termed a ‘box’; with each device residing in a compartment. A

summary of all hardware and software connections and control is shown in Figure 4.11. There are two different hardware configurations shown, interfacing with different source-meters. In the top configuration, each compartment is controlled by an individual Keithley source-meter. In the bottom configuration, to cut costs, a Keysight source-meter is used to supply current. The photodiodes in each box are measured by a single Keithley, switching between each compartment using an Arduino relay circuit. This allows a dramatic reduction in hardware and costs.

The next two sections go into detail regarding the implementation of the hardware and software setups.

### 4.3.3 Hardware Setup

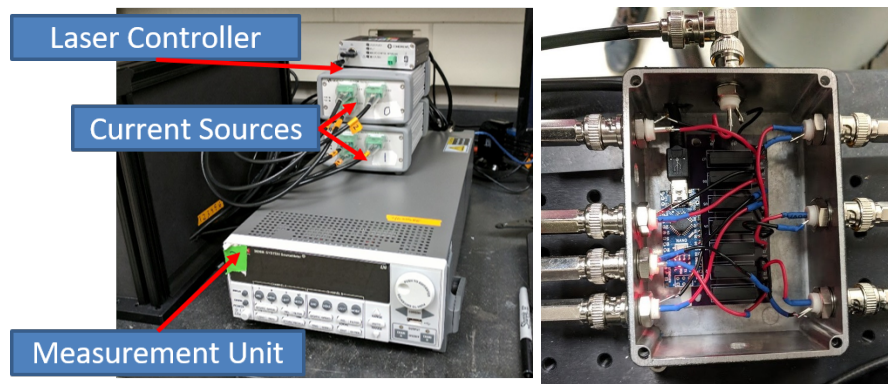
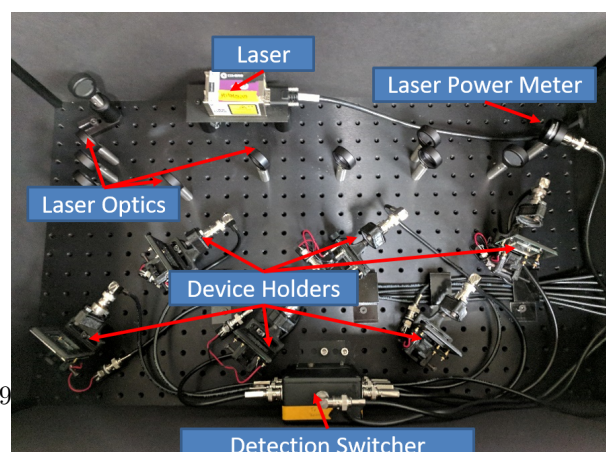


**Figure 4.12:** Source-Measure hardware and laser controller

Hardware for this setup requires control of current sources, voltage measurement, light source, as well as light measurements. Currently, there are four operational testing setups, termed “boxes”, with varying hardware configurations. Several boxes are multiplexed to allow multiple measurements from the multiple compartments. Source units for providing current and voltage measurements have used either the Keithley 26xx or Keysight u2722a source meters. The Keithley 26xx units are a two channel, low noise, high precision unit. The Keysight u2722a provides three channels with higher noise and lower precision at a lower price point per channel. Light sources for all boxes are conducted using Coherent OBIS lasers, with wavelengths of either 405 nm or 473 nm. Light measurements are conducted using the Keithley 26xx for all boxes, connected to a Hamamatsu S2281 photodiode. Figure 4.12a shows the electronic hardware setup for a box utilizing Keysights for source units and a Keithley for measurement. To reduce measurement units, the photodiodes in each compartment can be switched between using an Arduino relay system shown in Figure 4.12b. All of these pieces of hardware are compatible with the National



Instrument VISA command library for control.

Each device is held by a custom 3D printed vertical mount. The photodiode is wired into this mount with enough space for the laser to avoid the diode. A long pass filter is provided to minimize stray laser signal. The laser is optically split into six paths using beam splitters and neutral density filters are used where necessary to normalize laser power on each device.

#### 4.3.4 Software Development

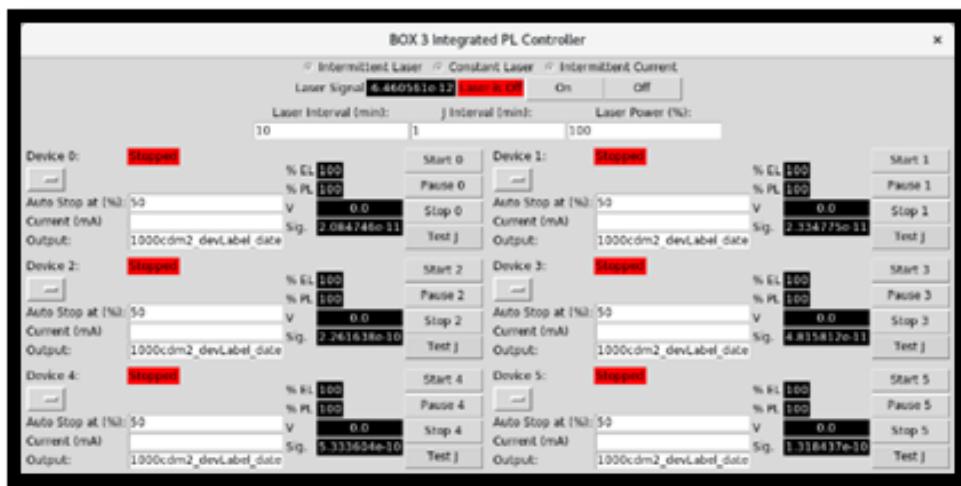


**Figure 4.14:** 6 channel software controller. Selection of test type, laser control for alignment, and global settings are accessible on the top of the interface. Individual channel settings are grouped on the bottom.

Software to control this measurements is implemented by myself in Python and outlined in Appendix E. The code is able to control the hardware to run constant current, intermittent laser integrated PL measurements, optical degradation, as well as optical degradation with current break degradations. The frequency of laser breaks and laser power can be controlled on a whole box level. Laser emission can be turned on for alignment. The software is able to be configured to the number of channels available depending on the hardware. Each channel can be individually controlled for current, stop, and labeling.

To organize collected data, a database for all lab data has been developed and is discussed in Chapter 7. Lifetimes integrate with this system when lifetimes are started, using the interface shown in Figure 4.15. Here, a lifetime test is connected to a particular growth, as well as the individual substrate and device pixel. Information about the lifetime is also connected. The lifetime operating current can be determined for a desired luminance by utilizing the current-voltage-luminance curve for the exact device within this interface.

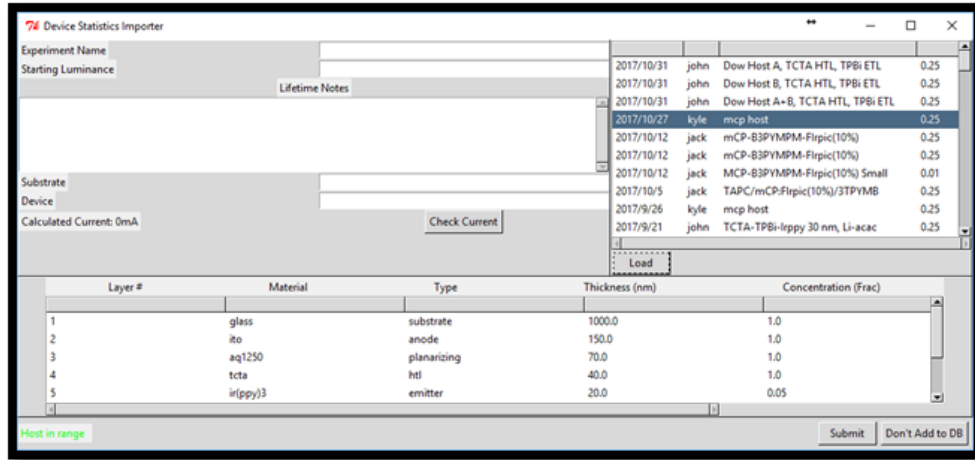


**Figure 4.15:** Test information for database import interface. The top left panel collects information about the specific device and lifetime. The right panel connects the device to a particular growth and architecture. The bottom panel confirms the architecture.

Additional notes and information are also able to be stored.

## 4.4 Conclusion

This chapter has outlined a system for decoupling degradation during operational lifetimes. Extensive care has been taken to outline the assumptions and assess error within the extracted parameters. Many of these assumptions need to be assessed for any device system to be tested to ensure accuracy. Applying this method to lifetime decoupling in device systems is the subject of Chapter 5.

# Chapter 5

## Applied Integrated Lifetimes

Chapter 4 discussed a novel approach for decoupling lifetime. The studies in this chapter use this technique and exploit this additional information to better understand device behavior. This includes a discussions of Hershey et al. [85] in Section 5.1, Bangsund et al. [86] in Section 5.2, and Bangsund and Hershey [158] in Section 5.3, as well as unpublished work.

### 5.1 CBP Host Thickness

#### 5.1.1 Motivation and Experimental

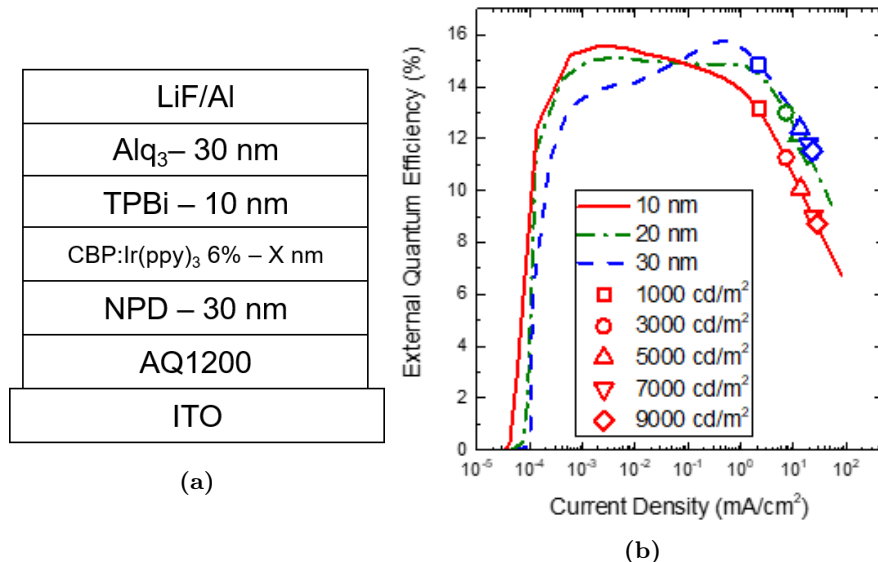


**Figure 5.1:** a. Device architecture, featuring EML thicknesses of  $X=10,20$ , and  $30\text{ nm}$ . b. External Quantum Efficiency ( $\eta_{EQE}$ ) for the three architectures. Operational points for lifetime are shown in symbols.

Carbazole materials are archotypical hosts for phosphorescent devices, most common among them be-

ing 4,4'-Bis(N-carbazolyl)-1,1'-biphenyl (CBP).<sup>30,54,135,160–164</sup> Therefore, CBP was used as a preliminary system to demonstrate the decoupling technique. Devices consisted of a 40-nm-thick hole-injection layer of Plexcore AQ1200 spun-cast on a glass substrate coated with a 150-nm-thick layer of indium-tin-oxide (ITO), followed by a 30-nm-thick hole-transport layer of N,N' -Bis(naphthalen-1-yl)-N,N' -bis(phenyl)-benzidine (NPD), and an EML of 4,4'-Bis(N-carbazolyl)-1,1'-biphenyl (CBP) doped at 6 vol. All devices were fabricated according to the processes outlined in Chapter 2.2. The structure shown in Figure 5.1a was used with EML thicknesses of X=10, 20, and 30 nm. The  $\eta_{EQE}$  for all three EML thicknesses, shown in Figure 5.1b, shows maximum efficiencies of 15.7%, 15.3%, and 15.7% for EML thicknesses of 10, 20, 30 nm, respectively. Though similar in peak value, as thicknesses increases, the peak  $\eta_{EQE}$  shifts to higher current. This is indicative of a shift in the charge dynamics and possible location of the recombination zone. Recombination zone has been previously linked with lifetime, with a longer lifetime expected for thicker RZ.<sup>105–114</sup> Using an ambipolar host such as CBP, one would expect that expanding the EML would result in a wider RZ and thus longer lifetime.

### 5.1.2 Results

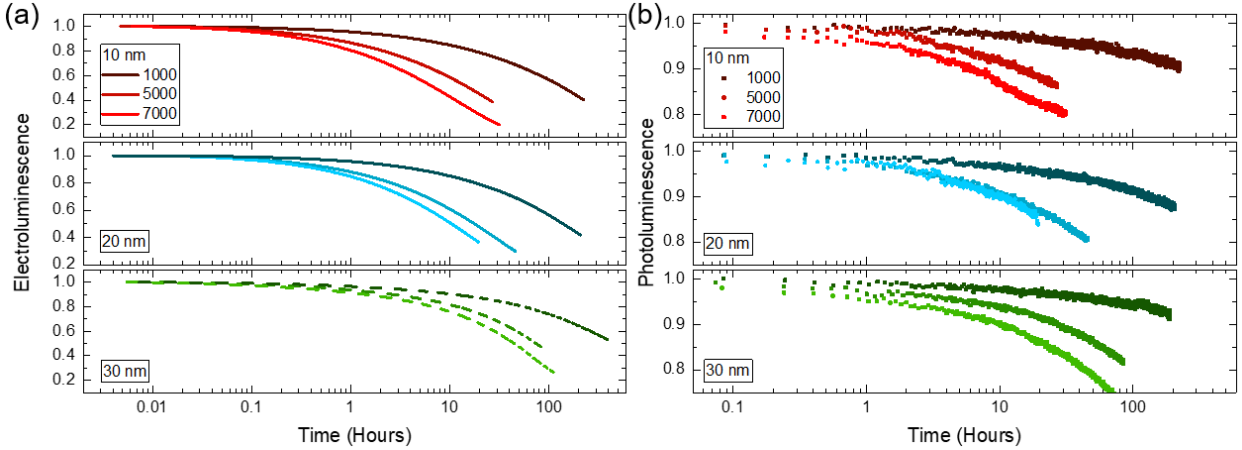


**Figure 5.2:** Device decay curves for multiple values of the initial luminance as a function of emissive layer thickness. Loss in (a) electroluminescence (EL) and (b) photoluminescence (PL) are shown and decrease monotonically with increasing luminance. For devices with a 10-nm-thick emissive layer, initial luminance values are  $1000\text{ }cd/m^2$ ,  $5000\text{ }cd/m^2$ , and  $7000\text{ }cd/m^2$ . For devices with a 20-nm- or 30-nm-thick emissive layer, initial luminance values are  $1000\text{ }cd/m^2$ ,  $5000\text{ }cd/m^2$ , and  $7100\text{ }cd/m^2$ .

Figure 5.2a shows the traditional EL lifetimes of these devices, and indeed the 30 nm EML shows a longer lifetime than the 10 and 20 nm. In Figure 5.2b, the intermittent  $\eta_{PL}$  measurements can be seen, showing the advantage of this technique and the large amount of additional data that is available. The operational conditions of each device is shown in Table 5.1. Similar currents are used across EML thicknesses, but voltage increases slightly with thickness, as might be expected.

To be able to extract  $\eta_{PL}$  and  $\eta_{EF}$ ,  $\eta_{OC}$  and  $\chi$  cannot change during degradation. No birefringence was

observed under cross polarization before or after degradation, suggesting the absence of large-scale crystallization which would change  $\eta_{OC}$ . No new emission features are observed with degradation, suggesting that the emissive state is unchanged and  $\chi$  can be assumed constant. With these assumptions satisfied,  $\eta_{PL}$  and  $\eta_{EF}$  can be extracted from the measured PL intensity, and are shown in Figure 5.3.

The lifetime decreases with luminance for all architectures. While a reduction in the EL lifetime is observed in Figures 5.2 and 5.3 in reducing device thickness from 30 nm to 20 nm, little difference is seen between devices having EML thicknesses of 20 nm and 10 nm. The degradation in the PL intensity does not appear to be a strong function of EML thickness. Indeed, comparing the EL and PL lifetimes with the extracted degradation in exciton formation shows that the EL decay is dominated by a loss in the efficiency of

exciton formation with  $\eta_{EF}$  reaching 60% of its initial value by the time EL has reached 50%. A substantial component of this decay is likely due to non-radiative recombination center formation.<sup>118,122</sup> Over this same period, the PL intensity has only degraded by 10% of its initial value.

The similarity in PL degradation observed across all EML thicknesses suggests that the exciton and polaron densities are similar between these devices,<sup>69–71</sup> thus have similar exciton recombination zone widths. The accelerated degradation in the exciton formation efficiency ( $\eta_{EF}$ ) observed for devices with EML thicknesses of 10 nm and 20 nm suggests that the recombination zone samples the EML/TPBi interface, which has been previously shown to cause degradation.<sup>116,131</sup> This change in recombination zone location is also suggested by the  $\eta_{EQE}$  behavior shifting peak location, shown in Figure 5.1b. To validate this suggestion, the position of the recombination zone was assessed in the devices with EML thickness of 20 and 30 nm devices using a quenching TPTBP sensitizer. The position of the recombination zone can be inferred by the corresponding reduction in device  $\eta_{EQE}$  due to quenching by TPTBP.<sup>68</sup> The sensitized 30-nm-thick EML devices showed no quenching, suggesting no recombination near the interface, while devices with a 20-nm-thick EML showed quenching only at the EML/TPBi interface, confirming the position of the recombination zone at that interface. Devices with a 10-nm-thick EML exhibited changing current-voltage behavior when sensitized with TPTBP, and thus PtTPTBP, an emissive sensitizer with a peak wavelength of 770 nm, was used in

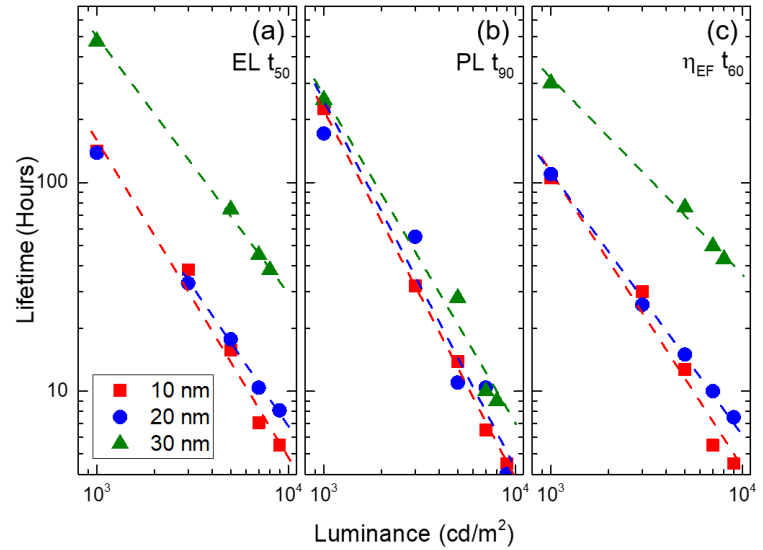


**Figure 5.3:** Extracted lifetimes for all 3 architectures as a function of luminance.

2-nm-thick strips on either side of the EML at 0.5 vol. %. This configuration was able to match the current-voltage behavior of the control device while permitting the measurement of emission from PtTPTBP. For devices with a 10-nm-thick EML, strong emission from PtTPTBP is observed from the EML/TPBi interface and weak emission seen from the EML/NPD interface. These quenching experiments are shown in Figure 5.4. These results suggest that for devices with an EML thickness of 10 nm or 20 nm, the recombination zone samples the EML/TPBi interface, accelerating exciton formation loss. While detailed analysis of the relevant degradation mechanism is the subject of future work, previous work has suggested a role played by exciton-polaron interactions.<sup>69,103,118,122,130</sup>

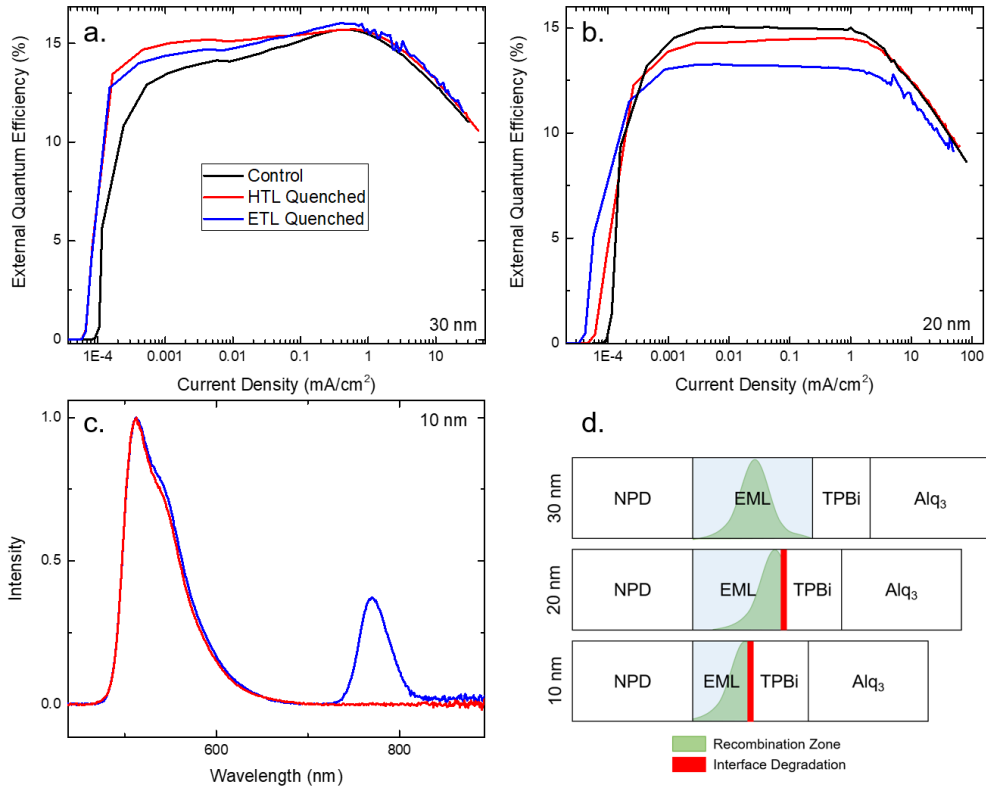


**Figure 5.4:** a. TPTBP quenched 30 nm devices. No quenching is observed. b. TPTBP quenched 20 nm devices. Quenching is observed for the ETL side quencher, and minimally for the HTL side. c. PtTPTBP quenched 10 nm EML devices. Emission from the sensitizer only at the ETL. d. Summary of recombination zone measurements.

### 5.1.3 Conclusion

The additional information offered by this technique is directed at improving the screening of active materials and device architectures for the realization of long-lived OLEDs. Device degradation that is dominated by a loss in either  $\eta_{EF}$  or  $\eta_{PL}$  implies a dominant rate process and an opportunity for improvement of materials or architecture. In systems using Ir(ppy)<sub>3</sub>, a relatively stable emitter with demonstrated long optical and electrical lifetimes,<sup>6</sup> losses in the exciton formation efficiency are expected to represent the majority

fraction of degradation. However, for novel molecules, limiting processes are largely unknown and would benefit from the separation of emitter and exciton formation efficiency loss. PL degradation could become increasingly important for blue-emitting species where the high exciton energies could contribute to material degradation.<sup>6,87,165–168</sup> This screening process would be dramatically improved if  $\eta_{\text{EF}}$  and  $\eta_{\text{PL}}$  can be mechanistically modeled. With additional datasets, modeling and understanding of degradation mechanisms can be improved and help to identify limiting processes. The model presented in Giebink et al. [69] could easily be adapted to separate losses that would be captured by  $\eta_{\text{PL}}$  and  $\eta_{\text{EF}}$ , and would provide further checks to this overparameterized model.

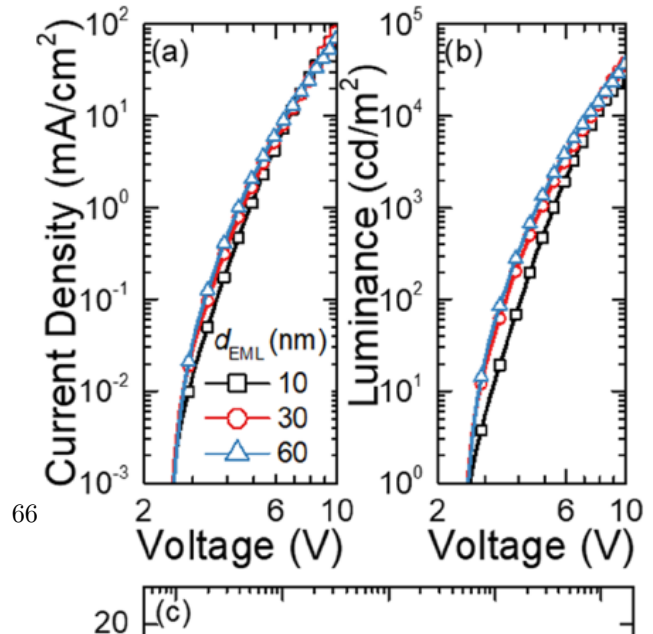
In summary, this work presents a method for decoupling optical and electrical losses during OLED operational decay by attributing the overall reduction in electroluminescence to a loss in  $\eta_{\text{PL}}$  or the exciton formation efficiency through  $\eta_{\text{EF}}$ . Model devices are shown as a function of luminance, with a loss in  $\eta_{\text{EF}}$  shown to be the limiting factor for the short-lived devices. By measuring the recombination zone, these devices are shown to be subject to interfacial degradation, only seen in narrow EML devices. Contrary to the expectation, the RZ is not found to expand with the EML thickness, but rather to shift within the device. This technique allows access to additional experimental information which can offer insight about the degradation mechanism and understanding of device luminance loss. This added information can be used to aid future efforts in modeling degradation.

## 5.2 MEML Luminance Scaling

This section outlines the work done in Bangsund and Hershey [158]. All figures are reproduced from this work, while the text is an adapted version of the paper text.

### 5.2.1 Motivation

As discussed in Section 5.1, recombination zone width has been extensively connected with lifetime, mediated by the exciton and polaron populations.<sup>6,69,84,103,104,106,108,109,169</sup> However, despite this observed trend with recombination zone thickness, the specific role of the RZ in degradation kinetics is still an active area of investigation. Using a mixed emissive layer (MEML) architecture, this work seeks to provide a more concrete connec-



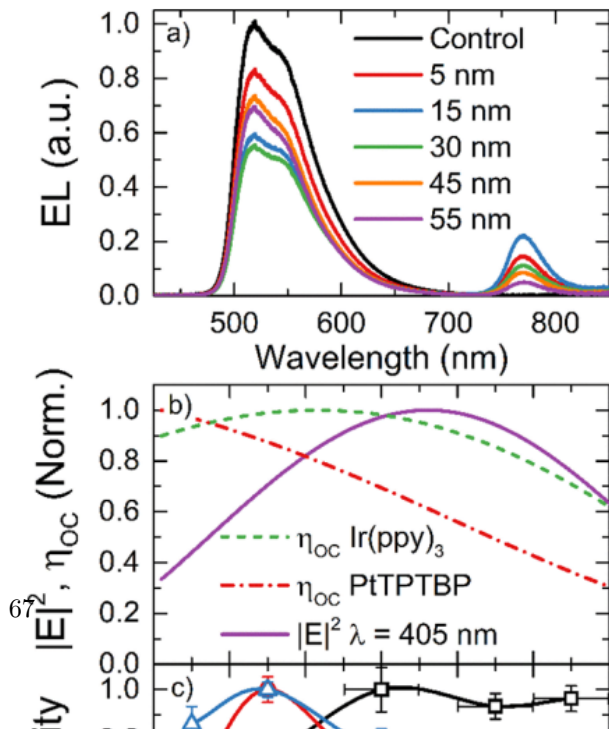
tion between the recombination zone and degradation within the same system.

### 5.2.2 Experimental

Devices consisted of a 60-nm-thick hole injection layer (HIL) of poly(thiophene-3-[2[(2-methoxyethoxy)ethoxy]-2,5-diyl](AQ1200, Sigma Aldrich), a 4,4',4''-tris(N-carbazolyl)triphenylamine (TCTA, TCI America) hole-transport layer (HTL), a mixed-host emissive layer (M-EML) consisting of a 47.5 vol. All layers were deposited according to the procedures outlined in Section 2.2. When varying the M-EML thickness (10 nm, 30 nm, 60 nm), the HTL and ETL thicknesses are varied equally to maintain a total device thickness of 100 nm. Device characteristics are shown in Figure 5.5, with the efficiency increasing slightly from 17% to 19% as the EML thickness increases from 10 to 60 nm.

This device architecture system, shown in the inset of Figure 5.5, was chosen because of its broad recombination zone, which spans the entire EML.<sup>68</sup> Because of this property, the MEML thickness,  $d_{eml}$  can be taken as a proxy for the RZ width, and the exciton density can be controlled by modifying the EML. The increase in recombination zone thickness is evidenced by the change in onset of the roll-off with increasing RZ width, seen in Figure 5.5c.

To experimentally confirm the RZ breadth, the 60 nm EML architecture was investigated using PtTPTBP as a sensitizer, using the methodology outlined in Chapter 2.6. The exciton density is found to remain above 60% of the peak across the entire 60 nm M-EML at a current density of 10 mA/cm<sup>2</sup>, shown in Figure 5.6. As current density increases from 0.1 mA/cm<sup>2</sup> to 10 mA/cm<sup>2</sup>, the peak of the RZ migrates from the ETL side to the HTL side of the M-EML. These findings are consistent



with other reports for similar device architectures,<sup>68</sup> and confirm that  $d_{eml}$  is a good proxy for RZ width.

The 60 nm EML is the thickest investigated EML thickness and should be subject to the most variation in RZ intensity across the EML. Therefore, thinner EML devices are also assumed to have a RZ spanning the EML.

### 5.2.3 Results

The degradation of these devices at an initial luminescence of  $L_0=3,000$  cd/m<sup>2</sup> is shown in Figure 5.7a.

The EL lifetime increases by approximately a factor of 3 in increasing the thickness from 10 nm to 60 nm, and nearly all this enhancement can be attributed to a reduced rate of PL degradation, shown in Figure 5.7b.

No trend with thickness is apparent in the  $\eta_{EF}$  decays, which are all within typical device-to-device variation. In contrast, the PL decays show a dramatic separation with thickness. We also note that a reduction in  $\eta_{EF}$  dominates the overall degradation rate in the 30 nm and 60 nm thick M-EML devices, but is comparable to PL losses in the 10 nm M-EML device. These results suggest that reduced degradation in emissive layer PL efficiency may be the primary reason for enhanced stability in M-EML architectures, as compared to their single-host counterparts. Moreover, the combination of improved efficiency roll-off and PL lifetime with an increased RZ width, and thus decreased exciton density, provides further evidence of a link between bimolecular annihilation events and the degradation of PL efficiency.<sup>169</sup> Losses in  $\eta_{EF}$ , however, appear to be relatively insensitive to exciton density.

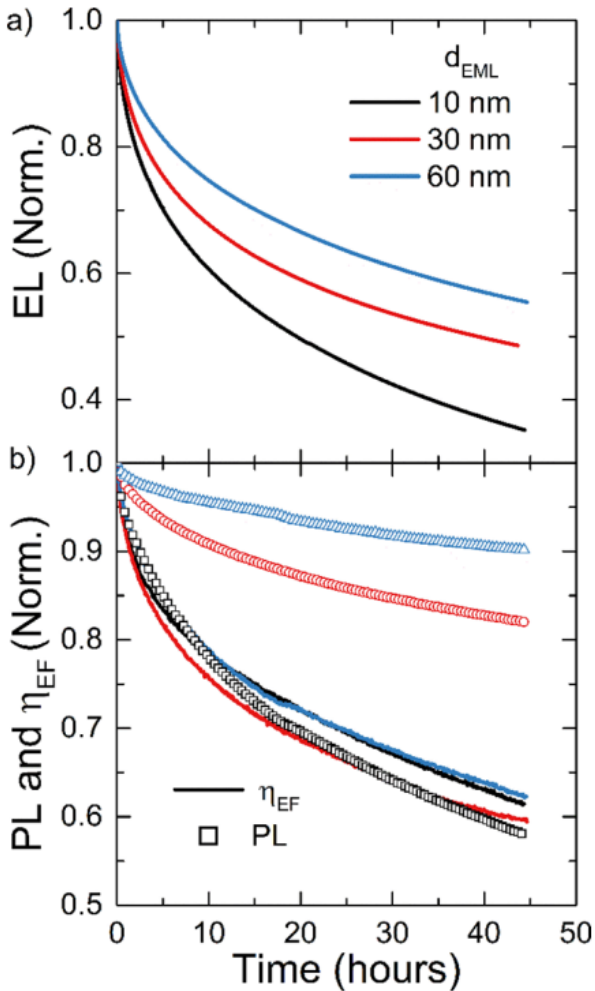


**Figure 5.7:** a. EL lifetime at  $3,000 \text{ cd/m}^2$  for EML thicknesses of 10,30,60 nm. b. The corresponding  $\eta_{PL}$  and  $\eta_{EF}$  degradation.

To show that exciton density and PL loss are intimately related, the exciton density was matched between the architectures by scaling the luminance to the EML thickness ratio. The 10, 30, and 60 nm EML devices were operated at initial luminances of 1,000, 3,000, and  $6,000 \text{ cd/m}^2$ , respectively. The results of this aging are shown in Figure 5.8. PL degradation is nearly identical for 10, 30, and 60 nm M-EML devices operated at luminances of 1,000, 3,000, and  $6,000 \text{ cd/m}^2$ , respectively. Exciton formation efficiency losses, on the other hand, are rapidly accelerated as luminance is increased. At

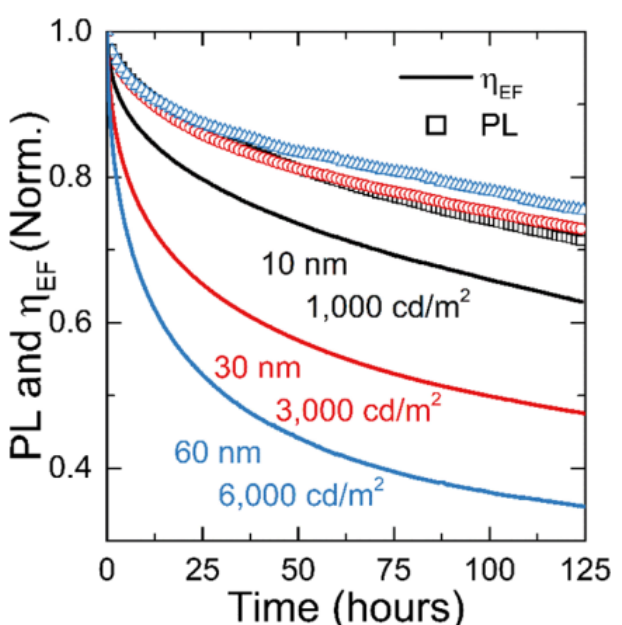


**Figure 5.8:** Lifetimes of devices with luminance scaled to match the EML thickness. PL collapses due to matched exciton density.

long times, the PL degradation slows slightly with increasing M-EML thickness, and this is attributed to the large differences in exciton formation efficiency losses. The exciton density does not remain matched over the course of the entire test due to these differences in  $\eta_{EF}$  losses, and consequently the formation rate for exciton quenchers will be reduced at long times in thicker M-EML devices. This observation of matched PL losses under scaled luminance has been reproduced under a range of scaled luminances from 330 cd/m<sup>2</sup> to 15,000 cd/m<sup>2</sup>, showing the same trend. Despite comparable exciton densities in the emissive layer, exciton formation efficiency losses differ substantially, and appear to scale with increased luminance and current density. Increased current density would result in a larger polaron density in the transport layers and could lead to an increase in the rate of defect formation mediated by unstable cationic or anionic molecules. Alternatively, the trend with luminance could be explained as an increase in interfacial photodegradation of the cathode or anode due to device electroluminescence.<sup>wang2012, 133,170</sup>

An alternative approach to investigating this connection is to look at the scaling relationships with luminance and exciton density. OLED lifetime has been widely observed to follow a  $1/L_0^n$  relationship,<sup>42</sup> where  $L_0$  is the initial luminance, and  $n$  is a device specific parameter typically between 1-2. For these devices,  $n = 1.8 \pm 0.1$  for the  $t_{50}$  of EL and is independent of M-EML thickness. As shown in Figure 5.9a, the degradation in  $\eta_{PL}$  and  $\eta_{EF}$  for a 60 nm MEML show similar acceleration behavior as a function of luminance, with  $n = 1.8$  and  $n = 1.75$ , respectively. Comparable slopes are seen for 10 nm and 30 nm M-EML devices.

However, when scaled by  $1/d_{EML}$ , as displayed in Figure 5.9b,  $\eta_{EF}$  and  $\eta_{PL}$  show distinct scaling behavior. While PL  $t_{85}$  shows a slope of  $n = 1.9 \pm 0.3$ , almost identical to the slope under luminance acceleration,  $\eta_{EF} t_{85}$  shows a much shallower slope of  $n = 0.5 \pm 0.2$  (decreasing to  $n = 0.3 \pm 0.3$  at 10,000 cd/m<sup>2</sup>). This raises several important implications. First, the identical slopes for PL provide further evidence that PL losses in this system are determined by the exciton density and the width of the recombination zone, and imply that there is a direct scaling law between recombination zone width and PL lifetime. While polaron density can play a role in PL degradation as well,<sup>27,43</sup> it is unlikely that polaron density scales identically with both luminance and  $d_{EML}$ , implying that a single exciton driven or an exciton-exciton annihilation driven degradation mechanism is dominant in this system.

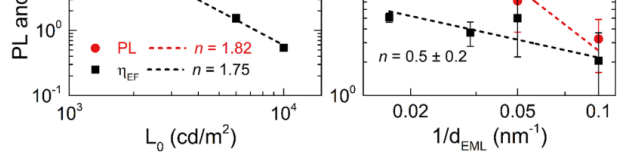


**Figure 5.9:** Scaling behavior of  $\eta_{PL}$  and  $\eta_{EF}$  as a function of a) luminance and b) exciton density.

Second, the shallow dependence of  $\eta_{\text{EF}} t_{85}$  on RZ width (and hence exciton density) shown in Figure 5.9b suggests that excitons play a lesser role in  $\eta_{\text{EF}}$  degradation. Notably, the difference in scaling with  $L_0$  and  $d_{\text{EML}}$  for  $\eta_{\text{EF}} t_{85}$  suggests that multiple degradation mechanisms comprise the total  $\eta_{\text{EF}}$  loss. Exciton formation loss is often attributed to the accumulation of non-radiative recombination centers in the emissive layer,<sup>118,122</sup> and has been linked to exciton-polaron interactions.<sup>171</sup> The shallow dependence on RZ width (and hence exciton density) shown in Figure 5.9b suggests that the  $d_{\text{EML}}$ -dependent increase in  $\eta_{\text{EF}}$  degradation reflects the generation of non-radiative recombination centers by an exciton-mediated process, consistent with these reports. However, this mechanism alone cannot fully account for degradation in  $\eta_{\text{EF}}$ , as the slope against initial luminance scaling with  $L_0$  is much steeper (Figure 5.9a). This contrasting behavior suggests that a second mechanism which is independent of emissive layer exciton density governs  $\eta_{\text{EF}}$  losses. This behavior is consistent with degradation mediated primarily by polarons or photodegradation of the cathode or anode interface, and may originate outside of the emissive layer.<sup>133,170</sup>

These findings have implications for efforts in modeling OLED lifetime. Most modeling approaches assume that the same defect population responsible for exciton quenching was also responsible for non-radiative recombination of charge carriers. This implies that the quenching population resides entirely in the emissive layer.<sup>2,7<sup>69,105</sup></sup> Defect populations external to the emissive layer have been considered, but only for the purposes of fitting voltage rise.<sup>45<sup>71</sup></sup> In all cases, the generation of defects is proposed to proceed via bimolecular quenching processes. While these treatments have yielded reasonable fits of the overall degradation behavior, they are unable to capture the behavior observed here. Exciton formation and PL degradation would be expected to trend together within these formalisms, whereas Figure 5.9 shows clearly distinct scaling behavior. Our results thus show that losses to  $\eta_{\text{PL}}$  and  $\eta_{\text{EF}}$  likely originate from kinetically distinct mechanisms. Moreover, the weak dependence of  $\eta_{\text{EF}}$  on exciton density indicates that degradation defects external to the emissive layer may play an important role in luminance loss, and should be considered in future modeling attempts. Non-radiative recombination centers could have suitable energetics to serve as exciton quenchers, and vice versa. However, because losses in  $\eta_{\text{EF}}$  and  $\eta_{\text{PL}}$  show different dependences with initial luminance and EML thickness, the exciton quenchers formed in the EML are likely inefficient non-radiative recombination centers for charge carriers.

#### 5.2.4 Conclusion

In conclusion, we find that broadening the recombination zone (RZ) sharply reduces the rate of PL degradation, showing a similar scaling relationship as with initial luminance variation. This confirms that PL degradation is strongly dependent on exciton density and has minimal dependence on changes in the po-

laron density as driven by the RZ. However, losses in the exciton formation efficiency ( $\eta_{\text{EF}}$ ) show a weaker dependence on RZ width, suggesting that  $\eta_{\text{EF}}$  losses are less sensitive to exciton density and may partly originate outside of the M-EML in this system. Notably, the different dependences of PL and exciton formation efficiency loss on RZ width provide clear evidence that kinetically distinct pathways drive OLED degradation, and that a single degradation mechanism cannot be assumed when attempting to model device lifetime. These results highlight the capability of decoupled measurements of  $\eta_{\text{PL}}$  and  $\eta_{\text{EF}}$  losses to yield useful diagnostic insight into the source of device instability and shed light on the kinetics of degradation and the nature of defects.

### 5.3 Dow Cohost

### 5.4 NPD Study

Long lived deep blue emitters are important for developing displays. This is still an active field of research.<sup>172,173</sup>

$d_{EML}$ (nm)	$L_0$ (cd/m <sup>2</sup> )	$J$ (mA/cm <sup>2</sup> )	$V_0$ (V)	$t_{50}$ (hours)
10	1000	2.2	4.2	139.0
	3000	7.2	5.1	39.9
	5000	13.6	5.4	15.8
	7000	14.4	6.2	6.9
	9000	28.0	6.3	5.3
20	1000	2.2	5.4	141.1
	3000	7.2	6.0	33.1
	5000	12.4	7.2	17.2
	7100	19.2	7.3	10.0
	9000	24.0	7.5	8.0
30	1000	2.2	5.9	474
	5000	13.6	7.3	74.4
	7100	19.6	7.6	46
	8000	22.4	7.7	38.1

**Table 5.1:** Summary of device lifetimes. For each device, the starting luminance ( $L_0$ ), current density ( $J$ ), starting voltage ( $V_0$ ) and time at which 50% of the initial luminance is reached ( $t_{50}$ ) are reported.

## Chapter 6

# Novel Blue Emitter Development

6.1 Molecular Systems

6.2 Performance Optimization

6.3 Solution Molecular Aggregation

## Chapter 7

# Data Management for Devices

# Chapter 8

## Modeling Out-Coupling

### 8.1 Theory

Code used for implementation of this theory is provided in Appendix D

### 8.2 Recombination Zone Overlap During Lifetime

## Chapter 9

### Future Research

# Bibliography

- (1) Maldonis, J. J.; Hwang, J.; Voyles, P. M. *Computer Physics Communications* **2017**, *213*, 217–222.
- (2) Maldonis, J. J.; Zhang, P.; Besser, M.; Kramer, M.; Voyles, P. M. *Microscopy and Microanalysis* **2015**, *21*, 1659–1660.
- (3) Zhang, P.; Maldonis, J. J.; Liu, Z.; Schroers, J.; Voyles, P. M. *Submitted* **2017**, DOI: [arXiv:1710.04791v2](https://arxiv.org/abs/1710.04791v2).
- (4) Zhang, P.; Maldonis, J. J.; Besser, M. F.; Kramer, M. J.; Voyles, P. M. *Acta Materialia* **2016**, *109*, 103–114.
- (5) Fielitz, T. R.; Holmes, R. J. *Crystal Growth and Design* **2016**, *16*, 4720–4726.
- (6) Scholz, S.; Kondakov, D. Y.; Lüssem, B.; Leo, K. *Chemical Reviews* **2015**, *115*, 8449–8503.
- (7) Baldo, M.; Thompson, M. E.; Forrest, S. *Nature* **2000**, *403*, 750–3.
- (8) Turro, N.; Scaiano, J.; Ramamurthy, V., *Modern Molecular Photochemistry of Organic Molecules*; University Science Books: 1991.
- (9) Baldo, M.; O'Brien, D.; You, Y.; Shoustikov, A.; Sibley, S.; Thompson, M. E.; Forrest, S. *Nature* **1998**, *395*, 151–154.
- (10) Furno, M.; Meerheim, R.; Thomschke, M.; Hofmann, S.; Lüssem, B.; Leo, K. *Proceedings of SPIE* **2010**, *7617*, ed. by Streubel, K. P.; Jeon, H.; Tu, L.-W.; Linder, N., 761716–761716–12.
- (11) Furno, M.; Meerheim, R.; Hofmann, S.; Lüssem, B.; Leo, K. *Physical Review B* **2012**, *85*, 115205.
- (12) Pope, M.; Swenberg, C., *Electronic Processes in Organic Crystals and Polymers*, 2nd; Oxford University Press: 1999.
- (13) Mark, P.; Helfrich, W. *Journal of Applied Physics* **1962**, *33*, 205.
- (14) Lampert, M. A. *Reports on Progress in Physics* **2002**, *27*, 329–367.
- (15) Hershey, K. W.; Holmes, R. J. *Journal of Applied Physics* **2016**, *120*, 195501.

- (16) Inoue, M.; Serevičius, T.; Nakanotani, H.; Yoshida, K.; Matsushima, T.; Juršėnas, S.; Adachi, C. *Chemical Physics Letters* **2016**, *644*, 62–67.
- (17) Forrest, S.; Bradley, D.; Thompson, M. E. *Advanced Materials* **2003**, *15*, 1043–1048.
- (18) Smith, T.; Guild, J. *Transactions of the Optical Society* **1931**, *33*, 73–134.
- (19) Wright, W. D. *Transactions of the Optical Society* **1929**, *30*, 141–164.
- (20) Guild, J. *Philosophical Transactions of the Royal Society A: Mathematical, Physical and Engineering Sciences* **1932**, *230*, 149–187.
- (21) Bohn, D. Google updates Pixel 2 XL with new ‘saturated’ color display option and other bug fixes - The Verge., 2017.
- (22) Tang, C. W.; VanSlyke, S. *Applied Physics Letters* **1987**.
- (23) Venkataraman, K., *The chemistry of synthetic dyes*; Elsevier, 2012: 1971.
- (24) Schäfer, F. P.; Drexhage, K. H. *Topics in Applied Physics* **1977**.
- (25) Dresner, J. *RCA REVIEW* **1969**.
- (26) Williams, D. F.; Schadt, M. *Proceedings of the IEEE* **1970**, *58*, 476.
- (27) Helfrich, W.; Schneider, W. G. *Physical Review Letters* **1965**, *14*, 229–231.
- (28) Tang, C. W.; Vanslyke, S. a.; Chen, C. H. *Journal of Applied Physics* **1989**, *65*, 3610–3616.
- (29) Reineke, S.; Walzer, K.; Leo, K. *Physical Review B* **2007**, *75*, 125328.
- (30) O’Brien, D. F.; Baldo, M.; Thompson, M. E.; Forrest, S. *Applied Physics Letters* **1999**, *74*, 442.
- (31) Adachi, C.; Baldo, M.; Forrest, S.; Thompson, M. E. *Applied Physics Letters* **2000**, *77*, 904.
- (32) Su, S. J.; Gonmori, E.; Sasabe, H.; Kido, J. *Advanced Materials* **2008**, *20*, 4189–4194.
- (33) Erickson, N. C.; Holmes, R. J. *Applied Physics Letters* **2010**, *97*, 083308.
- (34) Scholz, S.; Walzer, K.; Leo, K. *Advanced Functional Materials* **2008**, *18*, 2541–2547.
- (35) Uoyama, H.; Goushi, K.; Shizu, K.; Nomura, H.; Adachi, C. *Nature* **2012**, *492*, 234–8.
- (36) Adachi, C.; Baldo, M. A.; Thompson, M. E.; Forrest, S. R. *Journal of Applied Physics* **2001**, *90*, 5048–5051.
- (37) Zhang, Q.; Komino, T.; Huang, S.; Matsunami, S.; Goushi, K.; Adachi, C. *Advanced Functional Materials* **2012**, *22*, 2327–2336.
- (38) Zhang, Q.; Li, B.; Huang, S.; Nomura, H.; Tanaka, H.; Adachi, C. *Nature Photonics* **2014**, *8*, 1–7.

- (39) Menke, S. M.; Holmes, R. J. *The Journal of Physical Chemistry C* **2016**, *120*, 8502–8508.
- (40) Li, J.; Nakagawa, T.; Macdonald, J.; Zhang, Q.; Nomura, H.; Miyazaki, H.; Adachi, C. *Advanced Materials* **2013**, *25*, 3319–3323.
- (41) Wang, H.; Meng, L.; Shen, X.; Wei, X.; Zheng, X.; Lv, X.; Yi, Y.; Wang, Y.; Wang, P. *Advanced Materials* **2015**, n/a–n/a.
- (42) Liu, X.-K.; Chen, Z.; Zheng, C.-J.; Chen, M.; Liu, W.; Zhang, X.-H.; Lee, C.-S. *Advanced Materials* **2015**, n/a–n/a.
- (43) Kim, K.-H.; Moon, C.-K.; Sun, J. W.; Sim, B.; Kim, J.-J. *Advanced Optical Materials* **2015**, n/a–n/a.
- (44) Jankus, V.; Data, P.; Graves, D.; McGuinness, C.; Santos, J.; Bryce, M. R.; Dias, F. B.; Monkman, A. P. *Advanced Functional Materials* **2014**, n/a–n/a.
- (45) Lavie-Cambot, A.; Cantuel, M.; Leydet, Y.; Jonusauskas, G.; Bassani, D. M.; McClenaghan, N. D. *Coordination Chemistry Reviews* **2008**, *252*, 2572–2584.
- (46) Endo, A.; Ogasawara, M.; Takahashi, A.; Yokoyama, D.; Kato, Y.; Adachi, C. *Advanced materials (Deerfield Beach, Fla.)* **2009**, *21*, 4802–4806.
- (47) Yersin, H.; Leitl, M. J.; Czerwieniec, R. **2014**, *9183*, 91830N.
- (48) Nasu, K.; Nakagawa, T.; Nomura, H.; Lin, C.-J.; Cheng, C.-H.; Tseng, M.-R.; Yasuda, T.; Adachi, C. *Chemical communications (Cambridge, England)* **2013**, *49*, 10385–7.
- (49) Zhang, Q.; Li, J.; Shizu, K.; Huang, S.; Hirata, S.; Miyazaki, H.; Adachi, C. **2012**, 0–3.
- (50) Hofbeck, T.; Monkowius, U.; Yersin, H. *Journal of the American Chemical Society* **2015**, *137*, 399–404.
- (51) Linfoot, C. L.; Leitl, M. J.; Richardson, P.; Rausch, A. F.; Chepelin, O.; White, F. J.; Yersin, H.; Robertson, N. *Inorganic chemistry* **2014**, DOI: 10.1021/ic500889s.
- (52) Reineke, S. *Nature Photonics* **2014**, *8*, 269–270.
- (53) Méhes, G.; Goushi, K.; Potscavage, W. J.; Adachi, C. *Organic Electronics: physics, materials, applications* **2014**, *15*, 2027–2037.
- (54) Cho, Y. J.; Yook, K. S.; Lee, J. Y. *Advanced Materials* **2014**, *26*, 4050–4055.
- (55) Erickson, N. C.; Holmes, R. J. *Advanced Functional Materials* **2014**, *24*, 6074–6080.
- (56) Song, D.; Zhao, S.; Aziz, H. *Advanced Functional Materials* **2011**, *21*, 2311–2317.
- (57) Wehrmeister, S.; Jäger, L.; Wehlus, T.; Rausch, A. F.; Reusch, T. C. G.; Schmidt, T. D.; Brütting, W. *Physical Review Applied* **2015**, *3*, 1–10.

- (58) Son, K. S.; Yahiro, M.; Imai, T.; Yoshizaki, H.; Nishide, J.; Sasabe, H.; Adachi, C. *Japanese Journal of Applied Physics* **2008**, *47*, 7363–7365.
- (59) Murawski, C.; Leo, K.; Gather, M. C. *Advanced materials (Deerfield Beach, Fla.)* **2013**, *25*, 6801–27.
- (60) Giebink, N. C.; Forrest, S. *Physical Review B* **2008**, *77*, 235215.
- (61) Song, D.; Zhao, S.; Luo, Y.; Aziz, H. *Applied Physics Letters* **2010**, *97*, 243304.
- (62) Xiang, C.; Fu, X.; Wei, W.; Liu, R.; Zhang, Y.; Balema, V.; Nelson, B.; So, F. *Advanced Functional Materials* **2016**, *26*, 1463–1469.
- (63) Coehoorn, R.; Van Eersel, H.; Bobbert, P. A.; Janssen, R. A. J. *Advanced Functional Materials* **2015**, *25*, 2024–2037.
- (64) Reineke, S.; Schwartz, G.; Walzer, K.; Falke, M.; Leo, K. *Applied Physics Letters* **2009**, *94*, 2007–2010.
- (65) Mężyk, J.; Kalinowski, J.; Meinardi, F.; Tubino, R. *Applied Physics Letters* **2005**, *86*, 111916.
- (66) Baldo, M.; Adachi, C.; Forrest, S. *Physical Review B* **2000**, *62*, 10967–10977.
- (67) Köhler, a.; Bässler, H. *Materials Science and Engineering: R: Reports* **2009**, *66*, 71–109.
- (68) Erickson, N. C.; Holmes, R. J. *Advanced Functional Materials* **2013**, *23*, 5190–5198.
- (69) Giebink, N. C.; D’Andrade, B. W.; Weaver, M. S.; MacKenzie, P. B.; Brown, J. J.; Thompson, M. E.; Forrest, S. *Journal of Applied Physics* **2008**, *103*, DOI: 10.1063/1.2884530.
- (70) Coburn, C.; Forrest, S. *Physical Review Applied* **2017**, *7*, 041002.
- (71) Lee, J.; Jeong, C.; Batagoda, T.; Coburn, C.; Thompson, M. E.; Forrest, S. *Nature Communications* **2017**, *8*, 15566.
- (72) Baldo, M.; Holmes, R. J.; Forrest, S. *Physical Review B* **2002**, *66*, 35321.
- (73) Holmes, R. J. *Nature Nanotechnology* **2007**, *2*, 7–8.
- (74) Takenobu, T.; Bisri, S.; Takahashi, T.; Yahiro, M.; Adachi, C.; Iwasa, Y. *Physical Review Letters* **2008**, *100*, 066601.
- (75) Samuel, I. D. W.; Namdas, E. B.; Turnbull, G. a. *Nature Photonics* **2009**, *3*, 546–549.
- (76) Kasemann, D.; Brückner, R.; Fröb, H.; Leo, K. *Physical Review B* **2011**, *84*, 115208.
- (77) Murawski, C.; Liehm, P.; Leo, K.; Gather, M. C. *Advanced Functional Materials* **2014**, *24*, 1117–1124.
- (78) Soofi, H.; Saeidi, S. **2017**, 1–8.

- (79) Chopra, N.; Swensen, J. S.; Polikarpov, E.; Cosimescu, L.; So, F.; Padmaperuma, A. B. *Applied Physics Letters* **2010**, *97*, 95–98.
- (80) Reineke, S.; Schwartz, G.; Walzer, K.; Leo, K. *Applied Physics Letters* **2007**, *91*, 1–4.
- (81) Lee, J. I. J. Y. J.-I. J.; Lee, J. I. J. Y. J.-I. J.; Lee, J. I. J. Y. J.-I. J.; Chu, H. Y. *Applied Physics Letters* **2009**, *94*, 193305.
- (82) Zang, F. X.; Sum, T. C.; Huan, a. C. H.; Li, T. L.; Li, W. L.; Zhu, F. *Applied Physics Letters* **2008**, *93*, 023309.
- (83) Giebink, N. C.; Sun, Y.; Forrest, S. *Organic Electronics: physics, materials, applications* **2006**, *7*, 375–386.
- (84) Giebink, N. C.; D'Andrade, B. W.; Weaver, M. S.; Brown, J. J.; Forrest, S. *Journal of Applied Physics* **2009**, *105*, 124514.
- (85) Hershey, K. W.; Suddard-Bangsund, J.; Qian, G.; Holmes, R. J. *Applied Physics Letters* **2017**, *111*, 113301.
- (86) Bangsund, J. S.; Hershey, K. W.; Holmes, R. J. *ACS Applied Materials & Interfaces* **2018**, acsami.7b16643.
- (87) Coburn, C.; Lee, J.; Forrest, S. *Advanced Optical Materials* **2016**, *4*, 889–895.
- (88) Reineke, S.; Lindner, F.; Huang, Q.; Schwartz, G.; Walzer, K.; Leo, K. *Physica Status Solidi (B) Basic Research* **2008**, *245*, 804–809.
- (89) Erickson, N. C.; Holmes, R. J. *Journal of Applied Physics* **2011**, *110*, 084515.
- (90) Féry, C.; Racine, B.; Vaufrey, D.; Doyeux, H.; Cinà, S. *Applied Physics Letters* **2005**, *87*, 213502.
- (91) Giebink, N. *Optics InfoBase Conference Papers* **2017**, Part F72-S, 2017.
- (92) Kolosov, D.; English, D. S.; Bulovic, V.; Barbara, P. F.; Forrest, S. R.; Thompson, M. E. *Journal of Applied Physics* **2001**, *90*, 3242–3247.
- (93) Wang, W.; Lim, S. F.; Chua, S. J. *Journal of Applied Physics* **2002**, *91*, 5712–5715.
- (94) Burrows, P. E.; Bulovic, V.; Forrest, S.; Sapochak, L. S.; McCarty, D. M.; Thompson, M. E. *Applied Physics Letters* **1994**, *65*, 2922–2924.
- (95) Aziz, H.; Popovic, Z. D. *Chemistry of Materials* **2004**, *16*, 4522–4532.
- (96) Popovic, Z. D.; Aziz, H. *IEEE Journal on Selected Topics in Quantum Electronics* **2002**, *8*, 362–371.
- (97) Liew, Y.-f.; Aziz, H.; Hu, N.-x.; Chan, H. S.-o.; Xu, G.; Popovic, Z.; Liew, Y.-f.; Chan, H. S.-o. **2006**, *2650*, 1998–2001.

- (98) Melpignano, P.; Baron-Toaldo, A.; Biondo, V.; Priante, S.; Zamboni, R.; Murgia, M.; Caria, S.; Gregoratti, L.; Barinov, A.; Kiskinova, M. *Applied Physics Letters* **2005**, *86*, 1–4.
- (99) Liao, L. S.; He, J.; Zhou, X.; Lu, M.; Xiong, Z. H.; Deng, Z. B.; Hou, X. Y.; Lee, S. T. **2007**, *2386*, 1–6.
- (100) Shin, H. J.; Song, H. J.; Lee, J.; Yoon, H. J.; Chung, J.; Lee, J. C. *Journal of Applied Physics* **2006**, *100*, 1–5.
- (101) Scott, J. C.; Kaufman, J. H.; Brock, P. J.; DiPietro, R.; Salem, J.; Goitia, J. A. *Journal of Applied Physics* **1996**, *79*, 2745–2751.
- (102) Cumpston, B. H. *Journal of Applied Physics* **1997**, *81*, 3716–3720.
- (103) Zhang, Y.; Aziz, H. *ACS Applied Materials and Interfaces* **2016**, *8*, 14088–14095.
- (104) So, F.; Kondakov, D. *Advanced Materials* **2010**, *22*, 3762–3777.
- (105) Zhang, Y.; Lee, J.; Forrest, S. *Nature Communications* **2014**, *5*, 1–7.
- (106) Wu, Z.; Sun, N.; Zhu, L.; Sun, H.; Wang, J.; Yang, D.; Qiao, X.; Chen, J.; Alshehri, S. M.; Ahamed, T.; Ma, D. *ACS Applied Materials and Interfaces* **2016**, *8*, 3150–3159.
- (107) Chin, B. D.; Suh, M. C.; Kim, M. H.; Lee, S. T.; Kim, H. D.; Chung, H. K. *Applied Physics Letters* **2005**, *86*, 1–3.
- (108) Lee, J. Y. **2006**, 1103–1105.
- (109) Chwang, A. B.; Kwong, R. C.; Brown, J. J. *Applied Physics Letters* **2002**, *80*, 725–727.
- (110) Han, T. H.; Kim, Y. H.; Kim, M. H.; Song, W.; Lee, T. W. *ACS Applied Materials and Interfaces* **2016**, *8*, 6152–6163.
- (111) Lee, J. H.; Wu, C. I.; Liu, S. W.; Huang, C. A.; Chang, Y. *Applied Physics Letters* **2005**, *86*, 1–3.
- (112) Brown, C. T.; Kondakov, D. *Journal of the Society for Information Display* **2004**, *12*, 323–327.
- (113) Choong, V. E.; Shen, J.; Curless, J.; Shi, S.; Yang, J.; So, F. *Journal of Physics D: Applied Physics* **2000**, *33*, 760–763.
- (114) Liu, S. W.; Huang, C. A.; Lee, J. H.; Yang, K. H.; Chen, C. C.; Chang, Y. *Thin Solid Films* **2004**, *453-454*, 312–315.
- (115) Shen, Y.; Giebink, N. C. *Physical Review Applied* **2015**, *4*, 1–12.
- (116) Wang, Q.; Aziz, H. *ACS Applied Materials and Interfaces* **2013**, *5*, 8733–8739.
- (117) Aziz, H. *Science* **1999**, *283*, 1900–1902.

- (118) Kondakov, D. Y.; Sandifer, J. R.; Tang, C. W.; Young, R. H. *Journal of Applied Physics* **2003**, *93*, 1108–1119.
- (119) Matsumura, M.; Ito, A.; Miyamae, Y. *Applied Physics Letters* **1999**, *75*, 1042–1044.
- (120) Kondakov, D. Y.; Nichols, W. F.; Lenhart, W. C. *SID Symposium Digest of Technical Papers* **2007**, *38*, 1494–1496.
- (121) Kondakov, D. Y. *Journal of Applied Physics* **2008**, *104*, DOI: 10.1063/1.3006890.
- (122) Kondakov, D. Y.; Lenhart, W. C.; Nichols, W. F. *Journal of Applied Physics* **2007**, *101*, 024512.
- (123) Meerheim, R.; Walzer, K.; Pfeiffer, M.; Leo, K. *Applied Physics Letters* **2006**, *89*, 061111.
- (124) Fry, C.; Racine, B.; Vaufrey, D.; Doyeux, H.; Ciñ, S. *Applied Physics Letters* **2005**, *87*, 1–3.
- (125) Seifert, R.; Rabelo De Moraes, I.; Scholz, S.; Gather, M. C.; Lüssem, B.; Leo, K. *Organic Electronics: physics, materials, applications* **2013**, *14*, 115–123.
- (126) Moraes, I. R. D.; Scholz, S.; Lüssem, B.; Leo, K. *Organic Electronics* **2011**, *12*, 341–347.
- (127) De Moraes, I. R.; Scholz, S.; Lüssem, B.; Leo, K. *Applied Physics Letters* **2011**, *99*, 053302.
- (128) Sivasubramaniam, V.; Brodkorb, F.; Hanning, S.; Loebel, H. P.; Elsbergen, V.; Boerner, H.; Scherf, U.; Kreyenschmidt, M. *Central European Journal of Chemistry* **2009**, *7*, 836–845.
- (129) Peng, C.; Salehi, A.; Chen, Y.; Danz, M.; Liaptsis, G.; So, F. *ACS Applied Materials & Interfaces* **2017**, acsami.7b13537.
- (130) Wang, Q.; Aziz, H. *Organic Electronics* **2015**, *26*, 464–470.
- (131) Wang, Q.; Sun, B.; Aziz, H. *Advanced Functional Materials* **2014**, *24*, 2975–2985.
- (132) Yu, H.; Zhang, Y.; Cho, Y. J.; Aziz, H. *ACS Applied Materials & Interfaces* **2017**, acsami.7b01432.
- (133) Wang, Q.; Luo, Y.; Aziz, H. *Applied Physics Letters* **2010**, *97*, 1–4.
- (134) Tsutsui, T.; Yang, M.-j.; Yahiro, M.; Nakamura, K.; Watanabe, T.; Tsuji, T.; Fukuda, Y.; Wakimoto, T.; Miyaguti, S. *Jpn. J. Appl. Phys. Part 2*: **1999**, *38*, L1502–L1504.
- (135) Holmes, R. J.; Forrest, S.; Tung, Y.-J.; Kwong, R. C.; Brown, J. J.; Garon, S.; Thompson, M. E. *Applied Physics Letters* **2003**, *82*, 2422.
- (136) Kalinowski, J.; Stampor, W.; Męzyk, J.; Cocchi, M.; Virgili, D.; Fattori, V.; Di Marco, P. *Physical Review B* **2002**, *66*, 235321.
- (137) Zhang, B.; Tan, G.; Lam, C. S.; Yao, B.; Ho, C. L.; Liu, L.; Xie, Z.; Wong, W. Y.; Ding, J.; Wang, L. *Advanced Materials* **2012**, *24*, 1873–1877.

- (138) Tsuboi, T.; Murayama, H.; Penzkofer, A. *Thin Solid Films* **2006**, *499*, 306–312.
- (139) Adachi, C.; Kwong, R.; Forrest, S. *Organic Electronics* **2001**, *2*, 37–43.
- (140) Kawamura, Y.; Brooks, J.; Brown, J. J.; Sasabe, H.; Adachi, C. *Physical Review Letters* **2006**, *96*, 11–14.
- (141) Kawamura, Y.; Goushi, K.; Brooks, J.; Brown, J. J.; Sasabe, H.; Adachi, C. *Applied Physics Letters* **2005**, *86*, 1–3.
- (142) Rihani, A.; Hassine, L.; Fave, J.-L.; Bouchriha, H. *Organic Electronics* **2006**, *7*, 1–7.
- (143) Hassine, L.; Bouchriha, H.; Roussel, J.; Fave, J. L. *Applied Physics Letters* **2001**, *78*, 1053–1055.
- (144) Hassine, L.; Bouchriha, H.; Roussel, J.; Fave, J. L. *Journal of Applied Physics* **2002**, *91*, 5170–5175.
- (145) Ruhstaller, B.; Beierlein, T.; Riel, H.; Karg, S.; Scott, J.; Riess, W. *IEEE Journal of Selected Topics in Quantum Electronics* **2003**, *9*, 723–731.
- (146) Ruhstaller, B.; Carter, S. a.; Barth, S.; Riel, H.; Riess, W.; Scott, J. C. *Journal of Applied Physics* **2001**, *89*, 4575–4586.
- (147) Pinner, D. J.; Friend, R. H.; Tessler, N. *Journal of Applied Physics* **1999**, *86*, 5116–5130.
- (148) Blom, P. W. M.; De Jong, M. J. M.; Vleggaar, J. J. M. *Applied Physics Letters* **1996**, *68*, 3308–3310.
- (149) Wei, B.; Furukawa, K.; Amagai, J.; Ichikawa, M.; Koyama, T.; Taniguchi, Y. *Semiconductor Science and Technology* **2004**, *19*, L56–L59.
- (150) Liu, F.; Ruden, P. P.; Campbell, I. H.; Smith, D. L. *Applied Physics Letters* **2012**, *101*, 023501.
- (151) Rothberg, L. J.; Lovinger, A. J. *Journal of Materials Research* **1996**, *11*, 3174–3187.
- (152) Staroske, W.; Pfeiffer, M.; Leo, K.; Hoffmann, M. *Physical Review Letters* **2007**, *98*, 197402.
- (153) Parshin, M. A.; Ollevier, J.; Van der Auweraer, M. In, ed. by Heremans, P. L.; Muccini, M.; Meulenkamp, E. A., 2006; Vol. 6192, 61922A.
- (154) Ingram, G. L.; Zhao, Y.-B.; Lu, Z.-H. *Journal of Applied Physics* **2017**, *122*, DOI: 10.1063/1.5003011.
- (155) Wang, Q.; Aziz, H. *Organic Electronics* **2011**, *12*, 1571–1575.
- (156) Popovic, Z. D.; Aziz, H.; Hu, N. X.; Ioannidis, A.; Dos Anjos, P. N. M. *Journal of Applied Physics* **2001**, *89*, 4673–4675.
- (157) Winter, S.; Reineke, S.; Walzer, K.; Leo, K. *Proceedings of SPIE* **2008**, *6999*, 69992N–69992N–8.
- (158) Bangsund, J. S.; Hershey, K. W. **2018**.

- (159) Pettersson, L. A. A.; Roman, L. S.; Inganäs, O. *Journal of Applied Physics* **1999**, *86*, 487.
- (160) Han, C.; Zhu, L.; Li, J.; Zhao, F.; Zhang, Z.; Xu, H.; Deng, Z.; Ma, D.; Yan, P. *Advanced Materials* **2014**, *26*, 7070–7077.
- (161) Price, J. S.; Giebink, N. C. *Applied Physics Letters* **2015**, *106*, 263302.
- (162) Adachi, C.; Kwong, R. C.; Djurovich, P.; Adamovich, V.; Baldo, M.; Thompson, M. E.; Forrest, S. *Applied Physics Letters* **2001**, *79*, 2082.
- (163) Watanabe, S.; Ide, N.; Kido, J. *Japanese Journal of Applied Physics* **2007**, *46*, 1186–1188.
- (164) Adamovich, V. I.; Cordero, S. R.; Djurovich, P. I.; Tamayo, A.; Thompson, M. E.; D’Andrade, B. W.; Forrest, S. *Organic Electronics* **2003**, *4*, 77–87.
- (165) Xu, F.; Hershey, K. W.; Holmes, R. J.; Hoye, T. R. *Journal of the American Chemical Society* **2016**, *138*, 12739–12742.
- (166) Lee, J.; Chen, H.-F.; Batagoda, T.; Coburn, C.; Djurovich, P. I.; Thompson, M. E.; Forrest, S. *Nature Materials* **2015**, *15*, 92–98.
- (167) Yi, S.; Kim, J. H.; Cho, Y. J.; Lee, J.; Choi, T. S.; Cho, D. W.; Pac, C.; Han, W. S.; Son, H. J.; Kang, S. O. *Inorganic Chemistry* **2016**, *55*, 3324–3331.
- (168) Kim, S.-K.; Yang, B.; Ma, Y.; Lee, J.-H.; Park, J.-W. *Journal of Materials Chemistry* **2008**, *18*, 3376.
- (169) Schmidbauer, S.; Hohenleutner, A.; König, B. *Beilstein Journal of Organic Chemistry* **2013**, *9*, 2088–2096.
- (170) Wang, Q.; Williams, G.; Aziz, H. *Organic Electronics: physics, materials, applications* **2012**, *13*, 2075–2082.
- (171) Zhang, Y.; Aziz, H. *ACS Applied Materials and Interfaces* **2017**, *9*, 636–643.
- (172) Chan, C.-Y.; Cui, L.-S.; Kim, J. U.; Nakanotani, H.; Adachi, C. *Advanced Functional Materials* **2018**, *1706023*, 1706023.
- (173) Tang, X.; Bai, Q.; Shan, T.; Li, J.; Gao, Y.; Liu, F.; Liu, H.; Peng, Q.; Yang, B.; Li, F.; Lu, P. *Advanced Functional Materials* **2018**, *1705813*, 1705813.
- (174) Tokito, S.; Iijima, T.; Suzuri, Y.; Kita, H.; Tsuzuki, T.; Sato, F. *Applied Physics Letters* **2003**, *83*, 569–571.
- (175) Goushi, K.; Kwong, R.; Brown, J. J.; Sasabe, H.; Adachi, C. *Journal of Applied Physics* **2004**, *95*, 7798–7802.
- (176) Zhang, Y.; Forrest, S. *Physical Review B - Condensed Matter and Materials Physics* **2011**, *84*, 1–4.

## BIBLIOGRAPHY

- (177) Schueppel, R.; Uhrich, C.; Pfeiffer, M.; Leo, K.; Brier, E.; Reinold, E.; Baeuerle, P. *ChemPhysChem* **2007**, *8*, 1497–1503.
- (178) Padhye, M. R.; McGlynn, S. P.; Kasha, M. *The Journal of Chemical Physics* **1956**, *24*, 588–594.
- (179) Reineke, S.; Baldo, M. *Scientific Reports* **2014**, *4*, 3797.

# Appendices

## Appendix A

### List of Publications

- Hershey, K. W.; Holmes, R. J. *Journal of Applied Physics* **2016**, *120*, 195501
- Xu, F. et al. *Journal of the American Chemical Society* **2016**, *138*, 12739–12742
- Hershey, K. W. et al. *Applied Physics Letters* **2017**, *111*, 113301
- Bangsund, J. S. et al. *ACS Applied Materials & Interfaces* **2018**, acsami.7b16643
- Bangsund, J. S.; Hershey, K. W. **2018**

## Appendix B

# Measuring Triplet Energies

As discussed in Chapter 1.2, singlet excitons are typically responsible for molecular emission because the triplet state is quantum mechanically forbidden in the first order approximation.<sup>8</sup> Emission from the triplet state is allowed with the addition of spin-orbit coupling.<sup>9</sup> For applications including OLEDs, solar cells, and organic lasers, spectroscopic characterization of the triplet state is needed, often for molecules where the spin-orbit coupling is weak.<sup>174–177</sup>

Most measurements of the triplet energy are conducted via optical pumping.<sup>8,135,175,178</sup> However, triplet populations are not generated optically in most materials.<sup>8</sup> In order for a triplet population to be established,  $k_{ISC}$  must be greater than 0. Additionally, the radiative rate,  $k_r$  must be at least competitive with  $k_{nr}$ . Since the triplet state is quantum mechanically disallowed without spin-orbit coupling, the radiative rate is typically low compared to the singlet, on the order of  $10^6 s^{-1}$ . At room temperature,  $k_{nr}$  is often seen to be  $10^2 - 10^6 s^{-1}$ .<sup>179</sup> In order to reduce  $k_{nr}$ , cryogenic temperatures are often employed, though room-temperature techniques do exist.<sup>179</sup>

In our lab, I have utilized Janis liquid helium cryogenic optical system to measure triplets. This takes the temperature to 10K and severely reduces  $k_{nr}$ . Samples are prepared on Silicon to take advantage of the strong thermal conductivity compared to glass. If the total emission is collected, the singlet still is far more emissive than the triplet. However, the difference in their lifetimes can be utilized to separate them. Using a pulsed nitrogen laser, the

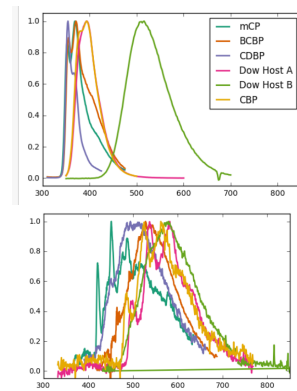


**Figure B.1:** Fluorescence (a) and Phosphorescence (b) spectra for several materials obtained from this system.

exciton population is excited. The singlet population decays quickly, within a few nanoseconds. However, the triplet lifetime at low temperatures is much longer. A triggered spectrometer can be used to measure the delayed phosphorescence, and thus measure the triplet emission only. I have done this with a Princeton Instruments Fergie spectrometer, with a delay of 5ms from the laser pulse.

This system has been used to measure triplet spectra for a variety of materials, shown in Figure B.1. To extract triplet energies, the short wavelength turn on of the triplet spectra can be used. This is the highest energy, which seems counter intuitive, but the observed spectra is a decay from  $T_1$  to vibrational states of the ground state,  $S_0$ . The triplet energy is defined as the difference between the lowest vibronic of  $T_1$  to the lowest vibronic of  $S_0$ , which is the highest energy transition observed in the spectra. These spectra show different behavior for sharpness of the leading edge, but a 20% of the maximum intensity is chosen as the threshold for defining the triplet energy.

## Appendix C

# Single Carrier Device Modeling

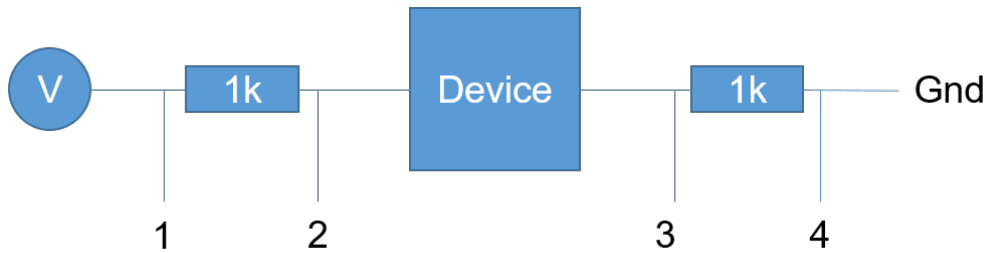


**Figure C.1:** Circuit used for measuring polaron density. Voltage readings are taken at 1-4 over a  $1M\Omega$  termination.

When trying to understand device behavior, it is often important to investigate single carrier devices to understand one charge species at a time or isolate dynamic processes. An example of this is measurement of the triplet-polaron quenching rate constant, demonstrated in Chapter 3.5. Determination of the polaron density is often critical in order to quantify these results. This is often done by assuming the device is operating within the space charge limit, in which charges have overcome injection barrier limits and transport through the bulk of the material is the limiting process.<sup>29,55</sup> In the space-charge limit, current is most simply described using the Mott-Gurney Law, and can be modified to include various trap states to adapt to different semiconductor properties.<sup>12</sup> However, space-charge limited current is really only accurate for device behavior at high voltages for thick devices. Often, organic layer stacks of interest feature relatively thin layers, and voltages close to the injection limits. It can be difficult to identify when a device is operating in the space-charge limit.

In order to reduce some of the uncertainty associated with determining polaron density, a differential current measurement can be conducted. For a single carrier device, only one type of carrier is injected. As charge is being injected into the device and a steady-state polaron density is being achieved, the current on the side of the device where charges are injected should be greater than on the other side. This can be seen

in Figure C.1, where for a hole only device, the current over  $R_{12}$  should be greater than the current over  $R_{34}$ . All of these signals can be measured using an oscilloscope. Once steady-state is achieved, the currents should be equal. The polaron population injected into the device can be calculated using the following equation

$$N_{pol} = \int J_{1-2} - J_{3-4} dt \quad (C.1)$$

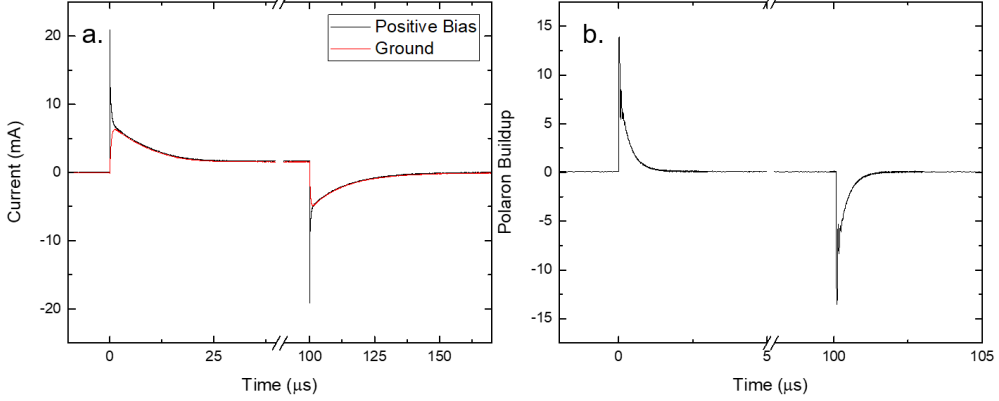


**Figure C.2:** Differential currents for a hole only device. Currents on either side of the device are shown in a. while the difference between them is shown in b.

where  $J$  is the current and 1-4 are labeled in Figure C.1. When voltage is removed from the device, the currents will diverge and the polaron density will be drained from the device. This is demonstrated in Figure C.2, with the currents on either side of the device and the differential current shown in C.2a and C.2b, respectively. Notice the positive differential when current is applied and polarons enter the device, and negative when they are removed.

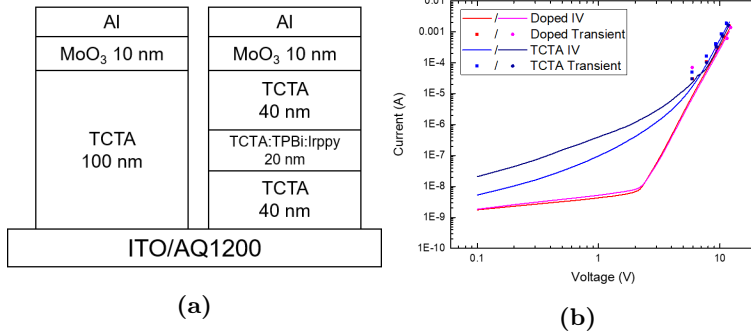


**Figure C.3:** a. Hole only device architectures. b. Current Voltage characteristics for the devices shown in a. Steady-state sweeps as well as current measured from the differential technique are shown.

While this technique is able to accurately tell the injected polaron population, the distribution of that population is still unknown. This technique does provide the advantage that with the total polaron population known, the current or voltage dependence of the population can be compared to different models to further validate the operational regime. Then, a model can be applied to show the spatial dependence of charge.<sup>12-14</sup> This technique has the advantage that only the spatial dependence is needed, rather than

having to estimate the total charge population, and is more accurate than previous methods relying on solely modeling.

Ideally the polaron population can be restricted to a small area of the device to minimize the extent of the spatial distribution. To achieve this, the devices shown in Figure C.3a were investigated. The region of interest is the mixed doped layer in the right hand device. This doped region should show a greater ability to facilitate trapped charge and show a larger polaron population. The current-voltage profile of these devices is shown in Figure C.3b where the doped devices show a stronger diode behavior. The currents obtained from the displacement current measurements show agreement with the steady state current.

The polaron population as a function of current is shown for these devices in Figure C.4. Unfortunately, polaron populations for both devices are almost identical and the hypothesis of increased trapping in the doped region is not correct. This means that charges are not confined and there is likely a wide distribution of the polaron density. Despite these drawbacks, the polaron population is still obtained and can be compared to space-charge limited current models.

## C.1 Future Work

This technique is useful for a variety of techniques where polaron population needs to be known precisely. One ready application of this technique is for triplet-polaron quenching measurements. As discussed in Chapter 3.5, measurement of  $k_{TP}$  relies on optically pumping a single carrier device under an applied current. To accurately determine the constant, the polaron density must be known precisely. The differential current technique would be useful for comparing different materials and their values of  $k_{TP}$ . Another application with similar motivations would be the optical degradation of single carrier devices.

Differential current analysis of single carrier devices provides a straight forward way of determining the polaron population within a single carrier device. While the spatial distribution of the polaron population may not be known, this can be easily modeled with the current dependence of the polaron population available for validation of the model. Though so far unused in a relevant application, this technique allows more sophisticated comparison of devices when matched polaron population is important.

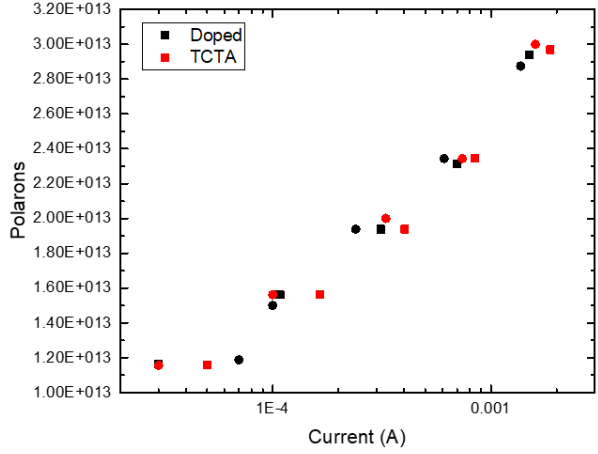


**Figure C.4:** Polaron population as a function of current for the devices in Figure C.3a

# Appendix D

## Out-Coupling Code

### D.1 Transfer Matrix Model

The following is code to implement a transfer matrix model for calculating absorption and electric field profile within a thin film stack, as described by Pettersson.<sup>159</sup>

transfer.m

```
1 function transfer
2
3 global q
4 global d
5 global n
6
7 %%%%%%%%%%%%%%%%%%%%%%%%%%%%%%%%%%%%%%
8 %
9 % Model Setup
10 %
11 %%%%%%%%%%%%%%%%%%%%%%%%%%%%%%%%%%%%%%
12
13 % Layers. Must match names in lookup table
14 layers = {'SiO2' 'ITOorizon' 'PEDOT' 'P3HTPCBBlendDCB' 'Ca' 'Al'};
15
16
17
18 % layer thicknesses. First value is unused
19 % but placeholder so indices match
20 d = [
21     0
```

```

22    110
23    35
24    220
25    7
26    200
27    ];
28
29 % angle of incidence
30 phi_0 = 0;
31
32 %%%%%%
33 %
34 % Test Parameters
35 %
36 %%%%%%
37
38 % resolution in nm
39 res = 1;
40 %% note: You should try to make this an even division of the layer
41 %% thicknesses. If not, the first output will always be at the left edge
42 %% of the layer,sampling at each res step. This could result in an uneven
43 %% spacing between the last sample of j and the first of j+1.
44
45 % Wavelengths to test
46 waves = [400];
47
48
49 %%%%%%
50 %
51 % Generation
52 %
53 %%%%%%
54
55 %% Load in index of refraction for each material and each wavelength
56 ntable = zeros(size(layers,2),size(waves,2));
57 for index = 1:size(layers,2)
58     ntable(index,:) = LoadRefrIndex(layers{index},waves);
59 end
60
61
62

```

```

63 % calculating array size for preallocation
64 numSteps=0;
65 x = [];
66 depth = 0;
67 for l = 1:length(d)-1
68     numSteps=numSteps+(ceil(d(l+1)/res)-1)*res+1;
69     steps = 0:res:(ceil(d(l+1)/res)-1)*res;
70     x = [x (steps+depth)];
71     depth = depth + d(l+1);
72 end
73 specs = zeros(numSteps, size(waves,2));
74
75 % hard work begins
76 for iter = 1:size(waves,2)
77     lambda = waves(iter);
78     n=ntable(:,iter);
79     q = (n.^2-n(1)^2*(sin(phi_0))^2).^(1/2);
80     % ! ! ! ! ! ! ! ! ! ! ! ! !
81     % T_glass=abs(4*1*n(1)/(1+n(1)).^2);
82     R_glass=abs((1-n(1))/(1+n(1))).^2;
83     S=scattering(1,lambda);
84     R=abs(S(2,1)/S(1,1))^2; %JAP Vol 86 p.487 Eq 9 Power Reflection from layers other than
85     % substrate
86     T=abs(2/(1+n(1)))/sqrt(1-R_glass*R); %Transmission of field through glass substrate
87     Griffiths Electrodynamics 9.85 + multiple reflection geometric series
88     % ! ! ! ! ! ! ! ! ! ! ! ! !
89
90
91     spec = [];
92
93     for l = 1:length(d)-1
94         steps = 0:res:(ceil(d(l+1)/res)-1)*res; % this is inefficient
95         % x = [x (steps+depth)];
96         spec = [spec pstm(steps,l,lambda)];
97         % depth = depth + d(l+1);
98     end
99     % ! ! ! ! ! ! ! ! ! ! ! ! !
100    spec = T * spec;
101    % ! ! ! ! ! ! ! ! ! ! ! ! !

```

```

102     specs(:,iter)=spec;
103 end
104
105 %%%%%%
106 %
107 % Plotting
108 %
109 %%%%%%
110 specs=(abs(specs)).^2;
111 plot(x,specs(:,1))
112 hold all
113 for iter = 2:size(waves,2)
114     plot(x,specs(:,iter))
115 end
116 title('PEDOT / P3HTPCBM Device')
117 xlabel('depth (nm)')
118 ylabel('|E|^2')
119 legend(strtrim(cellstr(num2str(waves)))')
120
121 % vertical lines for layers
122 axislimit1=axis;
123 for matindex=2:length(d)
124     line([sum(d(1:matindex)) sum(d(1:matindex))],[0 axislimit1(4)]);
125 end
126
127 hold off
128
129
130 %%%%%%
131 %
132 % Helper Functions
133 %
134 %%%%%%
135
136 % layer matrix
137 function [L] = layer(l,lambda) % indices match paper
138     global q
139     global d
140     xi = (2*pi/lambda) * q(l+1);
141
142     L = [ exp(-1i*xi*d(l+1)) 0 ; 0 exp(1i*xi*d(l+1)) ];

```

```

143
144 % interface matrix
145 function [I] = interface(l,k) % indices match paper
146 global q
147 r_TE = (q(1+1)-q(k+1))/(q(1+1)+q(k+1));
148 t_TE = (2*q(1+1))/(q(1+1)+q(k+1));
149 % switch to these for TM transmission
150 % r_TM = (-n(k+1)^2*q(j+1)+n(j+1)^2*q(k+1))/(n(k+1)^2*q(j+1)+n(j+1)^2*q(k+1));
151 % t_TM = (2*n(j+1)*n(k+1)*q(j+1))/(n(k+1)^2*q(j+1)+n(j+1)^2*q(k+1));
152
153 I = 1/t_TE*[1 r_TE ; r_TE 1];
154
155 % scattering matrices
156 function [S_jp, S_jpp] = scattering(l,lambda)
157 global d
158 S_jp = eye(2);
159 for v = 1:(l-1)
160     S_jp = S_jp * interface(v-1,v) * layer(v,lambda);
161 end
162 S_jp= S_jp * interface(l-1,l);
163
164 S_jpp = eye(2);
165 for v = (l+1):(length(d)-1) %%
166     S_jpp = S_jpp * interface(v-1,v) * layer(v,lambda);
167 end
168 %S_jpp= S_jpp * interface(length(d)-2,length(d)-1); %%
169
170 % partial system transfer matrix. E(x) for single layer
171 function [tm] = pstm(x,l,lambda)
172 global q
173 global d
174 [s_jp,s_jpp] = scattering(l,lambda);
175
176 xi = 2*pi/lambda * q(1+1);
177
178 tm = (s_jpp(1,1)*exp(-1i*x*(d(1+1)-x))+s_jpp(2,1)*exp(1i*x*(d(1+1)-x))) ./ ...
179 (s_jp(1,1)*s_jpp(1,1)*exp(-1i*x*d(1+1))+s_jp(1,2)*s_jpp(2,1)*exp(1i*x*d(1+1)));
180
181
182
183 function ntotal = LoadRefrIndex(name,wavelengths)

```

```

184 %Data in IndRefr , Column names in IndRefr_names
185 [IndRefr,IndRefr_names]=xlsread('Index_of_Refraction_library.xls');
186
187 % Load index of refraction data in spread sheet, will crash if misspelled
188 % file_wavelengths=IndRefr(:,strmatch('Wavelength',IndRefr_names));
189 file_wavelengths=IndRefr(:,strncmp('Wavelength',IndRefr_names,10));
190 % n=IndRefr(:,strmatch(strcat(name,'_n'),IndRefr_names));
191 n=IndRefr(:,strncmp(strcat(name,'_n'),IndRefr_names,length(name)+2));
192 % k=IndRefr(:,strmatch(strcat(name,'_k'),IndRefr_names));
193 k=IndRefr(:,strncmp(strcat(name,'_k'),IndRefr_names,length(name)+2));
194
195 % Interpolate/Extrapolate data linearly to desired wavelengths
196 n_interp=interp1(file_wavelengths, n, wavelengths, 'linear', 'extrap');
197 k_interp=interp1(file_wavelengths, k, wavelengths, 'linear', 'extrap');
198
199 %Return interpolated complex index of refraction data
200 ntotal = n_interp+1i*k_interp;

```

## D.2 Out-Coupling (Power Dissipation)

The following model implements an out-coupling calculation by calculating the power dissipation as a function of the normalized in-plane wavevector,  $u$ . This is an implementation of the method outlined by Furno *et al.*<sup>10,11</sup>

PowerDissipationModel.m

```

1
2 function [] = PowerDissipationModel
3 %TE=s
4 %IM=p
5 clear
6
7 %%%%%%%%%%%%%%%%%%%%%%%%%%%%%%%%%%%%%%%%
8 % -----
9 % Model Parameters %%%
10 % -----
11 %%%%%%%%%%%%%%%%%%%%%%%%%%%%%%%%%%%%%%%%
12
13
14 % Layers. Must match names in lookup table
15 materials = {'SiO2' 'ITOzorizon' 'TCTA' 'Bphen' 'Irppy' 'Al' 'Air'};

```

```

16
17 % Wavelengths to test
18 waves = 1E-9*510; % freespace wavelengths
19
20 %% start u initiation and nreftable fetching
21 %#####
22 % Dipole inplane wave vectors %#
23 u_range = cat(2,0:.005:.999,1.001:.005:pi/2); %#
24 %#
25 % Load in index of refraction for each material and each wavelength %#
26 nreftable = zeros(size(materials,2),size(waves,2)); %#
27 for index = 1:size(materials,2) %#
28     nreftable(index,:) = LoadRefrIndex(materials{index},waves*1E9); %#
29 end %#
30 %#####
31 %% end u initiation and nreftable fetching
32
33 % Save u
34 % u_r = u_range';
35 % save('u.txt','u_r','-ascii')
36
37 %construct layer matrix
38 ntable(1,:) = nreftable(1,:); % glass
39 ntable(2,:) = nreftable(2,:); % ITO
40 ntable(3,:) = nreftable(3,:); % neat TCTA
41 ntable(4,:) = (nreftable(3,:)+nreftable(4,:))/2; % MEML
42 ntable(5,:) = nreftable(4,:); % neat bphen
43 ntable(6,:) = nreftable(6,:); % Al
44 ntable(7,:) = nreftable(7,:); % air
45
46 % layer thicknesses.
47 d(1) = 0; % Sio2
48 d(2) = 150; % ito
49 d(3)=20; %tcta
50 d(4)=60; %MEML
51 d(5)=20; %bphen
52 d(6) = 100; % Al
53 d(7) = 0; % air
54 d = d * 1E-9; % convert to nm
55
56 for thick_iter=1:60

```

```

57 % Emitter Matrix
58 % [layer    location_p(nm)    weight]
59 emitters = [
60     4 thick_iter 1
61 ];
62 emitters(:,2)=emitters(:,2)*1E-9;
63
64 %% Start main work loop
65 %#####
66 % -----
67 % Generation
68 % -----
69 %%%%%%
70 %#
71 % initialize power array
72 K_TMv = zeros(size(u_range));
73 K_TMh = zeros(size(u_range));
74 K_TEh = zeros(size(u_range));
75 K_TMvp = zeros(size(u_range));
76 K_TMhp = zeros(size(u_range));
77 K_TEhp = zeros(size(u_range));
78
79 % hard work begins
80 for wavelength_iter = 1:size(waves,2)
81     for wavenumber_iter = 1:size(u_range,2)
82         u = u_range(wavenumber_iter);
83
84
85         lambda = waves(wavelength_iter); % free space lambda
86         n=ntable(:,wavelength_iter);
87
88         K_TMv(wavenumber_iter)=0;
89         K_TMh(wavenumber_iter)=0;
90         K_TEh(wavenumber_iter)=0;
91         K_TMvp(wavenumber_iter)=0;
92         K_TMhp(wavenumber_iter)=0;
93         K_TEhp(wavenumber_iter)=0;
94
95         for emitter = 1:size(emitters,1)
96             q= (n.^2-((n(emitters(emitter,1)).*u)).^2).^(1/2);
97

```

```

98 % reflection coefficients                                     %#%
99 [r_TMP,t_TMP,~] = reflection_neg(emitters(emitter,1),lambda,0,n,d,q);    %#%
100 [r_TMn,~,~] = reflection_pos(emitters(emitter,1),lambda,0,n,d,q);      %#%
101 [r_TEp,t_TEp,~] = reflection_neg(emitters(emitter,1),lambda,1,n,d,q);    %#%
102 [r_TEn,~,~] = reflection_pos(emitters(emitter,1),lambda,1,n,d,q);       %#%
103                                                               %#%
104 k=2*pi*n(emitters(emitter,1))/lambda;                      %#%
105 z_p = emitters(emitter,2);                                %#%
106 z_n = d(emitters(emitter,1))-z_p;                         %#%
107 a_TMP = r_TMP*exp(2*j*k*sqrt(1-u.^2).*z_p); % Furno A4    %#%
108 a_TMn = r_TMn*exp(2*j*k*sqrt(1-u.^2).*z_n); % Furno A5    %#%
109 a_TEp = r_TEp*exp(2*j*k*sqrt(1-u.^2).*z_p); % Furno A4    %#%
110 a_TEn = r_TEn*exp(2*j*k*sqrt(1-u.^2).*z_n); % Furno A5    %#%
111                                                               %#%
112 % Radiated Power Density                                 %#%
113 K_TMv(wavenumber_iter) = K_TMv(wavenumber_iter) + emitters(emitter,3).*3/4*real(   %#%
114 u.^2./sqrt(1-u.^2).*(1+a_TMP).*(1+a_TMn)./(1-a_TMP.*a_TMn)); % Furno A1      %#%
115 K_TMh(wavenumber_iter) = K_TMh(wavenumber_iter) + emitters(emitter,3).*3/8*real(   %#%
sqrt(1-u.^2).*(1-a_TMP).*(1-a_TMn)./(1-a_TMP.*a_TMn)); % Furno A2      %#%
116 K_TEh(wavenumber_iter) = K_TEh(wavenumber_iter) + emitters(emitter,3).*3/8*real(   %#%
(1./sqrt(1-u.^2).*(1+a_TEp).*(1+a_TEn)./(1-a_TEp.*a_TEn)); % Furno A3      %#%
117                                                               %#%
118 % Transmission of the top half-stack                   %#%
119 T_TMP = abs(t_TMP).^2*(n(1)/n(emitters(emitter,1)))*sqrt((1-(u*n(emitters(   %#%
emitter,1))/n(1))^2)/(1-u^2)); % Furno A12
120 T_TEp = abs(t_TEp).^2*(n(1)/n(emitters(emitter,1)))*sqrt((1-(u*n(emitters(   %#%
emitter,1))/n(1))^2)/(1-u^2)); % Furno A13
121                                                               %#%
122 % Power radiated into the substrate                    %#%
123 K_TMvp(wavenumber_iter) = K_TMvp(wavenumber_iter) + emitters(emitter,3).*3/8*(u   %#%
.^2./sqrt(1-u.^2).*(abs(1+a_TMn)).^2./((abs(1-a_TMP.*a_TMn)).^2)*T_TMP; % Furno A8
124 K_TMhp(wavenumber_iter) = K_TMhp(wavenumber_iter) + emitters(emitter,3).*3/16*(   %#%
sqrt(1-u.^2).*(abs(1-a_TMn)).^2./((abs(1-a_TMP.*a_TMn)).^2)*T_TMP; % Furno A9
125 K_TEhp(wavenumber_iter) = K_TEhp(wavenumber_iter) + emitters(emitter,3)   %#%
.*3/16*(1./sqrt(1-u.^2).*(abs(1+a_TEn)).^2./((abs(1-a_TEp.*a_TEn)).^2)*T_TEp; % Furno A10
126                                                               %#%
127 end % emitter                                         %#%
128 end % wavenumber                                      %#%
129 end % wavelength                                     %#%

```

```

130 K = (1/3*(abs(K_TMv)+2*abs(K_TMh)+2*abs(K_TEh))) ; % Forno A6      %#  

131 K = K./sum(emitters(:,3));                                %#  

132  
133  
134 % Transmission out of the substrate to air             %#  

135 n_g = ntable(1,1);                                         %#  

136 n_a = 1;                                                 %#  

137 u_g = u_range*ntable(emitters(1),1)/ntable(1,1);        %#  

138 cos_g = sqrt(1-u_g.^2);                                    %#  

139 cog_a = sqrt(1-(n_g./n_a.*u_g).^2);                      %#  

140 Rs = ((n_g.*cos_g-n_a.*cog_a)./(n_g.*cos_g+n_a.*cog_a)).^2;    %#  

141 T_s = 1-Rs;                                              %#  

142 Rp = ((n_g.*cog_a-n_a.*cos_g)./(n_g.*cog_a+n_a.*cos_g)).^2;    %#  

143 T_p = 1 - Rp;                                            %#  

144 % This calculation assumes a lossless interface          %#  

145  
146 % Outcoupled Power                                     %#  

147 n = ntable(:,1);                                         %#  

148 Rc_s=zeros(1,size(u_range,2));                            %#  

149 Rc_p=zeros(1,size(u_range,2));                            %#  

150 for u_iter = 1:size(u_range,2)                          %#  

151     q= (n.^2-((n(1,1).*u_range(u_iter))).^2).^(1/2);    %#  

152     Rc_s(u_iter) = abs(reflection_neg(1,waves(1),1,ntable(:,1),d,q))^2;    %#  

153     Rc_p(u_iter) = abs(reflection_neg(1,waves(1),0,ntable(:,1),d,q))^2;    %#  

154 end                                                       %#  

155 K_outTMv = K_TMvp.*T_p./(1-Rp.*Rc_p); % Forno A14      %#  

156 K_outTMh = K_TMhp.*T_p./(1-Rp.*Rc_p); % Forno A14      %#  

157 K_outTEh = K_TEhp.*T_s./(1-Rs.*Rc_s); % Forno A14      %#  

158  
159 K_out = (1/3*(abs(K_outTMv)+2*abs(K_outTMh)+2*abs(K_outTEh)));    %#  

160 K_out=K_out./sum(emitters(:,3));                           %#  

161  
162 % Power Dissipation Spectra                         %#  

163 y=u_range.*K;                                           %#  

164 y_out=u_range.*K_out;                                     %#  

165  
166 % critical angle from snells law                  %#  

167 u_crit = 1/real(ntable(emitters(emitter,1),1));        %#  

168 index=find(u_range<u_crit,1,'last')+1;                 %#  

169 out = trapz(u_range(1:index),y_out(1:index)); % Forno A15    %#  

170 tot = trapz(u_range,y); % Forno A7                   %#
```

```

171 %#
172 eta(thick_iter)=out/tot; %#
173 %# %#
174 % Power vs Angle %#
175 % sin_theta = u_range(1:113)/u_range(113); %#
176 % theta = asind(sin_theta); %#
177 % cos_theta = cosd(theta); %#
178 % P_out = (1/ntable(emitters(1),1)).^2.*cos_theta/pi.*K_out(1:113); % Furno A18 %#
179 %#
180 %#
181 ##### %#
182 %% End main work loop %#
183 %#
184 % End Control Loops %#
185 end %#
186 %#
187 ##### %#
188 %-----%%%
189 % Plotting %%%
190 %-----%%%
191 ##### %#
192 %#
193 %#
194 % Power Spectrum vs u %#
195 % semilogy(u_range,y) %%%
196 % xlabel('u') %%%
197 % ylabel('K*u') %%%
198 %#
199 % Power Intensity vs Angle (requires uncommenting of angle code) %%%
200 % plot(theta,P_out); %%%
201 %#
202 %#
203 %#
204 ##### %%%
205 %-----%%%
206 % Saving %%%
207 %-----%%%
208 ##### %%%
209 save('eta.txt','eta','ascii') %%%
210 %#
211

```

```

212
213
214
215 %%%%%%%%%%%%%%%%%%%%%%%%%%%%%%%%%%%%%%
216 %%%%%%%%%%%%%%%%%%%%%%%%%%%%%%%%%%%%%%
217 %
218 % Helper Functions
219 %
220 %%%%%%%%%%%%%%%%%%%%%%%%%%%%%%%%%%%%%%
221 %%%%%%%%%%%%%%%%%%%%%%%%%%%%%%%%%%%%%%
222
223
224 % layer matrix -----
225 %
226 function [L] = layer(l,lambda,~,d,q)
227
228
229     xi = (2*pi/(lambda)) * q(1); % pettersson 6
230
231     L = [ exp(-1i*xi*d(1)) 0 ; 0 exp(1i*xi*d(1)) ]; % pettersson 5
232
233 % interface matrix -----
234 %
235 % o is orientation 0=TM, 1=TE
236 function [I] = interface(l,k,orientation,n,~,q)
237
238     if(orientation==1)
239         % TE light
240         r = (q(1)-q(k))./(q(1)+q(k)); % pettersson 2a
241         t = (2*q(1))./(q(1)+q(k)); % pettersson 2b
242     else
243         % TM light
244         r = (n(k)^2*q(1)-n(1)^2*q(k))./(n(k)^2*q(1)+n(1)^2*q(k)); % pettersson 3a
245         t = (2*n(1)*n(k)*q(1))./(n(k)^2*q(1)+n(1)^2*q(k)); % pettersson 3b
246
247     end
248
249     I = 1/t .* [1 r ; r 1]; % pettersson 1
250     % checks for singular matrix. If so, a small term is added to the diagonal,
251     % a common method of dealing with singular matrices.
252     % This adds in potential error, but

```

```

253 % makes the system solvable and stable. Will fail if NaN is passed
254 %if ( cond(I) > 1E8)
255 %    I = I+eye(2)*1E-5;
256 %end
257
258 % reflection coefficient Positive Direction -----
259 %
260 %Uses the Interface and layer matrices , but in the appropriate directions.
261 function [r,t,D] = reflection_pos(active_layer,lambda,orientation,n,d,q)
262
263 S_jpp = eye(2);
264 for v = (active_layer):(length(d)-2)
265     S_jpp = S_jpp * interface(v,v+1,orientation,n,d,q) * layer(v+1,lambda,n,d,q); % pettersson 13
266 end
267 S_jpp = S_jpp * interface(length(d)-1,length(d)-0,orientation,n,d,q);
268 r = S_jpp(2,1)/S_jpp(1,1); % pettersson 9
269 t = 1/S_jpp(1,1); % Pettersson 15
270
271 D=det(S_jpp);
272
273 % reflection coefficient Negative Direction -----
274 %
275 function [r,t,D] = reflection_neg(active_layer,lambda,orientation,n,d,q)
276 S_jp = eye(2);
277 % for v = (active_layer):-1:3
278 for v = (active_layer):-1:3 % Treat glass as semiinfinite
279     S_jp = S_jp * interface(v,v-1,orientation,n,d,q) * layer(v-1,lambda,n,d,q); % pettersson 13
280 end
281 S_jp = S_jp * interface(2,1,orientation,n,d,q);
282 r = S_jp(2,1)/S_jp(1,1); % pettersson 9
283 t = 1/S_jp(1,1); % Pettersson 15
284
285 D=det(S_jp);
286 %t=D*t;
287
288 % Index fetching from files -----
289 %
290 function ntotal = LoadRefrIndex(name,wavelengths)
291     %Data in IndRefr , Column names in IndRefr_names

```

```

292 [IndRefr,IndRefr_names]=xlsread('Index_of_Refraction_library.xls');
293
294 % Load index of refraction data in spread sheet, will crash if misspelled
295 file_wavelengths = IndRefr(:,strncmp('Wavelength',IndRefr_names,10));
296 n = IndRefr(:,strncmp(strcat(name,'_n'),IndRefr_names,length(name)+2));
297 k = IndRefr(:,strncmp(strcat(name,'_k'),IndRefr_names,length(name)+2));
298
299 % Interpolate/Extrapolate data linearly to desired wavelengths
300 n_interp = interp1(file_wavelengths, n, wavelengths, 'linear', 'extrap');
301 k_interp = interp1(file_wavelengths, k, wavelengths, 'linear', 'extrap');
302
303 %Return interpolated complex index of refraction data
304 ntotal = n_interp+1i*k_interp;

```

## Appendix E

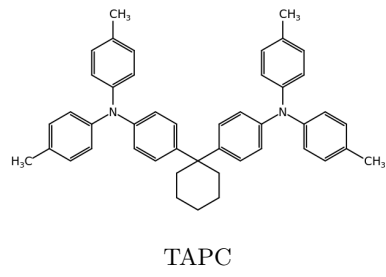
# Lifetime Box Code

The following code outlines our implementation of lifetime setup and can be found on the Holmes Group Github page at <https://github.umn.edu/HolmesGroup/lifetimeTesting>. To implement all boxes, code is organized into separate files. *box.py* contains all general functions shared between all hardware implementations and is the main driver for lifetime. Different hardware configurations require different commands in order to control the hardware. These hardware specific implementation details are located in *keithleyBox.py*, *keithleyBox2.py*, and *keysightBox.py*. To facilitate hardware rearrangement, configuration files, such as *box1.json* coordinate hardware. Finally, each piece of hardware is uniquely named in Linux using udev rules, outlined in *85-lifetime.rules*.

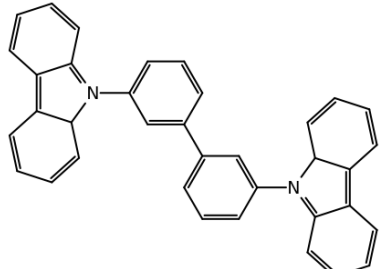
```
box.py  
keithleyBox.py  
keithleyBox2.py  
keysightBox.py  
box1.json  
85-lifetime.rules
```

## Appendix F

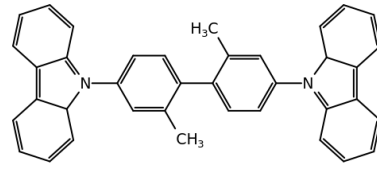
### Chemical Structures



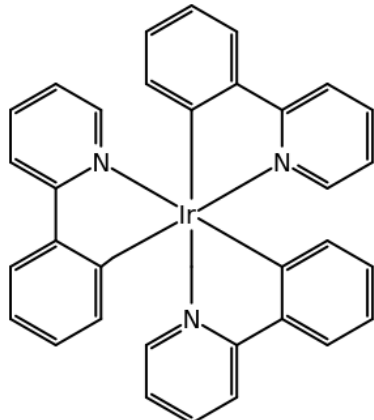
TAPC



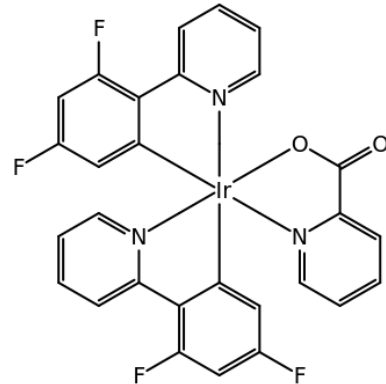
mCBP



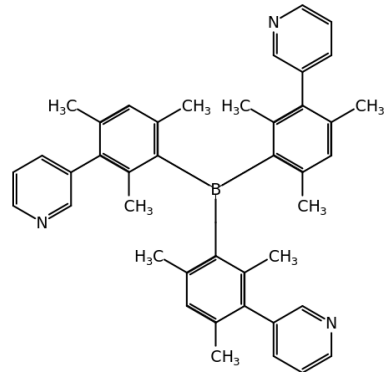
CDBP



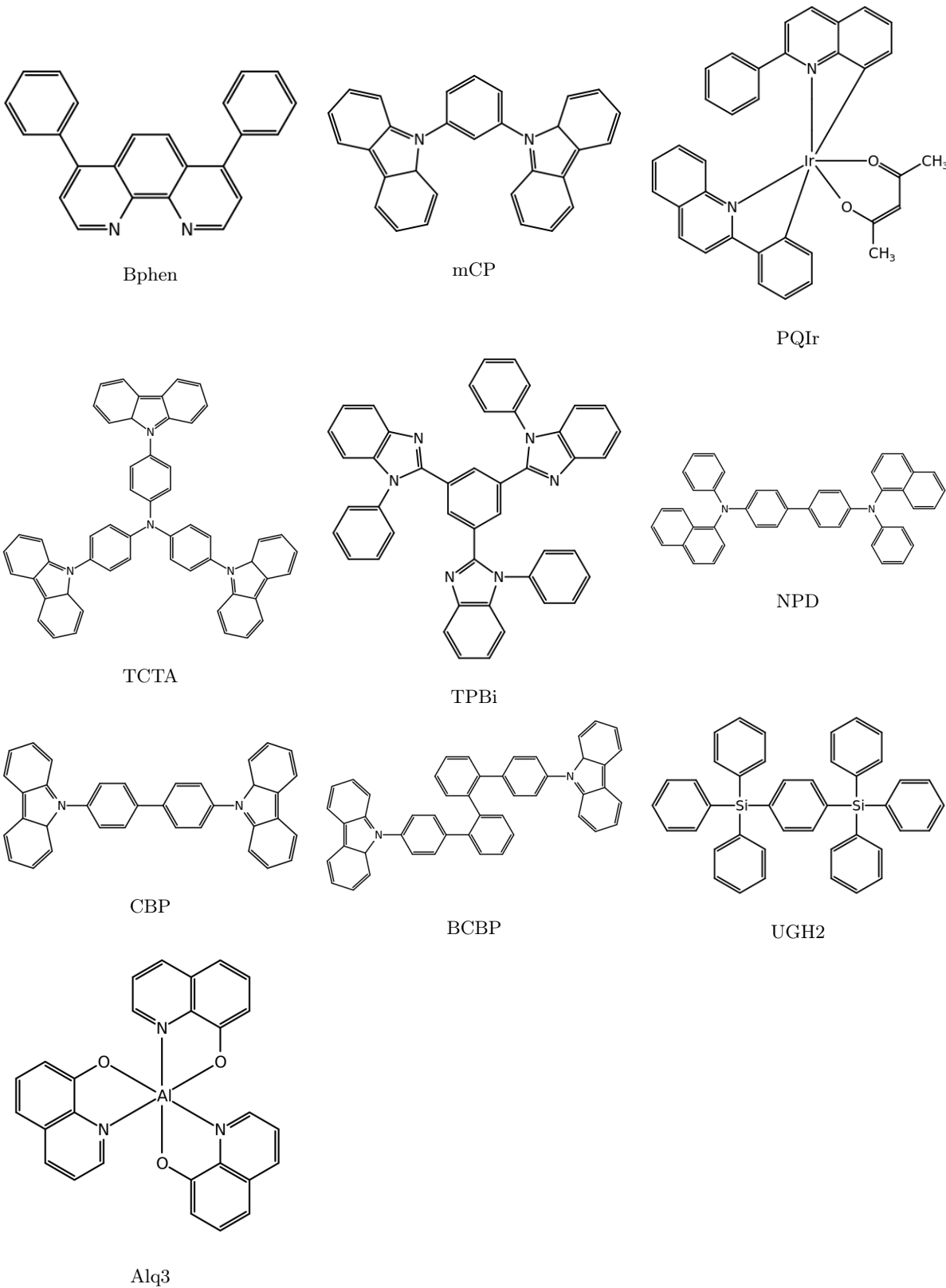
Ir(ppy)<sub>3</sub>



FIrpic



3TPYMB



## Appendix G

# Material Properties

Common Name	Chemical Name	Other Names	HOMO	LUMO	E <sub>T</sub>	CAS	T <sub>melt</sub>	M.W.	τ
3TPYMB	b'Tris(2,4,6-triMethyl-3-(pyridin-3-yl)phenyl)borane'		6.7	3.3		929203021		599.61	
4CzIPN	b'(4s,6s)-2,4,5,6-tetra(9H-carbazol-9-yl)isophthalonitrile'		5.8	3.4		1416881521		788.89348	
Ag	b'Silver'	silver ag	4.6	4.6		7440224	962.0	107.868	
Air	b'Aluminum'								
Alq3	b'Tris(8-hydroxyquinoline)aluminuhydroxyquinolinate)aluminum Aluminum oxinate	Tris(8-hydroxyquinoline)aluminuhydroxyquinolinate)aluminum Aluminum oxinate	5.62	2.85		7429905	660.0	26.981	
		Aluminum hydroxyquinolate 8-Hydroxyquinoline aluminum salt				2085338		459.43	
Anthracene	b'Anthracene'						120127		178.23
AQ1200	b'						5.5		
AQ1250							5.5		
Au	b'Gold'	gold au				7440575	1064.0	196.97	

Common Name	Chemical Name	Other Names	HOMO	LUMO	E <sub>T</sub>	CAS	T <sub>melt</sub>	M.W.	τ
B3PYMPM	b'bis-4,6-(3,5-di-3-pyridylphenyl)-2-methylpyrimidine'		6.8	3.3		925425963		554.64	
BCBP	b''2,2'-Bis(4-(carbazol-9-yl)phenyl)-biphenyl"		6.1	2.6		858131701		636.78	
BCP	b'Bathocuproine'		6.5	1.6		4733395		360.45	
BP2T	b'5,5u-[Di(1,1u-biphenyl)-4-yl]-2,2ubithiophene'		7.0	3.5		175850289		470.658	
BP4mPy	b'3,5,3A,5A-tetra(m-pyrid-3-yl)phenyl[1,1A]-biphenyl'	3,5,3',5'-tetra(m-pyrid-3-yl)phenyl[1,1']biphenyl	6.66	2.57		1009033946	191	766.93	
Bphen	b'Bathophenanthroline'	4,7-Diphenyl-1,10-phenanthroline	6.4	3.0		1662017		332.4	
BPy-TP2	b'2,7-Bis(2,20-bipyridine-5-yl)triphenylene'		5.7	2.7		1394813581		536.624	
c-TiO <sub>2</sub>									
C60	b'Fullerene'	fullerene	6.1	3.7		99685968		720.64	
C70	b'[5,6]Fullerene'	fullerene C60	6.3	3.5		115383227		840.75	

Common Name	Chemical Name	Other Names	HOMO	LUMO	E <sub>T</sub>	CAS	T <sub>melt</sub>	M.W.	τ
CBP	b'4,4'-Bis(N-carbazolyl)-1,1'-biphenyl'		6.1	1.9		58328317		484.59	0.7
CDBP	b"4,4'-Bis(9-carbazolyl)-2,2'-dimethylbiphenyl"		6.0	2.9		120260017		512.64	
ClAPc	b'Aluminum phthalocyanine chloride'					14154428		574.96	
CuPc	b'Copper(II) phthalocyanine'		4.8	2.6		147148		576.07	
CzSi	b'9-(4-tert-butylphenyl)-3,6-bis(triphenylsilyl)-9H-carbazole'		6.0	2.5		898546822		816.19	
CzTRZ	b'9-[4-(4,6-diphenyl-1,3,5-triazin-2-yl)phenyl]-9H-carbazole'		6.08	3.28		nan	nan		
Dow ETL			5.1	1.808					
Dow ETL2			5.842	1.908					
Dow HIL			4.509	1.128					
Dow Host A			5.669	2.269					

Common Name	Chemical Name	Other Names	HOMO	LUMO	$E_T$	CAS	$T_{melt}$	M.W.	$\tau$
Dow Host B			1.223						
Dow HTL			5.261	2.361	1.872				
DPDCPB	b'2-[7-(4-Diphenylaminophenyl)-2,1,3-benzothiadiazol-4-yl]methylene]propanedinitrile'		5.5	3.36	1.039	1393343606	455.53		
DPDCTB	b''		5.35	3.44					
DTDCPB	b'2-[7-4-[N,N-Bis(4-methylphenyl)amino]phenyl]-2,1,3-benzothiadiazol-4-yl]methylene]propanedinitrile'		5.43	3.35	1.3582	1393343582	483.59		
DTDCTB	b'2-[7-(5-N,N-Ditolylamino)phenyl]-2-yl]-2,1,3-benzothiadiazol-4-yl]methylene]malononitrile'		5.3	3.44		1335150098	489.61		
Flrpic	b'Bis[2-(4,6-difluorophenyl)pyridinato-C2,N](picolinato)iridium(III)		5.8	2.9		376367930	694.66		
Glass	b'Silicon Dioxide'								

Common Name	Chemical Name	Other Names	HOMO	LUMO	E <sub>T</sub>	CAS	T <sub>melt</sub>	M.W.	τ
H2P <sub>c</sub>	b'29H,31H- Phthalocyanine'				574936		514.54		
HATCN	b'1,4,5,8,9,11- Hexaaazatriphenylenehexacarbonitrile'		9.5	5.5	105598274		384.27		
Hoye CoOMe			7.5	4.4					
Hoye Nap CoOMe									
Hoye Nap NPh <sub>2</sub>									
Hoye Nap OMe									
Hoye Nap H									
Hoye OH									
Hoye OMe									
Hoye Triben-H									
Hoye Triben OMe									
Hoye OMe	b'		6.07	2.55					
Ir(dpm)PQ2	b'Bis(2- phenylquinoline)(2,2,6,6- tetramethylheptane- 3,5- dionate)iridium(III)'				713079039		783.98		
Ir(mphq) <sub>3</sub>	b'Tris[2-phenyl-4- methylquinoline]iridium(III)'				1433853907		847.04		

Common Name	Chemical Name	Other Names	HOMO	LUMO	E <sub>T</sub>	CAS	T <sub>melt</sub>	M.W.	τ
Ir(ppy) <sup>3</sup>	b'Tris[2-phenylpyridinato-C2,N]iridium(III)',		5.1	2.6	94928866		654.78	1000.0	
ITO	b'Indium Tin Oxide'				50926119				
Li(acac)									
LiF	b'Lithium Fluoride'		2.8		7789244		25.94		
LiQ	b'8-Quinolinolato lithium (Liq)'		4.667	1.292	25387933		151.09		
MADN	b'2-Methyl-9,10-bis(naphthalen-2-yl)anthracene'		5.6	2.6	804560007		444.57		
MAI									
mCBP	b' <sup>1</sup> 3,3'-Bis(N-carbazolyl)-1,1'-biphenyl"		6.0	2.4	342638544		484.58916		
mCP	b'1,3-Bis(N-carbazolyl)benzene'		6.1	2.4	550378784	187.0	408.49		
MgPc	b'Magnesium phthalocyanine'		5.9		1661036		536.83		
MoO <sub>x</sub>	b'Molybdenum(VI) oxide'				1313275		143.94		

Common Name	Chemical Name	Other Names	HOMO	LUMO	E <sub>T</sub>	CAS	T <sub>melt</sub>	M.W.	τ
NPD	b'N,N-Di(1-naphthyl)-N,N-diphenyl-(1,1-biphenyl)-4,4-diamine'		5.3	2.3		123847858	280.0	588.74	3.5
NTCDA	b'1,4,5,8-Naphthalenetetracarboxylic dianhydride'		5.4 5.4	1.52 2.4		81301		268.18	
NTU1	b'2-[7-(4-ethyl-4H-thieno[3,2-b]indol-2-yl)benzo[c][1,2,5]thiadiazol-4-yl]-methylene malononitrile'								
NTU2	b'2-[7-(8-ethyl-8Hthieno[2,3-b]indol-2-yl)benzo[c][1,2,5]thiadiazol-4-yl]-methylene malononitrile'								
P3HT	b'Poly(3-hexylthiophene-2,5-diyl)'						156074985		
PbPC	b'Lead(II) phthalocyanine'					15187163		719.72	

Common Name	Chemical Name	Other Names	HOMO	LUMO	$E_T$	CAS	$T_{melt}$	M.W.	$\tau$
Pedot	b'Poly(3,4-ethylenedioxythiophene)-poly(styrenesulfonate)'								
Pentacene	b'Pentacene'		5.2 4.85 5.0	3.0 2.8 3.2		135488 300.0	278.35		
Perfluoropentacene	b'perfluoropentacene'		6.7	5.0		646533882		530.22	
PO-T2T	b'2,4,6-Tris[3-(diphenylphosphoryl)phenyl]-1,3,5-triazine'		6.83	2.83		1646906284	287	909.8	
PPT	b'2,8-Bis(diphenylphosphoryl)dibenzo[b,d]thiophene'		7.5	3.5			1019842999	584.6	
PQIr	b'(2,4-Pentanedionato)bis[2-(2-quinoliny)phenyl]iridium(III)'					337526951		699.82	
Pt17									
PTCBI	b'3,4,9,10-Perylenetetracarboxylic Bisbenzimidazole'		6.2	4.3		79534911		536.54	
PTCDA	b'Perylene-3,4,9,10-tetracarboxylic dianhydride'		6.95	4.1		128698	392.32	3.2	

Common Name	Chemical Name	Other Names	HOMO	LUMO	E <sub>T</sub>	CAS	T <sub>melt</sub>	M.W.	τ
PTCDI	b'N,N-Dioctyl-3,4,9,10-perylenedicarboximide'	PTCDI-C8	6.2	6.2		78151583		614.77	
PtOEP	b'Platinum octaethylporphyrin'					31248392		727.84	
PtTPTBP	b'Platinum(II) tetraphenyltetra-benzoporphyrin'	[6,13,20,27-Tetraphenyl-29H,31H-tetrabenzo[porphyrinato(2-)-κ2N29,N31]platinum Pt(II)] meso-Tetraphenyl benzoporphine Tetra-platinum tetraphenyl-tetrabenzo[porphine PtTPBP]	4.8	2.9		166174056		1008.0	
Quartz									
Rubrene	b'5,6,11,12-Tetraphenylnaphthacene		4.85	3.15		517511		532.67	9.1

Common Name	Chemical Name	Other Names	HOMO	LUMO	$E_T$	CAS	$T_{melt}$	M.W.	$\tau$
SnI22									
SnNcCl2	b'Tin(IV) 2,3-naphthalocyanine dichloride'				26857614		902.37		
SubNc	b'Boron sub-2,3-naphthalocyanine chloride'	SubNc-Cl	5.35	3.47	142710563		580.83		
SubPc	b'Boron subphthalocyanine chloride'	SubPc-Cl	5.6	3.2	36530060	375.0	430.66	0.5	
T2T	b'2,4,6-tris(biphenyl-3-yl)-1,3,5-triazine'		5.57	3.6					
TAPC	b'4,4-Cyclohexyldenebis[N,N-bis(4-methylphenyl)benzamine]'		6.5	3.0	1201800830		537.652		
TAZ	b'3-(Biphenyl-4-yl)-5-(4-tert-butylphenyl)-4-phenyl-4H-1,2,4-triazole'		6.3	2.7	150405699		429.56		
TCTA	b'Tris(4-carbazoyl-9-ylphenyl)amine'		5.7	2.4	139092787		740.89		
Tetracene	b'Benz[b]anthracene'		5.1	1.8	92240		228.29		

Common Name	Chemical Name	Other Names	HOMO	LUMO	E <sub>T</sub>	CAS	T <sub>melt</sub>	M.W.	τ
TmPyPB	b'1,3,5-Tri(n-pyrid-3-ylphenyl)benzene'		6.63	2.54		921205030	181	537.65	
TPBi	b'2,2,2"-{1,3,5-Benzinetriyl}-tris(1-phenyl-1-H-benzimidazole)'		6.68	2.73					
TPD	b'N,N-Bis(3-methylphenyl)-N,N-diphenylbenzidine'		6.1	2.8		192198859		654.76	
Tris-PCz	b'9,9,9-triphenyl-9H,9H,9H-3,3:6,3-tercarbazole'	9,9'-Diphenyl-6-(9-phenyl-9H-carbazol-3-yl)-9H,9'H-3,3'-bicarbazole	5.5	2.3		65181784		516.67	
UGH2	b'p-Bis(triphenylsilyl)benzene;Benzene,1,4-bis(triphenylsilyl);1,4-Phenylenebis[triphenylsilane];1,4-Phenylenebis(triphenylsilsilane)'		7.2	2.8		18856081	345.0	594.89	
ZnPc	b'Zinc phthalocyanine'		5.28	3.3		14320048		577.91	

# List of Figures

1.1 Simplified Jablonski diagram. . . . .	7
2.1 Basic layer diagram for OLED devices. . . . .	8
2.2 Energy level diagram of an OLED. Energy is shown in reference to the vacuum level. Electrons are shown in black spheres, holes shown in white. . . . .	9
2.3 External Quantum Efficiency on energy level diagram. $\eta_{OC}$ represented in blue, $\eta_{PL}$ in green, $\chi$ in purple, and $\eta_{EF}$ in red. . . . .	10
2.4 a. Angstrom vacuum chamber b. Organic deposition boat c. Aluminum deposition boat . . .	11
2.5 a. ITO Pattern b. Organic Mask c. Metal Mask d. Mask Overlays. Device area shown in red. . .	12
2.6 a. Device current voltage and luminance voltage behavior . . . . .	13
2.7 a. Silicon detector responsivity b. Photopic response . . . . .	14
2.8 a. Simple color addition diagram. b. CIE $xyY$ color space. . . . .	15
2.9 Various phone display limits shown on CIE coordinates . . . . .	16
2.10 Structure of the first OLED cell from Tang and VanSlyke [22]. Diamine is commonly referred to now as TAPC. . . . .	17
2.11 Molecular structure of the green phosphor, $\text{Ir}(\text{ppy})_3$ . . . . .	18
2.12 Reverse intersystem crossing for TADF materials. Figure taken from Uoyama et al. [35]. . .	18
2.13 Efficiency roll-off as a function of current density . . . . .	19
2.14 Recombination zone measurement architecture. The curly brace indicates the device stack. Figure taken from Erickson and Holmes [68] . . . . .	20
2.15 Recombination zone comparison for an emissive sensitizer analyzed using the quenched ratio and the emitted ratio as a function of current density. . . . .	21
2.16 a. Hole only device. b. Electron only device. . . . .	22
2.17 a. Dark spot in PL on an active device area, taken from Kolosov et al. [92]. b. Cathode bubbling where delamination has occurred under SEM, as shown in Wang et al. [93] . . . .	24

LIST OF FIGURES

2.18	Mass spectroscopy data taken from Seifert et al. [125] . . . . .	26
2.19	Emission from Ir(ppy) <sub>3</sub> and CBP, as reported by Zhang and Aziz [103] a. All emission, b. Emission shoulder, showing CBP emission, c. CBP emission with Ir(ppy) <sub>3</sub> background subtracted. . . . .	28
2.20	Device emission spectra containing a. PtOEP sensitizer on the ETL side of the device, b. PtOEP sensitizer on the HTL side of the device, DCM2 sensitizer on the ETL side of the device. Reproduced from Coburn and Forrest [70] . . . . .	29
3.1	Fitting the transient electroluminescence decay without polaron dynamics. . . . .	30
3.2	(a) Efficiency roll-off predicted by Erickson <i>et al.</i> 2014 as a function of recombination zone width. <sup>55</sup> (b) Observed efficiency roll-off for gradient EML devices. . . . .	31
3.3	Extracted polaron injection time is shown as a function of voltage along with a fit from the model. . . . .	34
3.4	(a) Transient photoluminescence (PL) decays for several initial exciton densities with fits shown as solid lines using Equation 3.2. Fit parameters are discussed in SECTION. Exciton densities are calculated using measured incident power and beam size in combination with Beer's Law. (b) Steady-state PL quenching as a function of polaron density and the resulting fit from Equation 3.11 shown as the solid line. . . . .	37
3.5	Normalized experimental $\eta_{EQE}$ as a function of current density. Solid line is a fit to the data using Equation 3.1 and 3.3 in the absence of polaron loss. Pulsed EQE measurements are conducted using low duty cycle pulses to steady-state luminance to reduce Joule heating in device. . . . .	40
3.6	Transient electroluminescence (EL) for four different current densities (J) and device areas (A). (a) $0.25 \text{ cm}^2$ device at a current density during the pulse of $J = 0.9 \text{ A/cm}^2$ (b) $0.25 \text{ cm}^2$ device at $J = 2.2 \text{ A/cm}^2$ (c) $0.0079 \text{ cm}^2$ device at $J = 7.6 \text{ A/cm}^2$ (d) $0.0079 \text{ cm}^2$ device at $J = 38 \text{ A/cm}^2$ . . . . .	41
3.7	Term efficiency for each dynamical process influencing the exciton population for (a) $0.25 \text{ cm}^2$ device operated at $0.9 \text{ A/cm}^2$ for 500 ns and (b) $0.785 \text{ mm}^2$ device operated at a current density of $38 \text{ A/cm}^2$ for 250 ns. Relative term amplitude is calculated as the magnitude of each term in Equation 3.1 divided by the sum of absolute values of each term. . . . .	42

3.8	Transit time extracted from $\eta_{\text{EQE}}$ measurements are shown as the red circles. Predictions using the drift model are calculated using Equation 3.12. The drift model assumes a uniform electric field. Good agreement between the experimental transit time and the drift model is found for a field distributed over 20 nm. The charge balance factor is shown as a function of current density in blue squares. . . . .	43
3.9	Current density formalism within the circuit. $J_1$ and $J_2$ are the currents measured on either side of the device. $J_e$ and $J_h$ are the electron and hole currents within the device and $J_l$ is the unbalanced current, assumed to be only holes, that leaks out of the opposing contact. . . . .	45
3.10	The quantity $\alpha(1 - \alpha)$ is plotted as a function of the polaron composition, $\alpha$ and the electron to hole ratio. . . . .	46
4.1	Cross polarized optical micrographs of (a) active device area (b) crystallized film from Fielitz <i>et al.</i> <sup>5</sup> (I) Orthorhombic phase, (III) 200 $\mu\text{m}$ scale bar . . . . .	50
4.2	(a) Experimental configuration for the measurement of electro- (EL) and photoluminescence (PL) during OLED degradation. Laser excitation is incident on a subsection of the device area. The laser is aligned so that neither the incident nor reflected beam strikes the detector. Stray laser light is removed by a $\lambda=475$ nm dielectric long pass filter. (b) Excitation scheme. EL and PL signals are probed independently with no temporal overlap. (c) External quantum efficiency versus current density and luminance for devices having emissive layer thickness of 10 nm, 20 nm and 30 nm. . . . .	51
4.3	Lifetime obtained under a constant driving current is shown in red solid line. Lifetime under the same conditions but with PL measurement breaks is shown in open squares. Strong agreement is observed. . . . .	51
4.4	Extinction coefficients shown for the green emitter Ir(ppy) <sub>3</sub> and blue emitter Fir(pic) as well as a few host materials. . . . .	52
4.5	Exciton recombination zone (RZ) and pump intensity $ E ^2$ for a hypothetical thick EML device are shown. . . . .	53
4.6	Dark spot formation on a device after exposure to a 405 nm laser. . . . .	53
4.7	Multiplicative correction factor for exciton formation efficiency due to changes in quenching during lifetime. Shown as a function of polaron and exciton density as well as luminance, assuming a 10 nm emissive layer. . . . .	54
4.8	Exciton lifetime ratio extracted from transient PL measurements on degraded and undegraded devices as a function of PL degradation for several emissive layer thickness. . . . .	55

## LIST OF FIGURES

4.9 Initial Attempts at measuring $\eta_{PL}$ during degradation using individual devices from the PTI . . . . .	56
4.10 First generation lifetime box setup. a. Box layout b. Electronics c. dark enclosure (cardboard box) d. software interface . . . . .	57
4.11 Box workflow summary. Top panel shows the operation of Boxes 1 and 2, bottom shows Box 3. . . . .	58
4.12 Source-Measure hardware and laser controller . . . . .	59
4.13 Device contacting, measurement, and optical hardware. Version 3 of the hardware is shown. Controlling hardware is shown in Fig. 4.12 . . . . .	59
4.14 6 channel software controller. Selection of test type, laser control for alignment, and global settings are accessible on the top of the interface. Individual channel settings are grouped on the bottom. . . . .	60
4.15 Test information for database import interface. The top left panel collects information about the specific device and lifetime. The right panel connects the device to a particular growth and architecture. The bottom panel confirms the architecture. . . . .	61
5.1 a. Device architecture, featuring EML thicknesses of X=10,20, and 30 nm. b. External Quantum Efficiency ( $\eta_{EQE}$ ) for the three architectures. Operational points for lifetime are shown in symbols. . . . .	62
5.2 Device decay curves for multiple values of the initial luminance as a function of emissive layer thickness. Loss in (a) electroluminescence (EL) and (b) photoluminescence (PL) are shown and decrease monotonically with increasing luminance. For devices with a 10-nm-thick emissive layer, initial luminance values are 1000 $cd/m^2$ , 5000 $cd/m^2$ , and 7000 $cd/m^2$ . For devices with a 20-nm- or 30-nm-thick emissive layer, initial luminance values are 1000 $cd/m^2$ , 5000 $cd/m^2$ , and 7100 $cd/m^2$ . . . . .	63
5.3 Extracted lifetimes for all 3 architectures as a function of luminance. . . . .	64
5.4 a. TPTBP quenched 30 nm devices. No quenching is observed. b. TPTBP quenched 20 nm devices. Quenching is observed for the ETL side quencher, and minimally for the HTL side. c. PtTPTBP quenched 10 nm EML devices. Emission from the sensitizer only at the ETL. d. Summary of recombination zone measurements. . . . .	65
5.5 a. Current Density and b. Luminance as a function of Voltage. c. $\eta_{EQE}$ for all three EML thicknesses. Inset is MEML device architecture. . . . .	66
5.6 a. Raw spectra of sensitized devices. b. Out-coupling for Ir(ppy) <sub>3</sub> and PtTPTBP across the EML as well as electric field profile. c. RZ as a function of current density. For all currents, the RZ is found to span the entire EML. . . . .	67

## LIST OF FIGURES

5.7 a. EL lifetime at 3,000 cd/m <sup>2</sup> for EML thicknesses of 10,30,60 nm. b. The corresponding $\eta_{PL}$ and $\eta_{EF}$ degradation. . . . .	69
5.8 Lifetimes of devices with luminance scaled to match the EML thickness. PL collapses due to matched exciton density. . . . .	69
5.9 Scaling behavior of $\eta_{PL}$ and $\eta_{EF}$ as a function of a) luminance and b) exciton density. . . . .	70
 B.1 Fluorescence (a) and Phosphorescence (b) spectra for several materials obtained from this system. . . . .	90
 C.1 Circuit used for measuring polaron density. Voltage readings are taken at 1-4 over a 1M $\Omega$ termination. . . . .	92
C.2 Differential currents for a hole only device. Currents on either side of the device are shown in a. while the difference between them is shown in b. . . . .	93
C.3 a. Hole only device architectures. b. Current Voltage characteristics for the devices shown in a. Steady-state sweeps as well as current measured from the differential technique are shown.	93
C.4 Polaron population as a function of current for the devices in Figure C.3a . . . . .	94

# List of Tables

3.1	Fit parameters extracted from transient and steady-state electroluminescence. Transient EL fit parameters averaged over all measured current densities. $\eta_{\text{EQE}}$ roll-off parameters averaged over several measured devices. Triplet-triplet annihilation and triplet-polaron quenching rates are fixed to those obtained from fitting the normalized efficiency roll-off. . . . .	40
5.1	Summary of device lifetimes. For each device, the starting luminance ( $L_0$ ), current density ( $J$ ), starting voltage ( $V_0$ ) and time at which 50% of the initial luminance is reached ( $t_{50}$ ) are reported. . . . .	73